LABORATORY FOR SOLID STATE PHYSICS

ETH Zurich
Department of Physics

Annual Report 2011

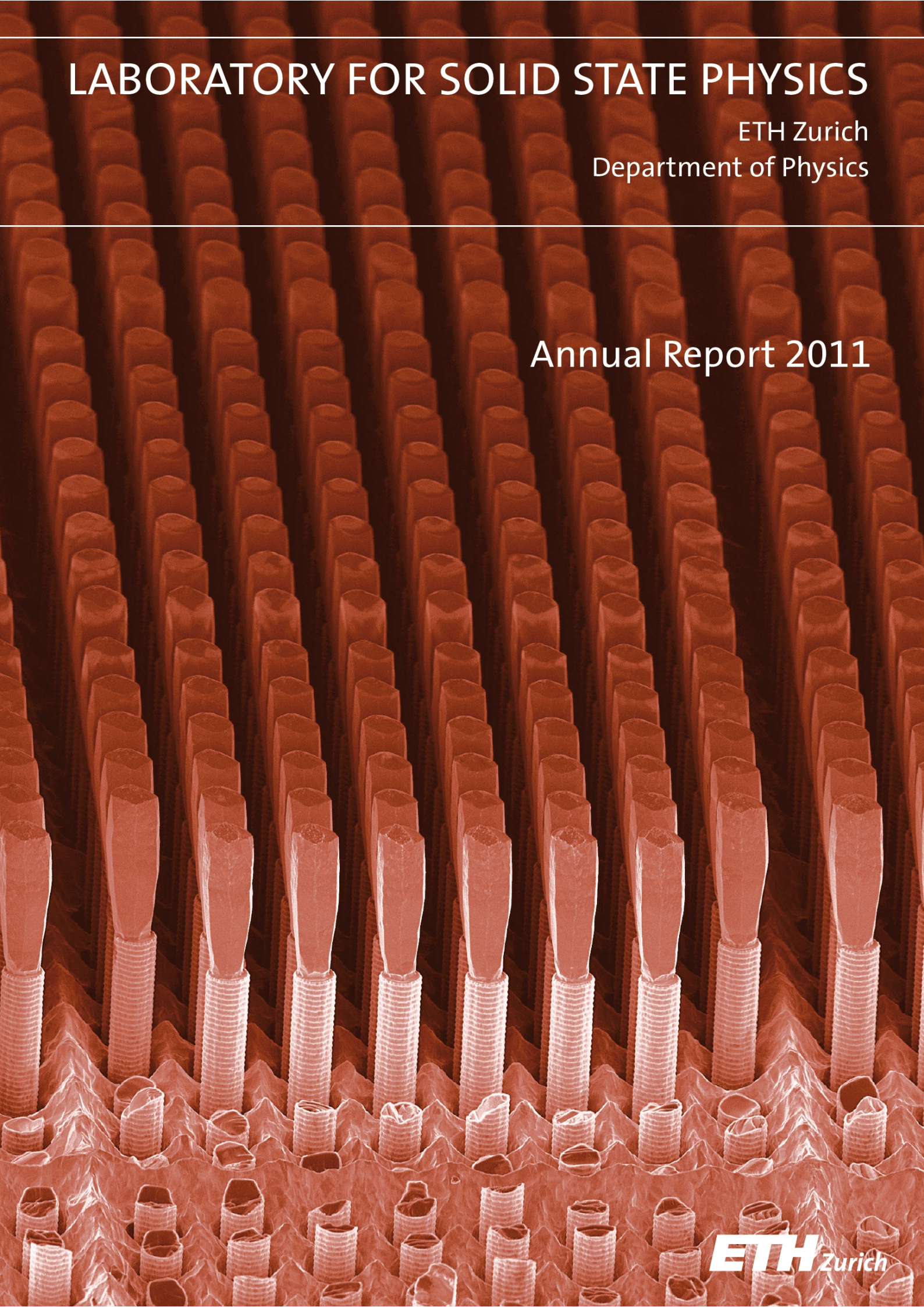

ETH Zurich

ANNUAL REPORT
2011

Solid State Physics Laboratory (LFKP)
ETH Zurich

Cover page:

Germanium pillars epitaxially grown on a Silicon wafer. The novel growth technique is designed to grow thick layers of Germanium on Silicon while relaxing the lattice mismatch strain. The achieved excellent Si/Ge interfaces are an essential ingredient for next generation X-Ray detectors.
From the Physics of New Materials Lab.

This annual report was edited by: Philip Moll

PREFACE

The Laboratory for Solid State Physics at ETH Zurich is pleased to present the Annual Report for 2011. This report summarizes our diverse research highlights, which have been published in high ranking journals and presented at international conferences. The members of the Laboratory are also committed to all aspects of teaching. Bachelor and Master level courses were offered for physics students as well as for students of other departments. The experimental research at the laboratory of solid state physics and our teaching activities benefit from the excellent infrastructure provided by ETH Zurich and in particular by the physics department. We thank the involved people for their dedication and solid support especially in all technical and administrative matters. Prof. René Monnier was a member of the laboratory for solid state physics for many decades and he retired in early 2012. Prof. Monnier was a highly regarded specialist in local density calculations and he applied this technique to a variety of material systems. His engagement for students in general and for teaching in particular is legendary and he will leave a big gap behind. Many young people sought René's advice and he coached them and advised them in a personal, friendly and supportive manner. We will miss Prof. Monnier and wish him all the best for his retirement. PD Dr. Hans Zogg has been for a long time member of our laboratory. He has officially retired in July 2011. He headed the Thin Films Physics Group at ETH Zurich. The department benefitted from his teaching commitments including a lecture on Thin Films: Production, Characterization and Applications. Among Dr. H. Zogg's recent achievements were PbSe and PbTe mid-infrared vertical external cavity surface emitting lasers on Si and BaF_2 substrates for which outstanding properties were demonstrated. We will miss Dr. Zogg as a member of the Laboratory for Solid State Physics and as a colleague.

We very gratefully acknowledge the continuous and substantial support by the Schulleitung of ETH Zurich, but also by the Swiss National Science Foundation, the Commission for Technology and Innovation (KTI), the European Research Council, industrial partners and all other sources. We also have the pleasure to thank Dr. Volcker Hildebrandt, a graduate from this Laboratory, for a generous donation.

For preparing this Annual Report, we would like to thank Mr. Ph. Moll for editing the report and Mrs. Heidi Hostettler as well as Mrs. Amanda Eisenhut for the graphical design.

Zürich, Mai 2012

Der Vorsteher

Prof. Dr. W. Wegscheider

Contents

Chapter 1

Physics of New Materials

(http://www.pnm.ethz.ch/)

Head
Prof. Dr. Bertram Batlogg

Academic Staff
Balthasar Blülle
Dr. Claudiu Falub
Dr. Alfonso Gonzalez
Jonathan Hanselmann
Roger Häusermann
Jakob Kanter
Thomas Kreiliger
Thomas Mathis
Philip Moll
Tobias Morf
Dr. Yasmine Sassa
PD Dr. Hans von Känel
Kristin Willa
Tino Zimmerling

Administrative Staff
Gabriela Strahm

Technical Staff
Kurt Mattenberger

Master Theses
Willa Kristin (FS2011)
Von Rohr Fabian (FS 2011)
Mena Mattia (FS 2011)
Gretener Christina (FS 2011)
Mensch Philipp (FS 2011)
Blülle Balthasar (FS 2011)
Wälde Moritz (FS 2011)
Talirz Leopold (FS 2011)
Kreiliger Thomas (FS 2011)
Maturo Margherita (FS 2011)
Tehlar Andres (FS 2011)
Sigrist Bernhard (HS 2011)
Kneer Luisa (HS 2011)

High Pressure Synthesis

Head
Dr. Janusz Karpinski

Academic Staff
Andrey Belousov
Dr. Zbigniew Bukowski
Dr. Sergiy Katrych
Dr. Nikolai Zhigadlo

Academic Guests
Dr. Roman Puzniak, Polish Academy of Sciences, Warsaw(Poland)
Dr. Krzysztof Rogacki, Polish Academy of Sciences, Wroclaw(Poland)

1.1 Three-dimensional electronic structure of MgB_2 by soft X-ray angle-resolved photoelectron spectroscopy

Y. Sassa, N. D. Zhigadlo and B. Batlogg in collaboration with M. Månsson (Laboratory of Neutron scattering & Magnetism, ETH Zürich), B. M. Wojek, O. Tjernberg (Material Physics, KTH, Sweden), M. Kobayashi, V. Strocov (Swiss Light Source, PSI, Villigen)

MgB_2 is a multi-band multi-gap superconductor due to a particularly selective electron-phonon coupling and a complicated Fermi surface. Much of the available information on the electronic states come from angle-resolved photoemission (ARPES) measurements, particularly from ARPES at low-photon energies, which may suffers from a series of limitations due to its surface sensitivity of the probe. As a result, the presence of possible surface bands as well as the lack of information regarding three-dimensionality (k_z-dispersion) of the electronic structure makes a comparison with theoretical calculations somewhat difficult. To determine the true bulk-electronic structure of MgB_2, we used soft x-ray ARPES. Photoemission experiment in the soft x-ray range brings a number of advantages such as free-electron final state, simplified matrix elements and increased of the photoelectron escape depth. The latter, along with the enhancement of bulk sensitivity, improves the resolution of the perpendicular momentum k_z and thus, permits reliable investigations of the three-dimensional electronic structure. Figure 1 and figure 2 display our very first experimental data of the bulk-electronic structure of MgB_2 acquired by soft x-ray ARPES. The data show no trace of surface bands and are distinct from previously published data. In addition, the electronic structure is found to display a clear three-dimensional character and has been thoroughly mapped for all k-momenta and as a function of polarization. The data quality allows for a direct and quantitative comparison of the electronic structure with calculations.

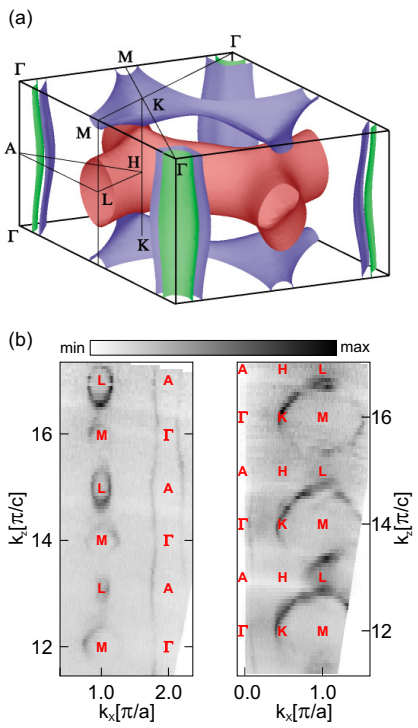

Figure 1.1: (a) Calculated Fermi surface of MgB_2. The blue and green cylinders centered around Γ (A) come from the bonding $p_{x,y}$ bands and the blue/red tubulars network are from the bonding/antibonding p_z bands (Kortus *et al.*, PRL 86, 4656 (2001)). (b) Fermi surface mapping in the k_x-k_z plane obtained by changing the photon energy. The mappings were done in the Γ-M (A-L) and Γ-K-M (A-H-L) direction. The measurement were performed at T = 10 K with linear vertical polarized light.

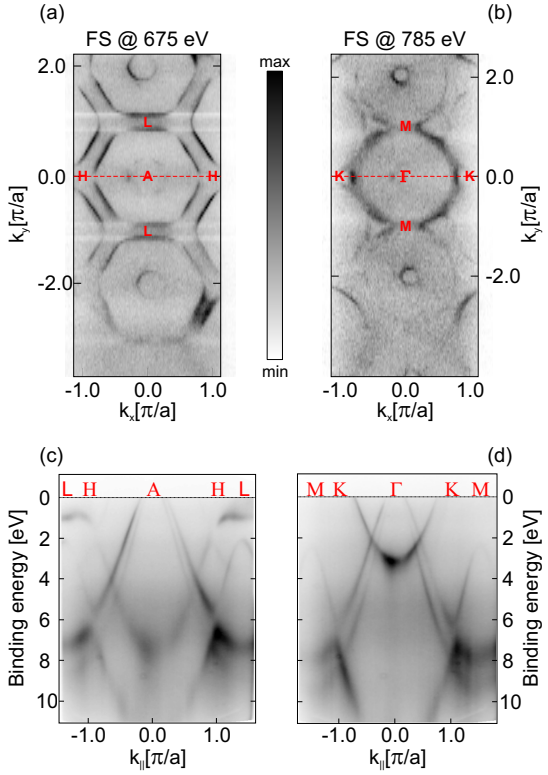

Figure 1.2: Fermi surfaces and band dispersions of MgB_2 measured by soft x-ray ARPES. (a-b) Spectral intensity maps obtained at two different photon energies (i.e, k_z) and integrated of ± 100 meV about E_F. The dashed red line mark specific cuts taking along H-A-H and K-Γ-K directions, respectively. (c-d) Band dispersions corresponding to the cut in (a) and (b). The measurement were performed at T = 10 K with circular polarized light.

1.2 Angle-resolved photoelectron spectroscopy study of $EuFe_{(2-x)}Co_xAs_2$

Y. Sassa, Z. Bukowski and B. Batlogg in collaboration with M. Månsson (Laboratory of Neutron scattering & Magnetism, ETH Zürich), Johan Chang (Laboratory for synchrotron and neutron spectroscopy, EPF Lausanne), Magnus H. Berntsen, O. Tjernberg (Material Physics, KTH, Sweden)

The discovery of superconductivity in the iron-based pnictides provided a new class of compounds to the high-temperature superconductor (HTS) family. $EuFe_2As_2$ is an interesting member of the '122' family since it is the only known compound containing 4f electrons. In addition, it exhibits a first antiferromagnetic (AFM) spin density wave (SDW) transition associated with the Fe moments at T_{SDW} = 190 K and a second one connected to the AFM ordering of the Eu^{2+} spins at T_{AFM} = 19 K. Previous angle-resolved photoelectron spectroscopy (ARPES) experiments performed on the parent compound reported that below the ordering temperature of the iron planes, back-folding bands reflected the orthorombic/antiferromagnetic Brillouin zone boundary hybridizes with non-folded bands resulting to a Fermi surface reconstruction and an energy gap. By substituing Fe to Co, superconductivity emerges with a T_c = 8K. To understand the connection between magnetism and superconductivity details on the electronic structure are important. By using ARPES, we have investigated the low-energy electronic excitations of the electron doped compound $EuFe_{(2-x)}Co_xAs_2$ (x = 0.20) as function of the k-momentum and below the Eu ordering transition. Figure 1(a) displays a constant energy map plotted at the Fermi level. Both hole-like pockets centered at Γ and an electron-like around the X point are easily visible. Contrary to the parent compound, no Fermi surface reconstruction were detected. Figure 1(b,e) displays typical ARPES spectra acquired at Γ and X points, respectively. Their location in k-space are indicated by the two solid blue lines marked 1 and 2 in (a). The dashed lines represent the dispersion extracted from Lorentzian fits of the momentum distribution curve (MDC) at different binding energies. Figure 1(c,f) represents their second derivative where a supplementary feature at the X point can be easily seen at a binding energy higher than 75 meV. The nature of this band (hole or electron) is unclear and required more investigation to clarify this issue. Figure 1(d,g) shows the momentum distribution curve (MDC) at different binding energies for Γ and X. Figure 1(h-k) displays the energy distribution curve (EDC) at k_F for Γ and X and their symmetrized EDC. The presence of a magnetic gap for α and β bands is clearly visible with $\Delta_\alpha = 14 \pm 2$ meV and $\Delta_\beta = 24 \pm 4$ meV. However, within the experimental resolution, no gap was detected for the γ band. The origin of this different gap magnitude is unclear and more investigations will be performed to clarify this issue.

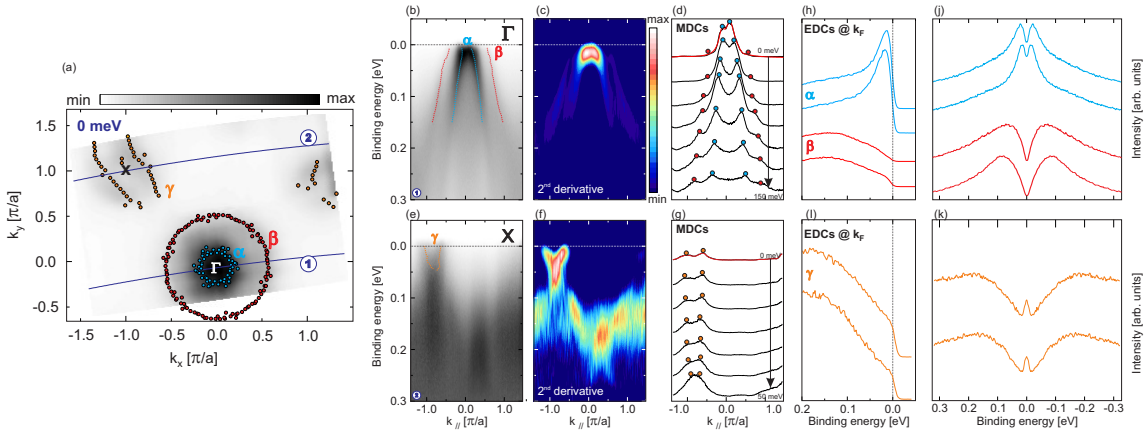

Figure 1.3: (a) Spectral intensity map obtained by energy integration of ARPES spectra $\pm$ 10 meV about E_F. The two solid blue lines mark the two specific cuts 1 & 2 in k-space displayed in (b,e). The filled circles represent k_F as determined from Lorenztian fits of the MDCs at E_F. (b,e) ARPES spectra acquired at Γ and X points, respectively. The dashed lines represent the dispersion extracted from Lorentzian fits of the momentum distribution curve (MDC) at different binding energies. (c,f) Second derivative of (b,e). (d,g) Momentum distribution curve (MDC) at different binding energies for Γ and X. The solid red curve is a Lorentzian fit of the MDC at the Fermi level (E_F) and the color circles represent the MDC peak position. (h,l) Energy distribution curve (EDC) at k_F for Γ and X. (j,k) Symmetrization of the EDCs showing the presence of a gap for α and β and no gap for the γ band.

1.3 Fast Josephson vortices in iron pnictide superconductors

P. Moll, L. Balicas, D. Geshkenbein, G. Blatter, J. Karpinski, N. Zhigadlo, B. Batlogg

With the discovery of new high temperature superconductors such as the iron pnictides, questions about their potential for technological applications arise naturally. Essential for any application is the materials capability to immobilize vortices ('pinning'), as moving vortices cause dissipation of energy. The observation of large critical currents j_c and disordered vortex lattices in the layered iron-pnictides indicates the existence of strong vortex pinning centers. To gain insight into the rich vortex physics on a microscopic scale and to further improve j_c, it is highly desirable to locate the pinning sites within the crystal structure. To this end we create a particular vortex arrangement by aligning the magnetic field along the superconducting planes in SmFeAs(O,F) (T_c 50-48K). In this situation, we discovered a distinct vortex matter transition upon cooling below T* 41K into a unique configuration of highly mobile vortices. Below T*, the vortex core is confined in-between two adjacent FeAs planes by periodic modulations of the superconducting order parameter within the unit cell, but are nearly free to slide between adjacent planes. This motion parallel to the planes is even more pronounced at lowest temperatures, well below T_c and H_c2, as the vortex cores avoid the highly effective pinning sites located in the FeAs layers. For fields slightly out-of-plane (¡0.3°) the vortices are again completely immobile as they cross the planes and are hence strongly pinned by defects within the FeAs layers. Our results indicate a strong and highy effective pinning mechanism localized in the FeAs layers, thus opening a pathway to improve the technological prospect of the pnictides.

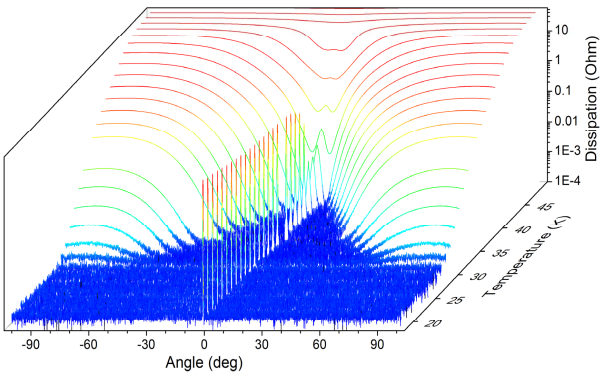

Figure 1.4: Dissipation as a function of angle between the magnetic field and the FeAs planes for several temperatures, acquired under a field H=12T. Starting at high temperatures, the typical V-shaped angular dependence originating from the anisotropy of the material turns into a broad peak centered exactly at the FeAs planes. Upon cooling, a sharp peak appears at a temperature $T^* \approx 42K$ and increases exponentially in height for 3-4K below T^*. The FWHM of the peaks is below 0.3° at low temperatures.

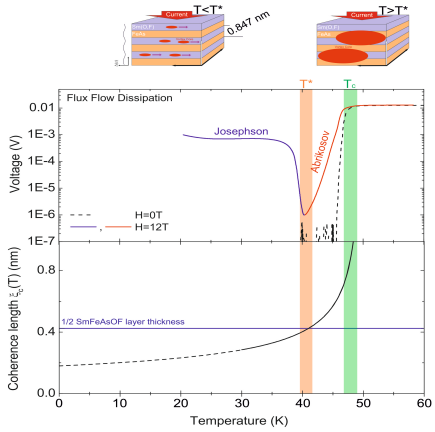

Figure 1.5: (upper panel) Flux flow dissipation in zero field and 12T, well aligned with the FeAs planes. Below T_c, a typical exponential decrease of dissipation due to pinned and thermally activated vortices is observed. At the temperature $T^* \approx 42K$, the of flux flow dissipation increases dramatically accompanied by a pronounced sharp peak shown in Fig.1.4. The temperature T^* is also the temperature at which the coherence length equals the thickness of the SmO layer (lower panel). This unusual and strong flux flow dissipation even at lowest temperatures despite the strong pinning observed at all other field angles supports the picture of highly mobile Josephson-like vortices within the SmO layers, avoiding the pinning centers in the FeAs sheets.

1.4 $CePt_2In_7$: Shubnikov-de Haas Measurements under High Pressures

J. Kanter, P. Moll, F. Ronning, E.D. Bauer, S. Friedemann, P. Alireza, B. Batlogg

Pressure is a very important experimental parameter in condensed matter physics as it can be a direct and gradual control of the electrons orbital overlap in a solid. Especially in correlated electron systems pressure is a valuable parameter in measurements probing electronic correlations.
Pressures above 25 kbar are usually only accessible by anvil pressure cells and electronic transport measurements remained a very difficult task as the implementation of several pressure resistant electrical leads on one anvil is non-trivial. To this end we have applied the Focused Ion Beam (FIB) technique to facilitate measurements of small, micro-structured samples under pressure using highly strain resistant contact leads, see Fig. 1 a & b.
In one application of this technique we are investigating the evolution of the effective electron masses, reflecting the electronic interactions, by measuring the quantum oscillations of the resistivity (Shubnikov-de Haas) as a function of applied pressure in the heavy fermion system $CePt_2In_7$. Upon increasing pressure the antiferromagnetically ordered phase is suppressed with the Néel temperature extrapolating to a quantum critical point (QPC) and an unconventional superconducting phase is induced. The magnetic fluctuations connected to the quantum critical point are thought to stabilize the superconducting phase, rendering the investigation of the evolution of the effective electron masses in $CePt_2In_7$ a very interesting candidate for Shubnikov-de Haas measurements under high pressures.

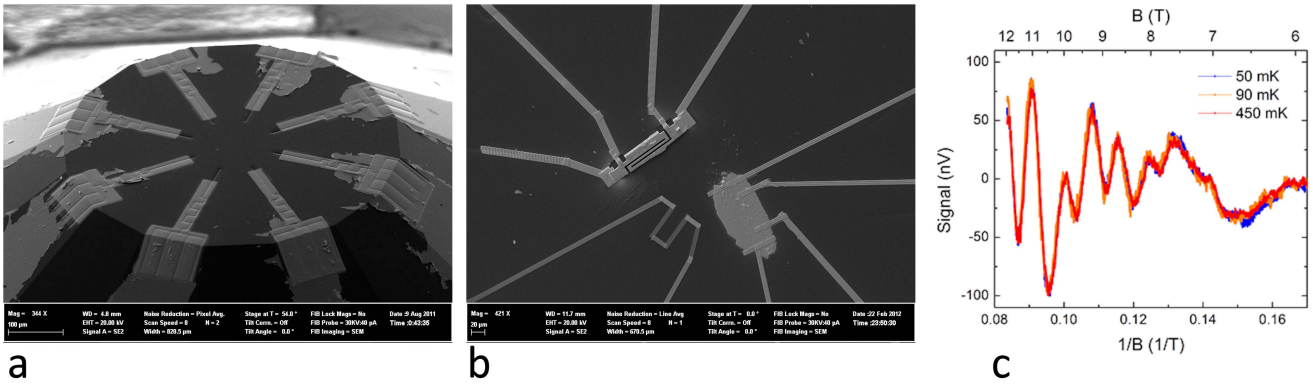

Figure 1.6: **a** Prepatterned diamond anvil providing 8 highly pressure resistant contact leads **b** FIB-structured and contacted samples with an increased length over cross section ratio, strongly improving the measurement signal. **c** Measurement data showing quantum oscillations in the resistivity in $CePt_2In_7$.

1.5 Composition, structure, magnetism, and superconductivity in $SmFeAs_{1-x}P_xO_y$

N.D. Zhigadlo, S. Katrych, P.J.W. Moll, J. Kanter, J. Karpinski, and B. Batlogg, in collaboration with M. Bendele, S. Weyeneth, R. Puzniak, H. Keller (Zurich University), R. Khasanov , V. Pomjakushin (PSI), M. Tortello, R.S. Gonnelli (Politecnico di Torino)

In the fully oxygenated compounds, the main impact of P substitution are to suppress the Neel temperature of the spin density wave (SDW) state and to strongly reduce the local magnetic field in the SDW state. The appearance of superconductivity in the $SmFeAs_{1-x}P_xO_y$ samples caused by oxygen deficiency was realized only after heat treatment under high pressure (HP). Oxygen deficiency brings the Sm-O charge-transfer layer closer to the superconducting As/P-Fe-As/P block and facilitates electron transfer. Single crystals of $SmFeAs_{1-x}P_xO_y$ with various T_c have been grown under HP, and their structural and superconducting properties were investigated.

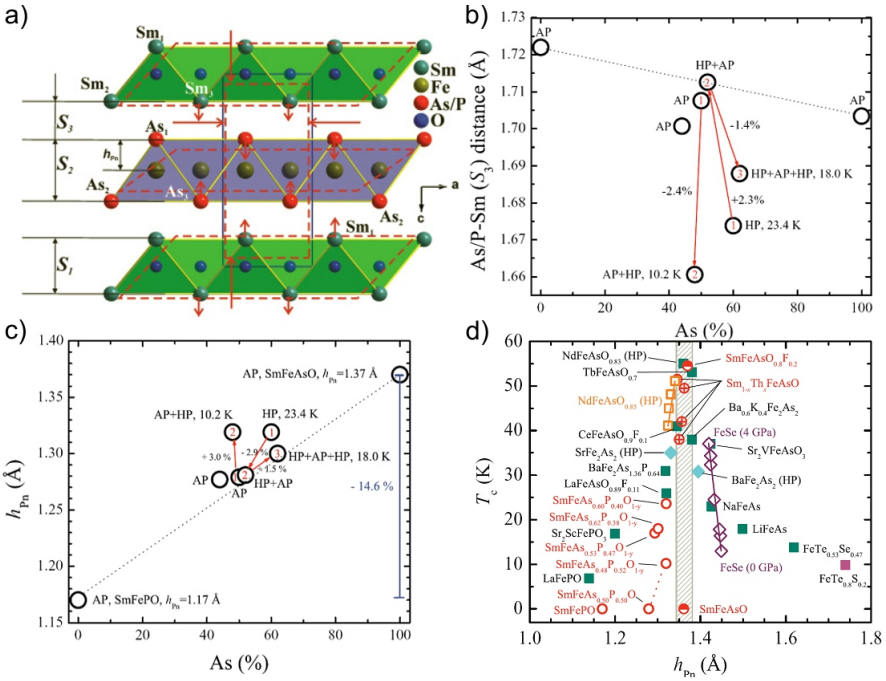

Figure 1.7: (a) Schematic representation of the projection of the $SmFeAs_{1-x}P_xO_y$ lattice on the *ac* plane and its changes with substitution of As by P (red dotted lines). (b) Interlayer distance S_3 and (c) pnictogen height h_{Pn} for $SmFeAs_{1-x}P_xO_y$ samples synthesized at ambient pressure (AP), high pressure (HP), and their combinations. Digits in the circles show the sequence of heat treatment. (d) Anion height dependence of the superconducting transition temperature T_c for various Fe-based superconductors. Our experimental results are indicated by red circles. The dashed line highlights the changes in h_{Pn} due to oxygen deficiency.

1.6 Magnetism and superconductivity in $LaFeAsO_{0.945}F_{0.055}$

N.D. Zhigadlo, S. Katrych, J. Karpinski, in collaboration with R. Khasanov, Z. Shermadini, M. Bendele, A. Amato, H. Luetkens (PSI); S. Sanna, G. Prando, P. Carretta, R. de Renzi (CNISM di Pavia)

Our results point to a strong difference between $LaFeAsO_{1-x}F_x$ and the structurally related families of Fe-based HTSs. In the most families bulk magnetism and bulk superconductivity are found to coexist on the nanoscale level. We show that the application of hydrostatic pressure on $LaFeAsO_{0.945}F_{0.055}$, which is at the border to the superconducting state but still magnetic, leads to a substantial decrease of T_N and a reduction of the magnetic phase volume and, at the same time, to a strong increase of T_c and the diamagnetic susceptibility. From magnetic-history-dependent ZF-μSR measurements it can be concluded that superconductivity most probably develops in the areas of the sample that are nonmagnetic down to the lowest temperatures. This shows that in $LaFeAsO_{1-x}F_x$ magnetism and superconductivity are competing order parameters.

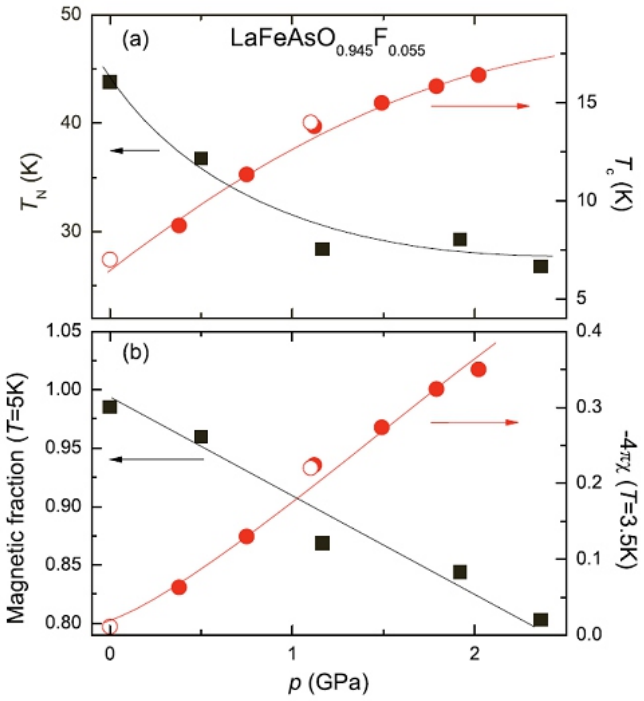

Figure 1.8: (a) Dependence of the magnetic ordering temperature T_N and the superconducting transition temperature T_c on pressure. (b) The magnetic fraction at T = 5 K and ZFC diamagnetic susceptibility -4$\pi\chi$ at T = 3.5 K, μ_0H = 5mT as a function of pressure.

1.7 Conducting interface versus conducting surface involving TTF and TCNQ crystals

T. Mathis, K. Mattenberger, B. Batlogg

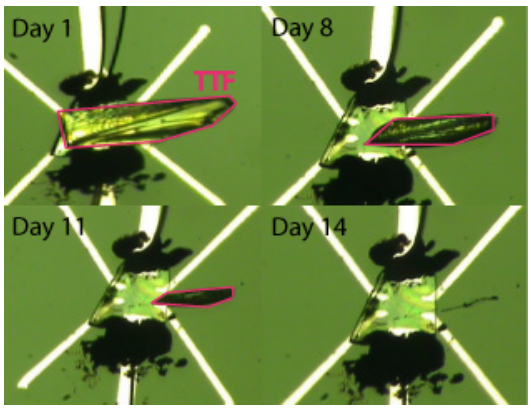

Figure 1.9: A TTF crystal (outlined in pink) placed on top a TCNQ crystal fully sublimates in two weeks. (1 bar He atmosphere, no UV light)

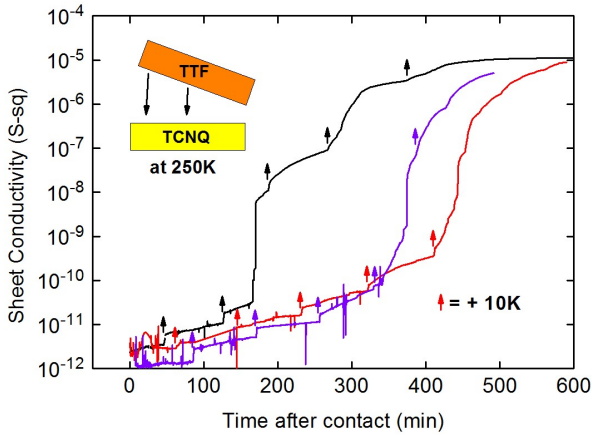

Figure 1.10: Three pairs of TTF and TCNQ crystals are laminated at 250 K. The surface conductivity is initially not affected but increases at an increased rate when the temperature is raised in 10 K steps (indicated by arrows) to room temperature. This dynamics suggests transfer of TTF molecules by sublimation.

When a TTF crystal is placed onto a TCNQ crystal at room temperature, a highly conducting layer is formed. In the last year we explored to what degree this is due to physical contact or transfer by sublimation of one species onto the other crystal. High purity crystals were grown by vapor transport, increasing their purity by resublimation. We have performed a variety of time-dependent surface conductivity measurements, including TTF lamination on TCNQ at

room temperature and low temperatures, as well as deposition of TTF molecules from the gas phase. The crystal-to-crystal contact contribution is found to be insignificant, while TTF sublimation onto TCNQ is dominant even at room temperature.

1.8 Deep trap states in Rubrene single crystals induced by ion radiation

T. Zimmerling, K. Mattenberger, M. Döbeli, M. J. Simon and B. Batlogg

The performance of organic electronic devices is limited by a high density of imperfections causing charge carrier trapping. Therefore, developing a deeper understanding of the various ways such traps are created is desirable. In this study, we induced defects in rubrene crystals ($C_{42}H_{28}$) by controlled irradiation with 1 MeV protons or He^+ at different fluence levels ($0.1 - 5 \cdot 10^{12}$ ions/cm^2), and quantified the resulting increase of the density of trap states (DOS).

Rubrene crystal were grown by physical vapor transport and sandwiched between two gold contacts as shown in Figure 1.11. To separate the irradiation effects from possible other influences only one part of the crystal was irradiated while the other was shielded to serve as reference. The trap DOS has been derived from bulk I-V measurements at different temperatures and by analyzing them in terms of temperature-dependent space-charge-limited currents (TD-SCLC).

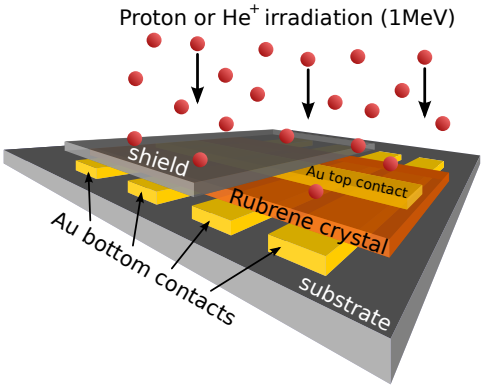

Figure 1.11: A Rubrene crystal sandwiched between gold contact to allows I-V measurements through the crystal bulk. One part of the crystal is irradiated with 1 MeV ions while the other is shielded.

Figure 1.12 (left) shows the creation of a trap peak in a crystal irradiated three times with protons. While the DOS of the shielded reference remains unaffected within experimental uncertainty, proton radiation of the unshielded part induces a pronounced trap peak that is ~ 0.2 eV wide and is centered at ~ 0.35 eV above the VB edge. The impact of proton and He^+ irradiations can be compared by calculating the radiation dose which is the absorbed energy per unit mass of the crystal. Unexpectedly, the trap density increases sublinearly and saturates at high dose, as depicted in Figure 1.12 (right).

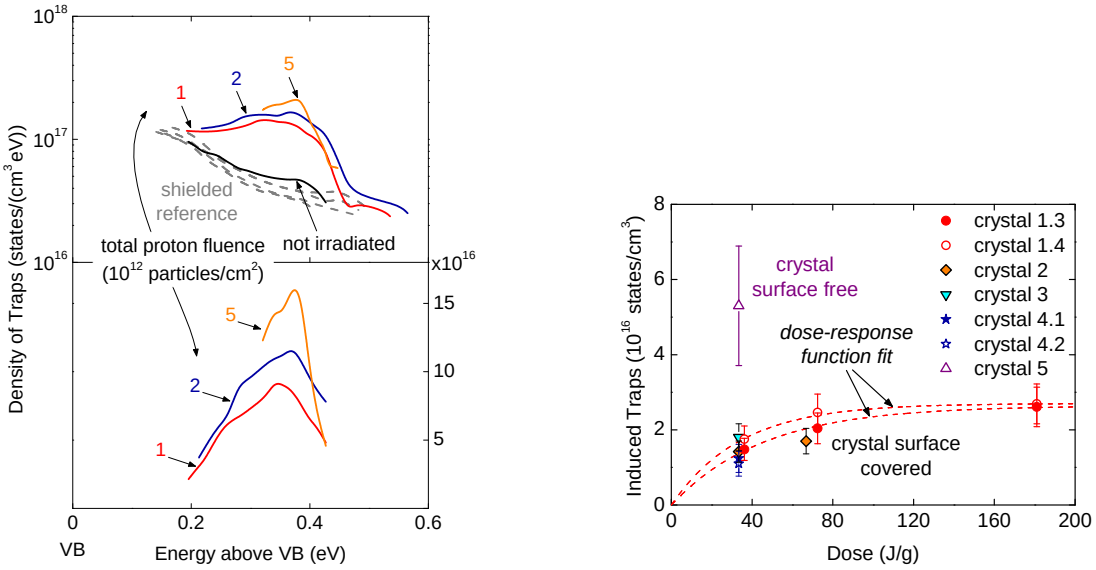

Figure 1.12: **Left:** Increase of the DOS after three doses of irradiation. **Right:** Induced trap density as function of radiation dose. A saturation of the induced trap density reflects the coexistence of trap creation and trap healing.

Saturation of the trap density at a low level of damage ($\sim$ 1 trap per 50 000 molecules) reflects the interplay between trap generation and trap healing. We attribute the generation process to breaking-off a H from the rubrene molecule

which is a known phenomenon in organic materials. Trap healing can take place if a H reattaches to a molecule where hydrogen has been previously removed. At high dose, both processes are in equilibrium. If the crystal surface is not covered by the top contact, hydrogen can desorb from the crystal which reduces the probability of trap healing. As a result the trap density is expected to be higher which was confirmed experimentally. Thus we have experimentally established the link between an electronic trap level and the underlying physical defect.

1.9 Charge trapping during gate-bias stress in Organic Field Effect Transistors

R. Häusermann, B. Batlogg

Charge trapping in organic field-effect transistors (OFETs) happens on various time scales. Trapping due to gate-bias stress is a relatively slow process which takes place on the timescale of fractions of seconds up to several days, posing a challenge to the experiment as well as the conceptual understanding. Additionally it is a major concern in the design of stable electric circuits incorporating OFETs.
The threshold voltage shift can be measured using two different methods: either a full transfer curve is measured before and after stress and the threshold voltage is extracted directly or a reduction of the Drain current is measured over time, which is then used to calculate the relative threshold voltage shift. The two methods give the same results as seen in figure 1.13.
Several mechanisms have been proposed to explain the threshold-voltage shift under gate bias stress: (i) trapping of charges in the bulk of the semiconductor, (ii) trapping in disordered areas of the semiconductor, (iii) trapping in regions in-between crystalline grains of the semiconductor, (iv) trapping in states at the semiconductor/dielectric interface and (v) formation of bipolarons in the semiconductor. It has been shown, that as long as SiO_2 is used as the dielectric, trapping of charges in the dielectric dominates the threshold Voltage shift.

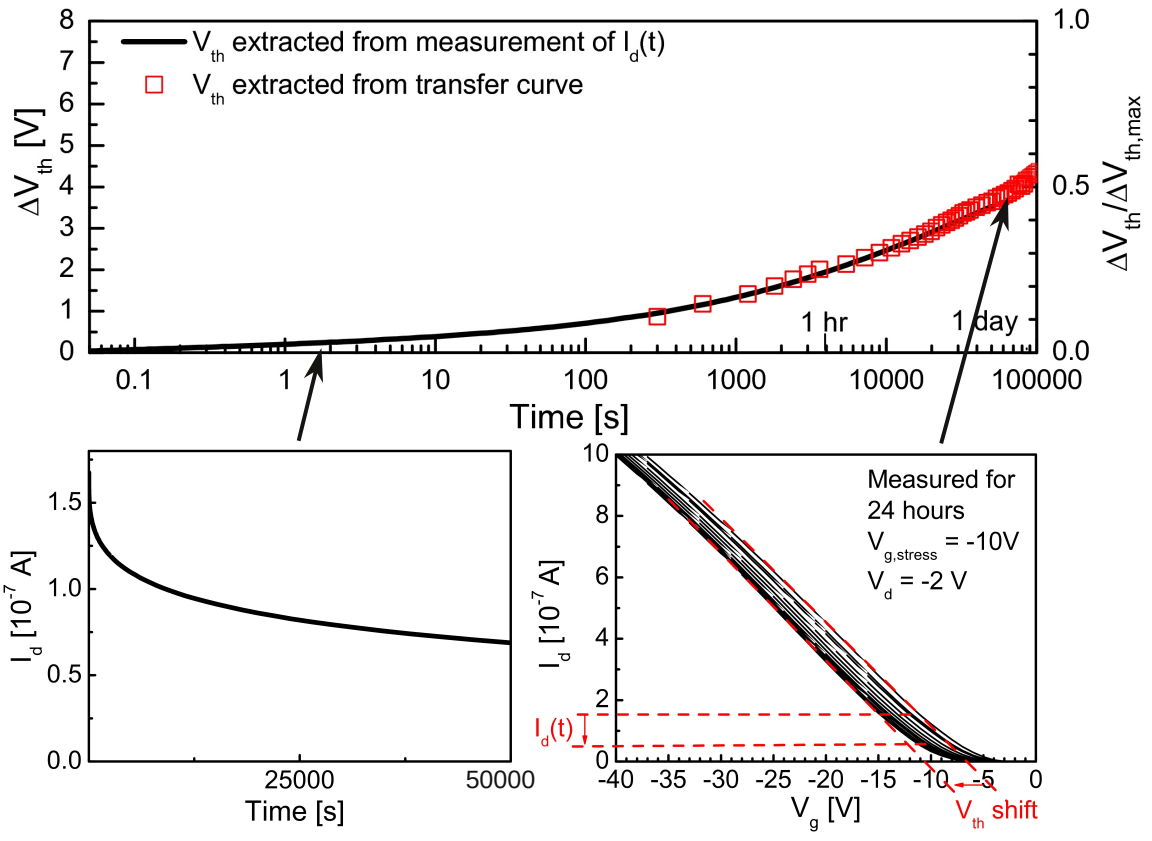

Figure 1.13: Extraction of the threshold voltage shift due to gate bias stress using two methods.

We study the role of the gate-insulator and semiconductor separately by fabricating devices with the same semiconductor but different insulators. Thin polycrystalline films or single-crystals of pentacene are used as the semiconductor. Untreated SiO_2 or a highly hydrophobic fluoropolymer (Cytop) form the gate-dielectric. Depending on the materials combination, we could show, charge trapping to occur either predominantly in the semiconductor or both in the semiconductor and the insulator. Remarkably, combinations of single-crystal/Cytop do not exhibit any charge trapping during gate-bias stress. Combinations of thin-film/Cytop however do show significant trapping. This suggests that charges are trapped in the semiconductor but not in the Cytop.
This work has been published: R. Häusermann and B. Batlogg, Applied Physics Letters **99**, 083303 (2011).

1.10 Organic Single-Crystal field effect Transistors from n-type Semiconductors

R. Häusermann, A. Flury, P. Schönherr, T. Mathis, B. Batlogg

In the last few years we have been able to characterize and understand organic p-type semiconductors by analyzing the density of states in the band-gap depnding on the preparation of the whole device. Therefore as a next step we will apply our measurement techniques to organic n-type semiconductors. To do these time consuming measurements and characterizations a good organic molecule needs to be chosen which is both easily processable and gives high performance. To chose the right compound 4 different commercially available organic molecules have been chosen. As a first step, organic single crystals from these compounds have been grown by physical vapor transport and their conductive properties have been analyzed.

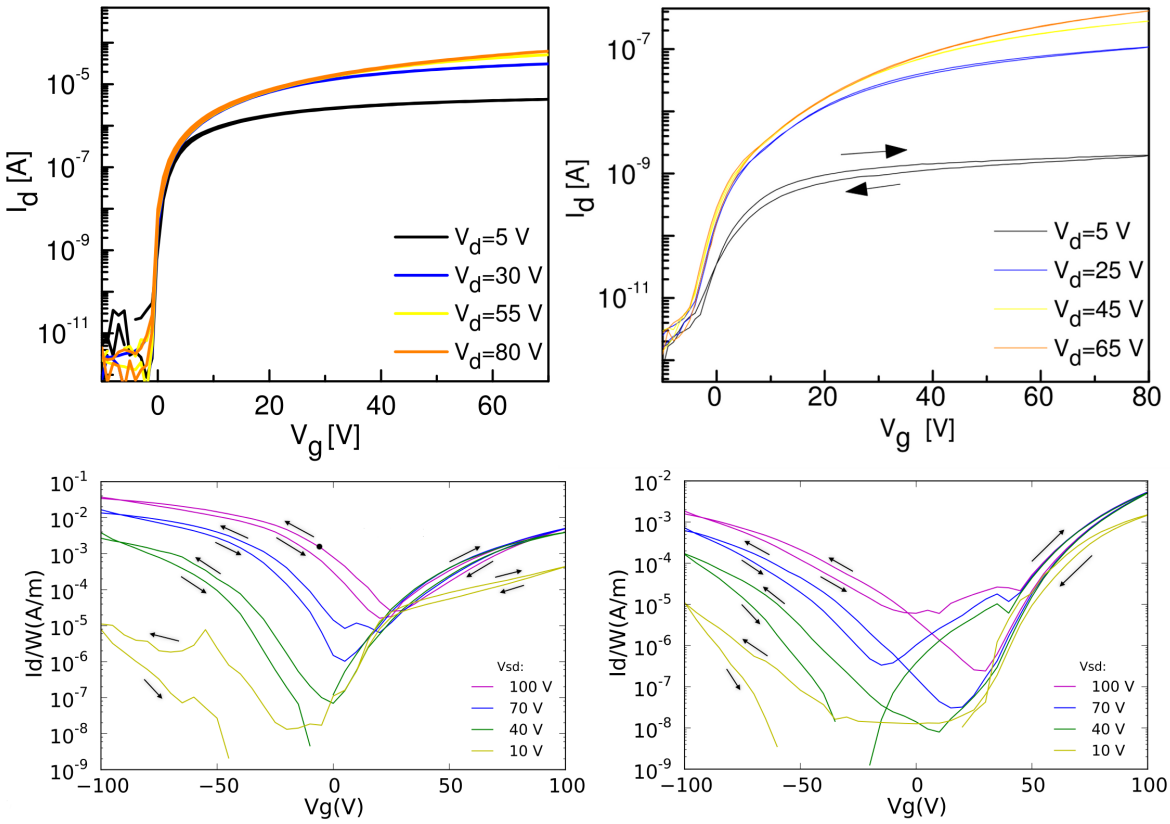

Figure 1.14: Organic single-crystal field effect transistor made from 4 different organic compounds.

It was possible to grow single crystals from all four materials, but only one material showed the desired performance (top left in figure 1.14). The other 3 materials where usable transistors, but with a high charge injection barrier.

Therefore for the other materials the contacts need to be tailored to reduce the charge injection barrier. Interestingly, after changing the contact to a gold/Magnesium double layer, ambipolar charge transport has been observed in two of the 4 compounds (lower to graphs in figure 1.14)

1.11 A solution processed high performance n-type Organic Semiconductor

K. Willa, B. Batlogg

As charge transport in organic semiconductors takes place due to the overlap of the π-bonds of adjacent molecules, the crystalline order in the semiconducting layer is of great importance. There are still many open question concerning the current transport mechanism in organic semiconductors. Different transport processes seem to dominate depending on the crystalinity, that is to say on the processing conditions.
We have spincoated the high performance n-type organic material reported under 1.10 (”Organic single-crystal field effect transistors from n-type semiconductors” by R. Häusermann) to compare transistor performance under different processing conditions. A chlorobenzene solution of this material was spincoated onto UVO and HMDS treated Si-SiO_2 samples, resulting in mobilities as high as 0.22 Vs/cm^2. Temperature dependent measurements were carried out, showing that the threshold voltage decreases with temperature, but suprisingly the mobility stays constant.

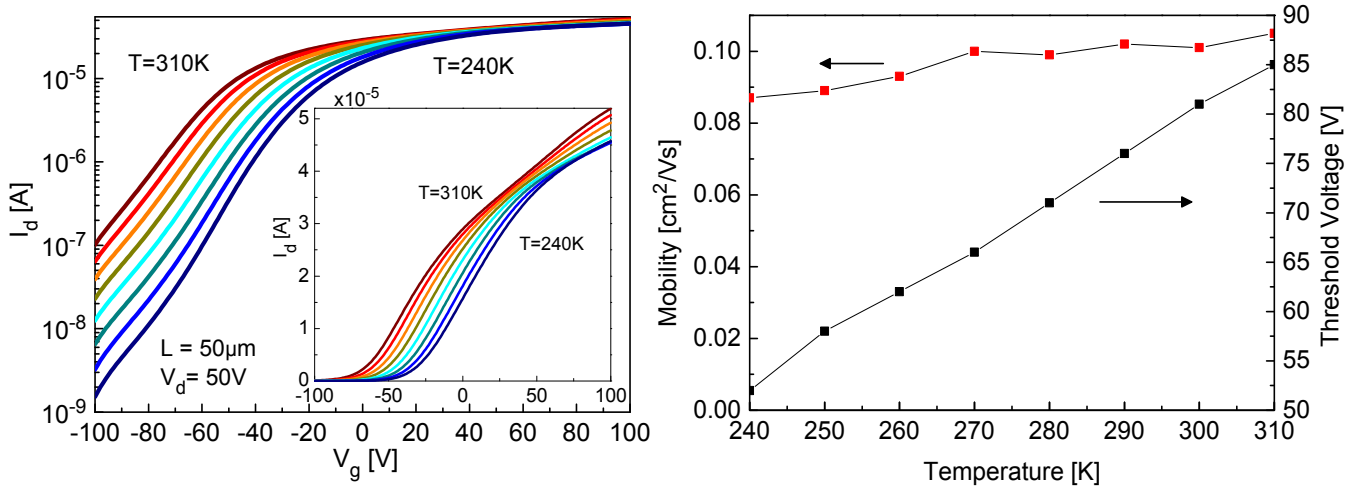

Figure 1.15: On the left the temperature dependent transfer curves of the high performance n-type material are plotted on a logarithmic scale and on a linear scale in the inset. On the right the extracted threshold voltage and mobility can be seen.

1.12 Arrays of Three-Dimensional Semiconductor Crystals

C.V. Falub, A.G. Taboada, T. Kreiliger, E. Müller, H. von Känel

In collaboration with: F. Isa, D. Chrastina, G. Isella (L-NESS, Politecnico di Milano, Italy), R. Bergamaschini, A. Marzegalli, L. Miglio (Dip. di Scienza dei Materiali, Università di Milano-Bicocca, Italy), P. Niedermann, A. Neels, A. Pezous, R. Kaufmann, A. Dommann (Centre Suisse d'Electronique et Microtechnique, Switzerland)

Despite significant progress in epitaxial growth techniques achieved in the last few decades, monolithic integration remains a challenge when it comes to combining materials differing in lattice parameter and thermal properties. The main problems are defect generation as a result of the lattice mismatch, as well as wafer bowing and crack formation, resulting from different thermal expansion coefficients. The latter become especially serious whenever an application requires an epitaxial layer to be thicker than just a few microns, as is the case for example for X-ray or particle detectors, high efficiency triple junction solar cells, and power electronic devices.

A leap closer to the solution of all these problems was recently made in the framework of the NEXRAY project funded by the Swiss Nano-Tera program one of the aims of which is the development of an X-ray imaging detector monolithically integrated on a silicon CMOS chip [1]. Applying a novel concept [2] to the problem of growing exceptionally thick Ge and SiGe layers yielded surprising results.

The basic idea behind our new approach is very simple. After patterning a Si substrate in the form of pillars with high aspect ratios (height to base), Ge or SiGe layers are deposited by low-energy plasma enhanced chemical vapor deposition (LEPECVD). After an initial phase of both lateral and vertical expansion, the epitaxial crystals forming on top of the Si pillars were found to switch to purely vertical growth, remaining separated by a small air gap up to heights exceeding 50 μm. Numerous growth experiments along with theoretical modeling allow us to understand the mechanism governing this very unusual mode of growth. It is basically a consequence of epitaxial growth very far from equilibrium, induced by high growth rates ($\approx$7 nm/s) and low substrate temperatures ($\approx$500 °C), as a result of which surface diffusion is very much reduced. Additionally, geometric flux shielding by nearest-neighbor crystals greatly diminishes growth on facets inclined with respect to the interface plane. Consequently, instead of forming continuous films full of cracks and crystal defects, we obtain space-filling arrays of three-dimensional crystals. The analysis of these structures by high-resolution XRD, SEM, TEM and defect etching revealed that the crystals are strain and defect-free despite the large lattice and thermal mismatch with the Si substrate. Although definite proof of the novel concept has been achieved only for group IV semiconductors, we believe it to be applicable to most materials combinations used for the fabrication of semiconductor devices.

[1] C.V. Falub, H. von Känel et al., Science, 335, 1330 (2012).

[2] H. von Känel and L. Miglio, International patent application WO 2011/135432.

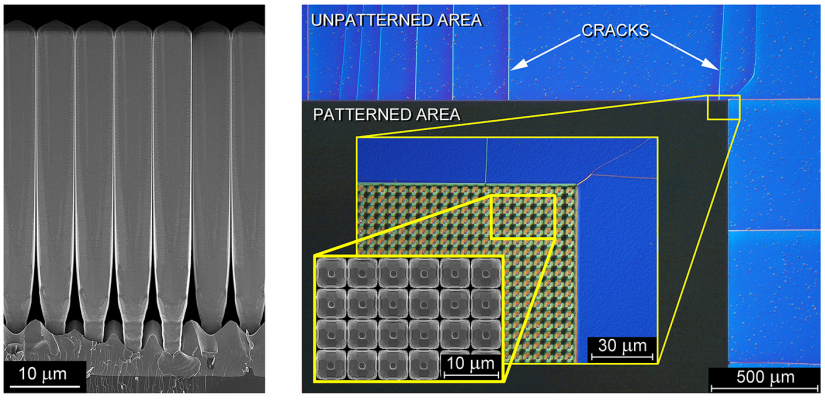

Figure 1.16: Left: SEM micrograph of 50 μm tall Ge crystals grown epitaxially on patterned Si substrates at 490 °C. Right: Nomarski interference contrast micrographs of $\approx$27 μm tall Ge towers grown at 490 °C on Si pillars. Crack propagation stops at the border between patterned and unpatterned areas.

1.13 Impedance Spectroscopy Simulation of Organic Semiconductor Devices

B. Blülle, R. Häusermann, T. Morf, T. Zimmerling, T. Mathis, B. Batlogg

In recent years, organic semiconductor devices of different structure and from different source materials have been fabricated and studied in our group. The physics of charge transport and the effect of traps in the density of states (DOS) has been investigated by means of current-voltage (IV) measurements. The steady-state characteristics of diode-like 'sandwich-devices' (SCLC devices) and of organic field-effect transistors (FET) under DC operation is well understood and the output- and transfer-curve of FETs can be simulated by means of a quasi one-dimensional numerical model considering band- and hopping-transport.

We are currently expanding our investigations to time-dependent phenomena and studying the current response of different devices under AC operation. In the steady-state case, the current-voltage characteristics are governed by multiple effects on different time-scales (charge transport, diffusion, injection, hopping transport, ...). We expect these phenomena to be more distinguishable in frequency dependent impedance spectroscopy measurements and simulations.

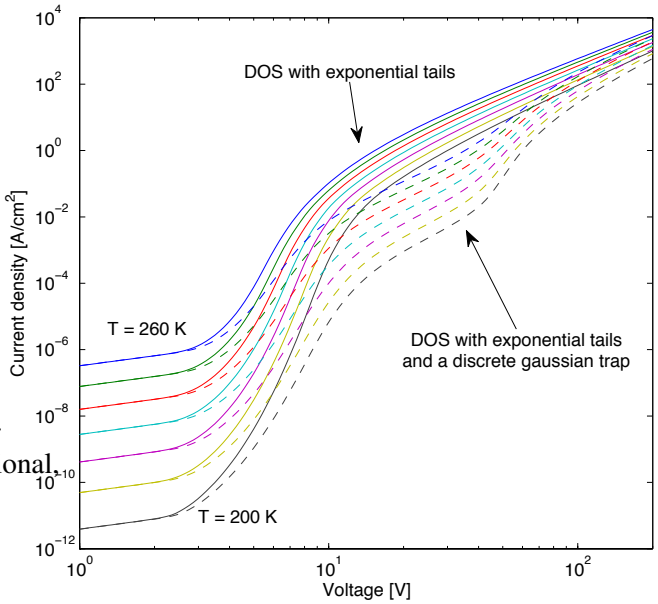

Figure 1.17: SCLC current-voltage simulation for different temperatures (200K - 260K, steps of 10K) and for two different DOS distributions with constant bands, exponential trap tails (solid lines) and an additional discrete gaussian trap (dashed lines).

On the modeling side, we implemented a simulator based on the drift-diffusion model (DD-model), which was adapted to account for a given trap distribution in the DOS. Sandwich-structured SCLC devices, which are intrinsically one-dimensional, can be simulated by a 1D-implementation of the DD-model. This is favorable in consideration of the computational effort required to solve the non-linear differential equations describing the model. The FET devices are modeled in 2D, where both, top-gate-bottom-contact and bottom-gate-bottom-contact setups are considered. Frequency dependent AC currents are simulated using sinusoidal steady-state analysis (SSSA), where we assume the device to be operated under an applied DC bias (steady-state), perturbed by a small oscillating voltage at the drain contact. The solution of the linearized DD-equations about the DC operating point in combination with a frequency dependent statistical trapping model then leads to a complex system response from which we can calculate the magnitude of the impedance and its phase shift with respect to the applied oscillation.

We found that the simulated DOS-dependent DC current-voltage characteristics is in good agreement with measurements of both, SCLC-devices and FETs. The AC response simulations show a well pronounced dependence on the number of trap states and their specific capture- and release rate and a well pronounced transit time effect allows the extraction of the charge carrier mobility.

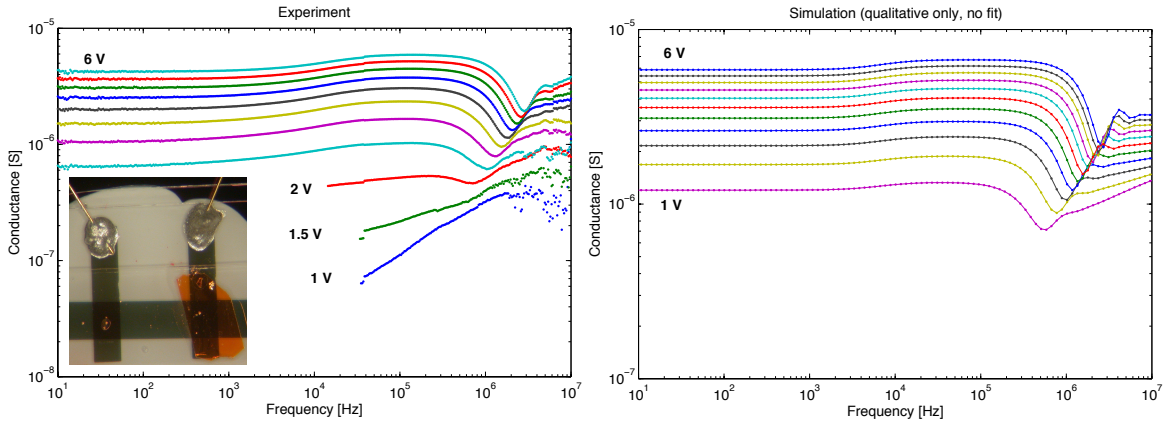

Figure 1.18: Impedance spectroscopy: experiment and simulation. The conductance $G = \Re(Z^{-1})$ obtained from simulated impedance Z at different bias voltages is in good qualitative agreement with results obtained by measurement of a rubrene SCLC-device (see inset). The transit time effect is revealed by the decrease of conductance at $f \approx 10^6$ Hz.

1.14 Contact Resistance between organic semiconductors and metal contacts

T. Morf, C. Mattfeld, B. Batlogg

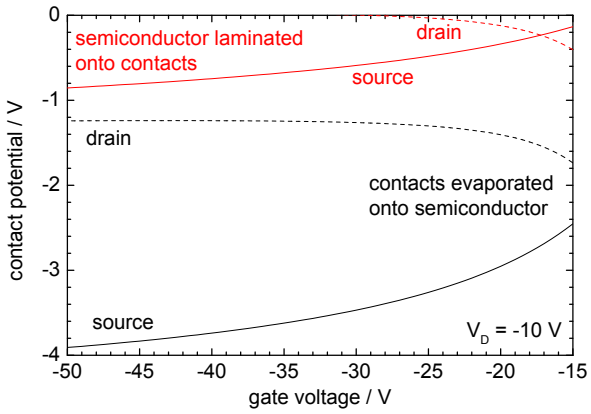

Figure 1.19: Measured contact potential for hole injection and extraction betwee gold and Rubrene. Irrespective of the contacting method, the potential drop is significantly larger for charge injection than for extraction. The difference between the two contacts is at least paritally due to the additional segment of current flowing from the evaporated contacts through the crystal to the bottom channel.

Unlike inorganic semiconductors, contacts to the organic materials cannot be tuned by doping of the active material. This requires a better understanding of parameters governing the charge transfer between metals and organic materials.

We access the contact resistance via potential drop in four-point measurements of single-crystal field-effect transistors. For gate voltages much larger than the drain voltage, the potential in the channel varies linearly with position. This allows the independent extraction of both injection and extraction resistance.

Using this method we compare the potential drops of contacts fabricated by different methods. The most used techniques are evaporation of the metal onto the semiconductor and lamination of an organic crystal to predefined contacts. However, for the prior case one has to consider an additional effect due to the device layout. Since the contacts are evaporated on top of the crystal while the gate is below it, charge carriers have to pass through the crystal before reaching the channel. In order to determine the respective contributions from this segment and from thermal load during evaporation, new methods of laminated top-contacts are presently explored.

Chapter 2

Physics of Semiconductor Nanostructures

(http://www.nanophys.ethz.ch)

Head
Prof. Dr. K. Ensslin
Prof. Dr. T. Ihn
Prof. Dr. R. Monnier

Academic Staff

S. Baer	S. Hellmüller	F. Nichele
C. Barraud	M. Hüfner	N. Pascher
J. Basset	A. Jacobsen	Dr. C. Rössler
D. Bischoff	Y. Komijani	Dr. P. Roulleau
T. Choi	A. Kozikov	S. Schnez
S. Dröscher	B. Küng	P. Simonet
T. Frey	Dr. P. Leek	M. Studer
U. Gasser	F. Molitor	A. Varlet
J. Güttinger	T. Müller	

Technical Staff

C. Barengo	P. Märki	P. Studerus

Academic Guests
K. Chida, Kyoto University (16.5.-17.6.2011)

Administrative Staff

C. Egli	C. Vinzens

NCCR QSIT

Dr. I. Blatter	S. Künzel	J. Rössler

2.1 Coherent electron-phonon coupling in tailored quantum systems

P. Roulleau, S. Baer, T. Choi, F. Molitor, J. Güttinger, T. Müller, S. Dröscher, K. Ensslin and T. Ihn

Coherent spin manipulation has already been accomplished in AlGaAs/GaAs double quantum dots (DQDs) and more recently also in InAs nanowires. Although the coherence times are usually limited by random nuclear fields, also electron-phonon coupling can be a source of decoherence. InAs nanowires and graphene are two alternative and promising materials for achieving coherent spin manipulation. In InAs nanowire DQDs, spin-orbit interactions are very strong and enable a more efficient electron-spin resonance driven by electric fields than with AlGaAs/GaAs DQDs. In graphene, it is expected that hyperfine coupling as a source of decoherence is very weak compared with AlGaAs/GaAs. Although electron-phonon interaction effects have been observed in carbon nanotube, AlGaAs/GaAs, or silicon quantum dots (QDs) and in AlGaAs/GaAs DQDs, only little is known about electron-phonon interaction in graphene and InAs nanowires.

Here, we report on an effect associated with coherent electron-phonon coupling in two entirely different DQD systems and therefore different electronic and phononic environments. The very strong confinement of electronic states in these two materials, in contrast to AlGaAs/GaAs DQDs, has enabled us to observe this coherent coupling, the solid-state analogue of the Dicke subradiance phenomenon. Almost 60 years ago, Dicke predicted superradiant and subradiant spontaneous emission, which was observed 40 years later with two trapped ions. Brandes et al. later proposed an interference effect due to electron-phonon interactions in a solid-state two-level system (DQD). Our experimental observations are interpreted in this framework. Periodic oscillations in the current through both double dot systems occur as a function of the energy difference of the levels in the two dots. The energy dependence of these oscillations allows us to infer a coherent coupling between electrons and the phonon field.

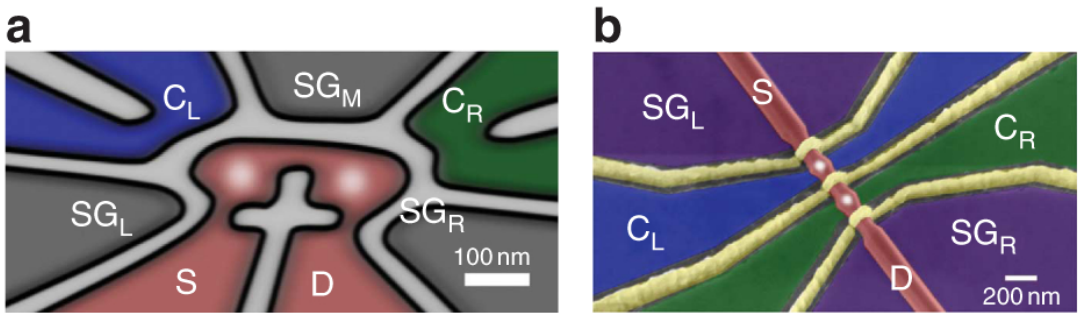

Figure 2.1: (a) Schematic representation of the graphene DQD. The two dots are separated by a 30 nm wide constriction and connected to source and drain (in red) by 20 nm wide constrictions. Both constrictions, in blue and green, serve as side gates to control the electrochemical potential of the QDs as well as charge detectors for the QDs. Additional side gates are shaded in grey. (b) Tilted scanning electron microscopy image of the NW DQD. The InAs NW (in red) is deposited on an AlGaAs/GaAs heterostructure with a two-dimensional electron gas 37 nm below the surface. Again, the constrictions in blue and green serve as side gates and as charge detectors. The purple side gates offer additional tunability. Metallic top gates (in yellow) enable us to independently tune the tunnel barriers.

2.2 Time-resolved charge detection in graphene quantum dots

J. Güttinger, J. Seif, C. Stampfer, A. Capelli, K. Ensslin, and T. Ihn

The high sensitivity of a quantum point contact or a single-electron transistor to its electrostatic environment is widely used as a powerful tool to detect the electron occupation in semiconductor-based quantum dot structures. Time-resolved charge detection offers the possibility of measuring extremely small currents by counting single-electron transitions and enables, e.g., the extraction of detailed electron tunneling statistics and probing of electron-electron correlations. Time resolution further allows for single-shot readout of spin qubits after spin-to-charge conversion with potential applications in future quantum information processors.

With the rise of two-dimensional graphene a fascinating new mesoscopic material for transport experiments has become available with the promise of long spin coherence times. First nanostructures have been made by etching graphene into narrow constrictions (nanoribbons). In these devices transport around the charge neutrality point is suppressed. Short constrictions have been successfully used as barriers for graphene quantum dots. Several experiments have been performed on graphene quantum dots including the observation of excited states in single and double quantum dots and the investigation of orbital and spin states around the electron-hole crossover. An additional nanoribbon placed in close proximity to the dot can be used to detect the number of electrons on the dot . In contrast to charge detection with a quantum point contact (QPC) tuned below the lowest conductance plateau, highly charge sensitive resonances in the detector nanoribbon are used as a sensor, similar to charge detection with a single electron transistor. These resonances arise from localization of charge carriers due to strong potential fluctuations in the disordered nanoribbon. Here we investigate tunneling through a graphene quantum dot lead in a time-resolved way by counting individual charging events with such an integrated graphene charge detector. The time resolution allows for a deepened analysis of the tunneling properties of a graphene constriction compared to the time-averaged case.

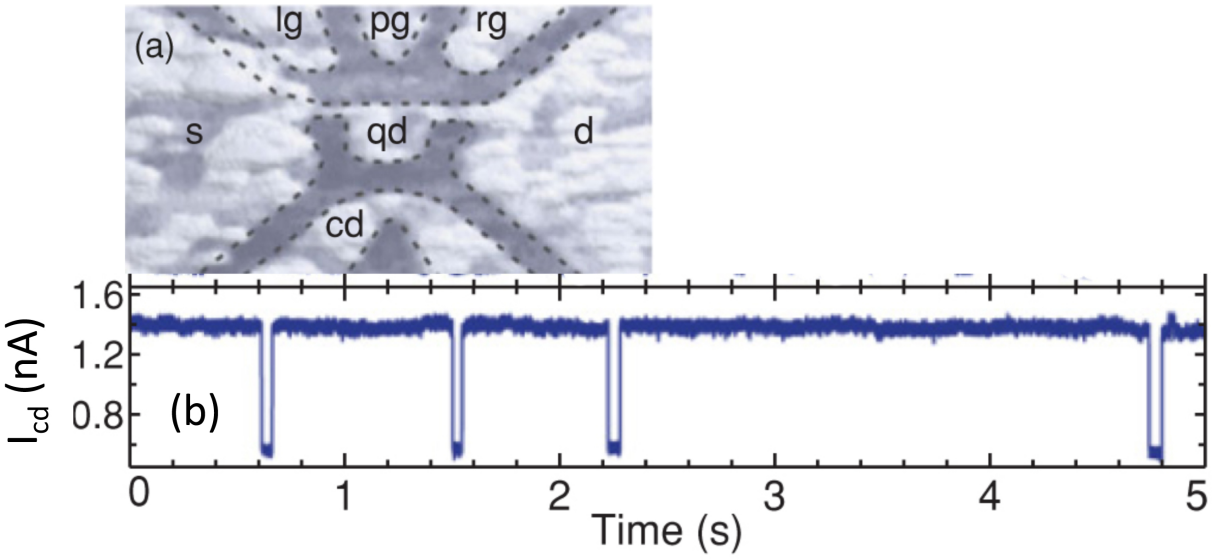

Figure 2.2: (a) SFM micrograph of the graphene quantum dot with source (s), drain (d), and lateral gates (pg, lg, rg), as well as the charge detector (cd) and its gate (cdg). (b) Time-resolved current through the charge detector. Each step up (down) indicates an electron leaving (entering) the quantum dot.

2.3 The relevance of electrostatics for scanning-gate microscopy

S. Schnez, J. Güttinger, C. Stampfer, K. Ensslin and T. Ihn

Scanning-gate microscopy (SGM) is a local probing technique that can unveil microscopic processes governing the conductance of nanostructures. The conducting tip of an atomic-force microscope is used to induce a potential perturbance in the nanostructure, thus altering the conductance of a particular sample as a function of tip position. Conductance maps are then obtained by recording the conductance while scanning the tip over the nanostructure. With this technique, various material systems and different types of nanostructures have been explored in the past, e.g. carbon nanotube-based quantum dots (QDs), GaAs- based quantum-point contacts, quantum wires, InGaAs-based quantum rings, GaAs-based QDs, superconducting single-electron transistors and recently graphene QDs. Scanning a tip over nanostructures causes an unwanted effect: the electrostatic potential experienced by charge carriers in the nanostructure changes during a scan because the moving metallic tip partially screens the electric field emanating from gate electrodes. In other words, the mere presence of the tip alters the transport properties of a nanostructure, even if contact potential differences between tip and gates are compensated. Although this is an obvious effect, its

importance has not been discussed in detail in the literature to our knowledge.

With the advent of graphene, two aspects may increase the importance of these screening effects. Firstly, graphene samples are typically not covered with a dielectric and secondly, voltages up to several tens of volts are applied to lateral gates. In this work, we have presented SGM on a graphene QD sample. We demonstrate that the screening effects can lead to apparent shifts of the QD resonances that are bigger than the lithographic extent of the sample. Moreover, under certain experimental conditions more than one set of Coulomb rings appears, which we also attribute to the strong screening effect. Our analysis corroborates with the constant-interaction model where we introduce the screening terms phenomenologically. We want to point out that our results are also of importance for other scanning-probe techniques, such as scanning-tunneling microscopy, although our findings are analyzed in the context of SGM.

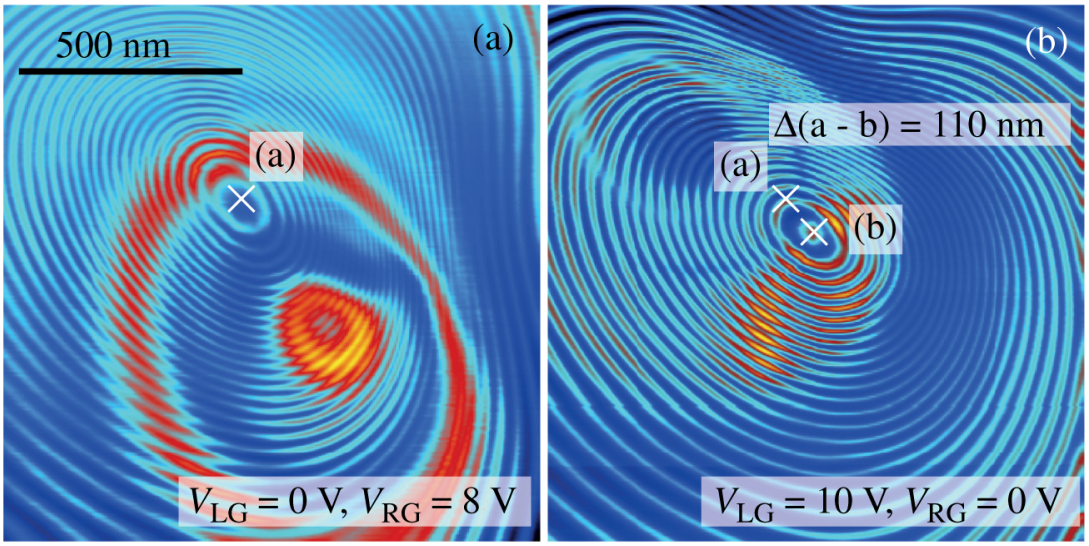

Figure 2.3: (a, b) Scanning-gate images taken in the hole regime for $V_{BG} = 12V$, $V_{tip} = 2V$ and $V_{bias} = 300\mu V$. The left- and right-side gates were changed as denoted in the figures. This results in an apparent shift of the centers of the Coulomb rings. These are denoted by (white) crosses; in (b) the center of (a) is also denoted. The overall shift is $\Delta = 110nm$.

2.4 Spatial mapping and manipulation of two tunnel-coupled quantum dots

M. Huefner, B. Küng, S. Schnez, K. Ensslin, T. Ihn, M. Reinwald, and W. Wegscheider

Most quantities measured in pure transport experiments, such as the current through a nanostructure, remain macroscopic and contain little spatial information. To justify assumptions about the potentially spatially nonuniform current flow in nanostructures it is highly useful to employ a probing technique which offers spatial resolution. Scanning gate microscopy, where a metallic tip is used to capacitively couple to the nanostructure acting as a freely movable gate, is a powerful local probing technique. It has been applied to a broad range of materials from two-dimensional electron gas (2DEG)-based semiconductors over InAs nanowires and graphene to superconductors. While it has been applied to investigate accidentally formed multiple dots no investigations of controllable, intentionally formed double dots have been reported to date. Here we show that we can control single electrons on a double quantum dot at 300 mK by moving a metallic tip across the structure. Spatial current maps allow us to gain insight into the topographic position of the charge distribution of the two quantum dots themselves. Our experiments give spatially resolved access to the microscopic electronic properties of a double quantum dot. They allow us to locally manipulate the electron number of the individual dots. This measurement technique lets us derive the positions of both quantum dots in real space and evaluate the relative shift of their positions due to in-plane gate voltages. We show that we can also deliberately form a single dot at different positions inside the defined structure by applying appropriate gate voltages. The position of a single dot is not altered above measurement resolution when a second dot is created next to it.

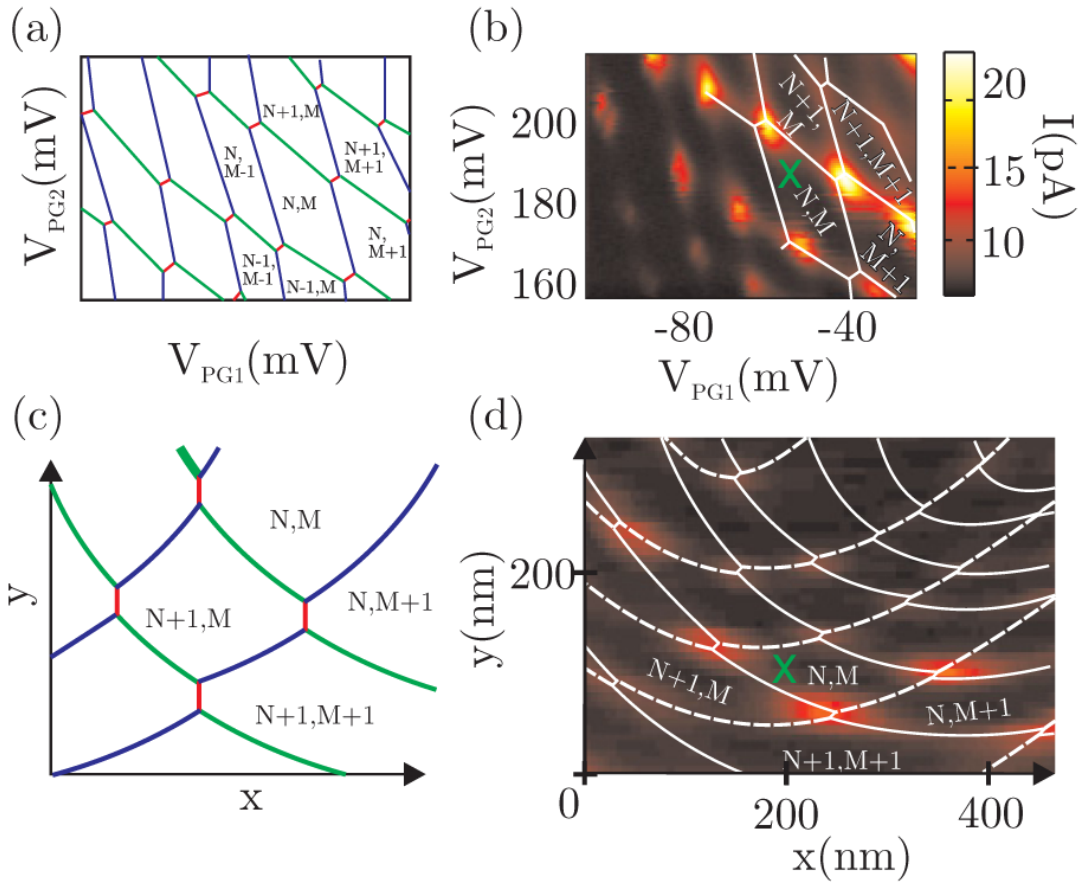

Figure 2.4: (a) Schematic of the hexagon pattern formed when measuring I(V_{PG1}, V_{PG2}) in the double dot regime. The letters i and j represent the number of electrons in dot 1 and dot 2 respectively. (b) shows the charge stability diagram for a source-drain voltage of 210μV. Panel (c) schematically shows the expected scanning gate pattern. The hexagons displayed in (a) are distorted in real space. (d) Current map of the double dot. The tip is scanned at a tip-sample distance d = 10 nm above the surface. Pairs of triple points are visible as regions of enhanced current. White lines are used as visual aids to highlight the underlying deformed hexagonal pattern. Labels (i,j) mark the same electron numbers on the dot as in the charge stability diagram shown in (b). The green cross marks the gate settings used for the current map shown in (d). The green cross in (d) marks the position at which the tip was located to record the measurements shown in (b). The green cross in (b) marks the voltage settings used to record the current map in (d).

2.5 Coulomb gap in graphene nanoribbons

S. Dröscher, H. Knowles, Y. Meir, K. Ensslin, and T. Ihn

Monolayer graphene shows impressive material stability, even if shaped into nanostructures of ≈10 nm in size. Its electronic properties are tunable by gate electrodes such as conventional semiconductors, while its conductivity competes with that of metals. Graphene nanoribbons have the potential to be used in nanoelectronics, and graphene nanoconstrictions are the basic building blocks for quantum devices. The transport properties of graphene ribbons and constrictions on a SiO_2 substrate have been one of the puzzles in the understanding of graphene nanostructures. Theoretical predictions of an energy gap in ribbons have triggered intense experimental and theoretical research. It has become evident experimentally that localized states due to edge and bulk disorder suppress the conduction and lead to a transport gap rather than a true band gap. In addition, experiments indicate the formation of an interaction driven Coulomb gap. A wealth of theoretical ideas ranging from Anderson localization to Coulomb blockade try to explain the phenomenology. We have shown that electronic transport in narrow nanoribbons is dominated by a chain of one or multiple quantum dots forming due to disorder. Not only is the conductance activated between conductance resonances, but the activation energy at each density corresponds to the Coulomb gap. At the lowest temperatures, cotunneling is present. Our experiments indicate that transport through graphene nanoribbons can be understood based

on the mesoscopic details of the sample in a single-particle picture including Coulomb blockade. In contrast to recent suggestions, there is no indication that additional energy scales or mechanisms are necessary to describe the observed behavior.

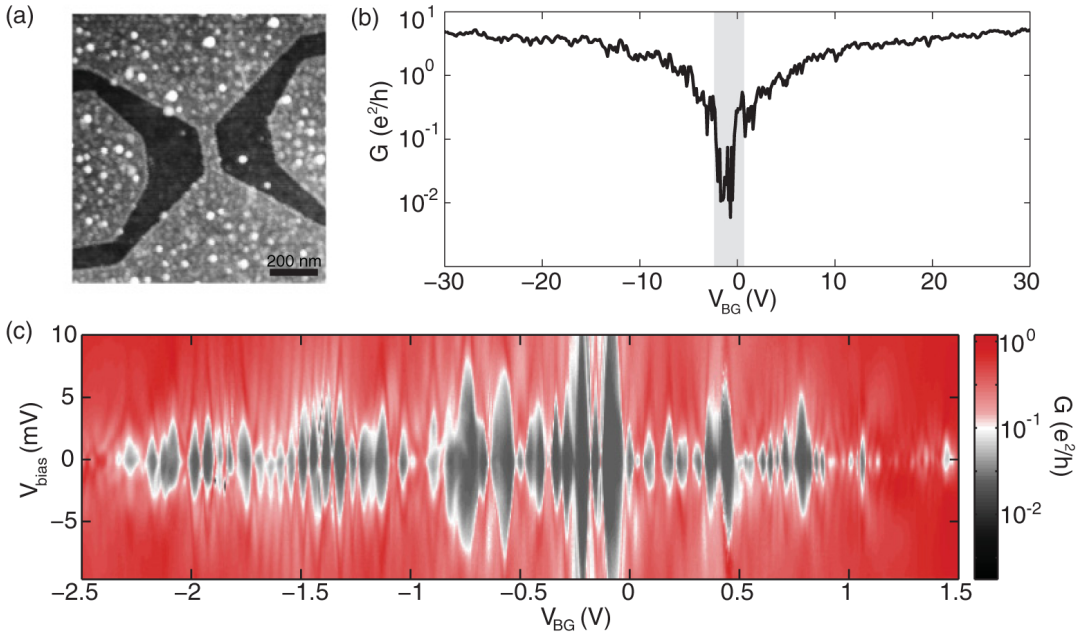

Figure 2.5: (a) Scanning force micrograph of the nanoribbon investigated here (L = 200 nm, W = 75 nm). (b) G(V_{BG}) in a large density range showing the transport gap around V_{BG} = 2 V. The measurement was taken at T = 1.25 K with a source-drain bias of $V_{bias} = 500\mu V$. (c) Finite-bias measurement inside the transport gap [same temperature as (b)].

2.6 Transport Properties of Clean Quantum Point Contacts

C. Rössler, S. Baer, E. de Wiljes, P.-L. Ardelt, T. Ihn, K. Ensslin, C. Reichl, and W. Wegscheider

Quantum devices on semiconductor nanostructures rely on quantum point contacts (QPCs) as the basic building blocks. Quantized conductance was observed early on and has been used as a signature of the quality of a quantum point contact QPC. With ever improving sample quality and the methodology for the detection of non-Abelian anyons in the ν = 5/2 fractional quantum Hall state, several experiments have recently used the properties of QPCs fabricated on ultra-high-mobility two-dimensional electron gases (2DEGs). In view of proposals to investigate fractional quantum Hall states in confined geometries and interferometer-like setups, a detailed understanding and the control of QPCs are essential. Here we present experimental data that go beyond previously published data by demonstrating experiments that profit from the extraordinary cleanliness of the high-mobility 2DEG. In contrast to standard 2DEGs, we do not observe defect-induced resonances when the QPCs are shifted laterally. Higher-order half-plateaus are observed in the finite-bias differential conductance at zero perpendicular magnetic field, as well as spin-split half-plateaus at finite perpendicular magnetic field. Finally, the 0.7 anomaly is investigated as a function of temperature and in perpendicular magnetic field.

Measurements at finite source-drain bias give access to the subband spacings of the QPC and reveal that QPC1 is described best by a short constriction, whereas QPC2 shows quantum wire-like characteristics. In addition to QPCs defined in standard 2DEGs, resonances at large bias are observed in QPC1 that correspond to higher-order transport conditions. These higher-order resonance conditions give valuable information about the shape of the confinement potential and enable the reconstruction of the full saddle-point potential in the constriction. Knowing the shape (and hence the slope) might prove important for the investigation of many-body states such as the 0.7 anomaly or the

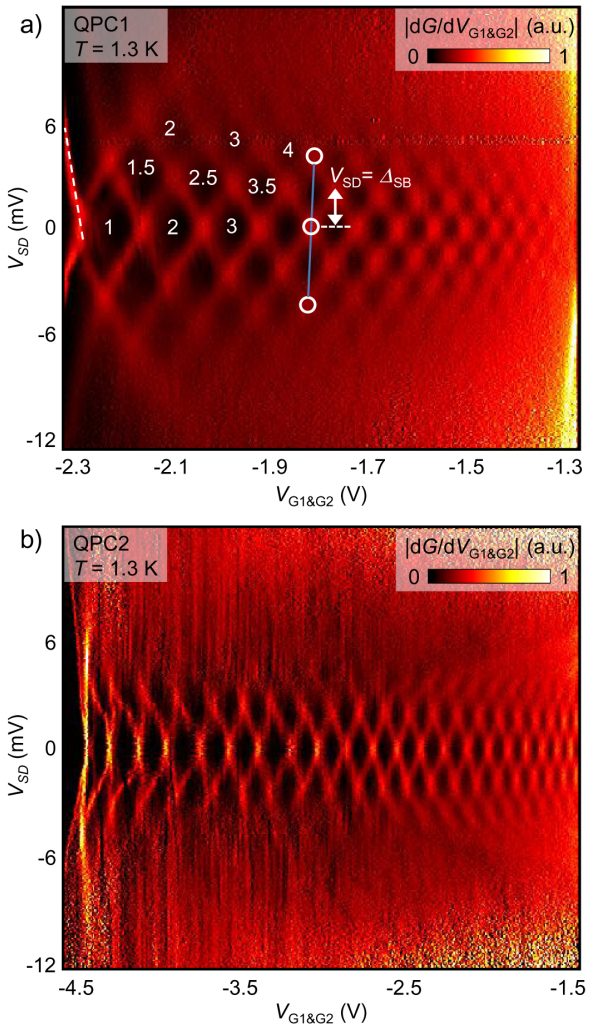

Figure 2.6: (a) Transconductance $G_{TC} = dG/dV_G$ of QPC1, plotted as a function of source-drain bias V_{SD} and voltage V_G applied to gates G1 and G2. Plateaus in the differential conductance of G =1,2,3,...2 e^2/h appear as black diamonds centered around V_{SD} = 0 mV. Their extent in V_{SD} corresponds to the subband spacing. Higher-order half-plateaus (G = 1.5, 2.5, 3.5, . . . 2 e^2/h) and second-order integer-plateaus (G =2,3,4,...2 e^2/h) appear as black diamonds at finite source-drain bias. (b) Transconductance of QPC2. Integer plateaus around V_{SD} = 0 mV are resolved. For gate voltages $V_G \leq 2.5V$, higher-order plateaus are obscured by noise.

transmission of fractional quantum Hall states. At finite magnetic field and lower temperature, a strongly exchange-enhanced g-factor is observed, which we interpret as the result of a very smooth confinement potential. While measurements on QPCs are possible with a high signal-to-noise ratio if the gate voltages are always swept in the same regime and direction, it was not possible to form a stable quantum dot with the same technique on the same wafer. For future interferometer experiments on high-mobility samples in the fractional quantum Hall regime, it is desirable to prepare split-gate electrodes on high-mobility wafers that do not rely on screening electrons at the X-valley and thereby allow stable gate operation.

2.7 Characterization of a microwave frequency resonator via a nearby quantum dot

T. Frey, P. J. Leek, M. Beck, K. Ensslin, A. Wallraff, and T. Ihn

The interaction of light and matter is one of the most fundamental processes in physics. One way to explore this area is to use artificial atoms such as quantum dots which offer, e.g., the possibility to tune the energy spacing of the individual electronic states. Using this possibility, the resonant absorption of photons by electrons in a quantum dot has been investigated in transport measurements of photon assisted tunneling. Cavity quantum electrodynamics (QED), the study of the coupling of matter to light confined in a cavity, is traditionally studied with atoms but also with solid state systems such as self-assembled quantum dots. Furthermore, the realization of circuit QED, in which a single microwave photon is trapped in an on-chip cavity and coherently coupled to a quantum two-level system, has led to significant progress in control and coupling of microwave photons and superconducting qubits. The study of the interaction between the electromagnetic field of such a resonator and a semiconductor quantum dot marks an important step toward realizing a hybrid quantum information processor, in which the advantages of different systems, such as a long relaxation time of the individual qubit8 and interaction between distant qubits, could be exploited in one device.

The sample, shown in Fig. 2.7(a), consists of a laterally defined quantum dot positioned at an antinode of the electric field of a microwave transmission-line resonator. The dot is realized on an AlGaAs heterostructure with a two-dimensional electron gas (2DEG) residing at the heterointerface about 35 nm below the surface. The device is fabricated by three stages of optical lithography followed by local anodic oxidation (LAO) with an atomic force microscope (AFM) to define the quantum dot. In the first of the three lithography steps, the mesa for the quantum dot (dark gray parts, labeled M in Fig. 2.7 (a)) is wet etched. Ohmic contacts (labeled C in Fig. 2.7(a)) are then used to contact the 2DEG. Finally, the microwave resonator and its ground plane (labeled R and GND in Fig. 2.7(a)) are defined in a lift off process by depositing a bilayer of 3 nm Ti and 200 nm Al. The minimum distance from the mesa edge to the resonator center conductor is around 2 μm. The coplanar waveguide resonator is designed to have a fundamental frequency of 7 GHz and is coupled to the input/output lines by two planar finger capacitors (Fig. 2.7(b)). The capacitance, determined in a finite element calculation, corresponds to an external quality factor of $Q_{ext} \approx 8000$. In Fig. 2.7(d), the AFM structure is shown which consists of the quantum dot connected by two tunnel barriers to the source (S) and drain (D) contacts used to measure the conductance of the dot. In addition, a left side gate (LSG), a plunger gate (PG), and a right side gate (RSG) are used to tune the potential of the quantum dot. The lithographic diameter of the quantum dot is approximately 230 nm.

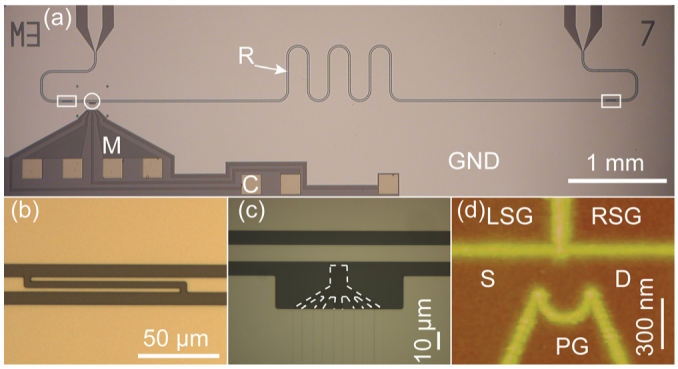

Figure 2.7: ((a) Optical micrograph of a microwave resonator (R) with an integrated quantum dot, (GND): ground plane of the resonator, (C): ohmic contact, (M): 2DEG mesa. (b) Magnified view of a coupling capacitor, location on the chip marked with rectangles in (a). (c) Enlarged view of the 2DEG mesa, location on the chip marked with a circle in (a). Edge of the mesa highlighted with a dashed line. (d) AFM picture of the measured quantum dot, realized on the 2DEG mesa. Source and drain contacts are labeled S and D, the plunger gate PG, and the left and right side gate LSG and RSG.

Chapter 3

Dynamics of strongly correlated materials

(http://www.solid.phys.ethz.ch/ott)

Head

Prof. Dr. Joël Mesot
Prof. Dr. Hans-Rudolf Ott

Academic Staff

Dr. Toni Shiroka
Dr. Krunoslav Prša
Francesco Casola
Marek Pikulski

Administrative Staff

Gabriela Strahm
Claudia Vinzens

3.1 NMR studies of disordered spin ladders in high magnetic fields

F. Casola, T. Shiroka, J. Mesot, and H.-R. Ott

in collaboration with M. Grbić, M. Horvatić, S. Krämer, S. Mukhopadhyay, C. Berthier (LNCMI, Grenoble),

S. Wang and H. M. Rønnow (EPFL, Lausanne), Ch. Rüegg (PSI, Villigen)

Quantum-dominated magnetism has recently been proposed as a paradigmatic research area for the study of the low-energy physics of both clean and dirty-boson systems in condensed matter [1, 2]. In real materials, containing spin arrays in one or two dimensions, disorder is usually introduced via chemical substitution, providing either a random variation in the exchange coupling constant via bond-disorder [3], or site-disorder by means of replacing magnetic with non-magnetic ions [4]. Bond randomness and site disorder are both known to cause boson confinement of the triplet excitations. However, the rich phase diagrams predicted in either case are still largely unexplored, reflecting the scarcity of materials where the external parameters can be easily tuned to access new regimes.

An excellent model compound for studying the physics of disordered antiferromagnets is the recently synthesized spin-$^1/_2$ zigzag ladder $Bi(Cu_{1-x}Zn_x)_2PO_6$ [5]. Here frustrated Cu ladders run along the b axis of the crystal lattice, with the P atoms residing at the centers of oxygen tetrahedra.

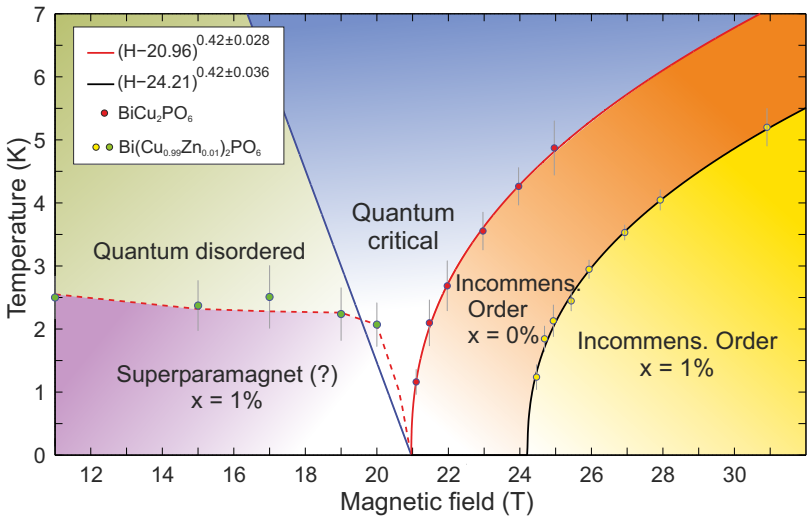

Figure 3.1: H-T phase diagram for both pure and 1% Zn-doped $Bi(Cu_{1-x}Zn_x)_2PO_6$. Doping at the 1% level introduces a 3 T shift of the phase boundary to $H_c \sim 24$ T.

NMR is the only method capable of probing the low-energy spin dynamics and the local magnetism in such systems at high fields (above 17 T). Our previous but preliminary ^{31}P NMR study on the compound with $x = 0$ at the high-magnetic-field laboratory LNCMI in Grenoble had revealed the onset of a field-induced ordered (FIO) phase at $H_c \simeq 20.9$ T for $H \parallel b$. Replacing Cu with Zn at the few percent level leads to IIO which, however, may be quenched by external magnetic fields $H_0(T)$. Recent neutron scattering data indicate that the IIO phase for $x = 0.01$ and $x = 0.05$ is suppressed at $H_0 \approx 4$ and 14 T, respectively [6]. Consequently, the IIO and the expected FIO phases are separated by a region with unexplored magnetic features.

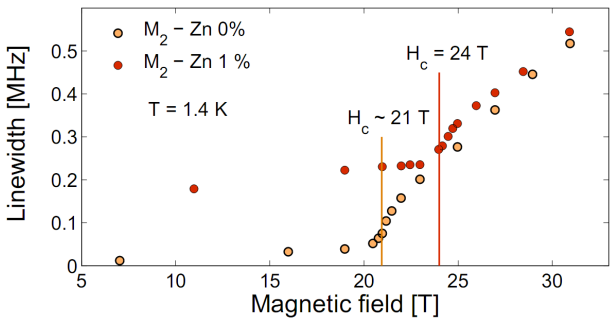

Figure 3.2: Order parameter (linewidth) vs. applied magnetic field for pure and doped BCPO, as determined from ^{31}P NMR signals.

distinct change in charamed to explore in detail the regime $\mu_0 H \geq 11$ T by means of ^{31}P NMcter with increasing H. While narro Our current project aiR, in particular at fields $H \geq H_c$. The NMR lineshapes for pure BCPO measured with H along the crystalline b-axis reveal a w at low fields, their growing widths at $H > H_c$ indicates a continuous distribution of the local magnetic field, typical of an incommensurate magnetic structure. In spite of the presence of defect-induced satellites, similar features of the lineshapes are observed for the doped compound. The variation of the ^{31}P NMR lineshapes across the covered field range (11–31 T) provided the boundaries of the FIO phase in the pure and doped BCPO, with extrapolated $T = 0$ K critical-field values $H_c = 20.96$ T and $H_c = 24.2$ T, respectively (see Fig. 3.1). The shift of the FIO boundary in the doped phase represents a unique feature due to disorder, never observed before.

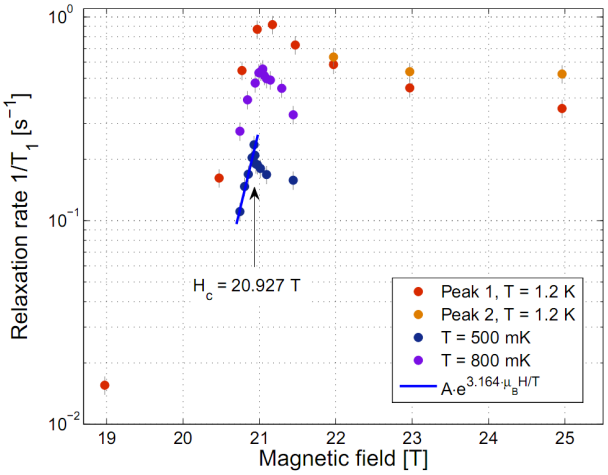

Figure 3.3: Maxima in NMR relaxation rates $T_1^{-1}(H)$ at constant temperatures for pure BCPO. The peaks indicate $H_c(T)$.

The characteristic asymmetry of the doubly-peaked line structure is most likely due to the Zeeman distortion of the helical magnetic structure in high fields. The first and second moments of the NMR lines increase linearly with H already in fields $H < H_c$, most likely indicating a Dzyaloshinskii-Moriya type anisotropy. The value of the second moment, or more simply the linewidth, may be used as a measure of the FIO order parameter. Related data, taken at $T = 1.4$ K are shown in Fig. 3.2; the onset of FIO is reflected in the sudden increase of the linewidth at the corresponding critical fields for $x = 0$ and $x = 0.01$, respectively. An identification of the FIO phase boundary is also possible from experiments probing the spin-lattice relaxation rate T_1^{-1}. At high fields, T_c may be obtained from distinct maxima in $T_1^{-1}(T)$ in a constant field H. For H close to H_c, however, the relaxation rates decrease dramatically overall. Therefore, measurements of $T_1^{-1}(H)$ at constant temperature are more suitable for observing the maxima in $T_1^{-1}(H)$. These were then used to identify the transition (see Fig. 3.3). As can be seen in Fig. 3.1, the phase boundaries, obtained by fits to the experimental data (indicated by open circles), are in both cases well represented by a power law of the form $T_c \propto (H - H_c)^{0.42}$. The exponent 0.42 is significantly lower than the expected value of 2/3 for 3D magnetic BEC transitions [1]. Reasons for this difference are currently explored. Attempts to establish the order configuration in fields exceeding H_c from detailed analyses of NMR line shapes and positions are also in progress.

3.2 Two-axis goniometer for low-temperature single-crystal NMR measurements

T. Shiroka, F. Casola, H.-R. Ott and J. Mesot
in collaboration with W. Bachmann (D-PHYS ETH Zurich)

During the past year we successfully completed the development and construction of a new NMR probe-head containing a two-axis goniometer intended for low-temperature single-crystal NMR measurements. Through the use of commercially available parts our probehead design (shown in Fig. 3.4) achieves a satisfactory angular resolution ($\pm 1^\circ$), while maintaining a high angular precision and the ability to orient samples down to liquid helium temperatures. With the new probehead we could measure the angular dependence of the main NMR parameters in anisotropic single crystals in several cases of scientific interest. A typical rotation plot is shown in Fig. 3.5, where ^{29}Si NMR spectra of the spin-chain compound $BaCu_2Si_2O_7$ exhibit a clear angular dependence as a function of the crystal orientation with respect to the applied magnetic field. A regular paper on these developments is currently in preparation.

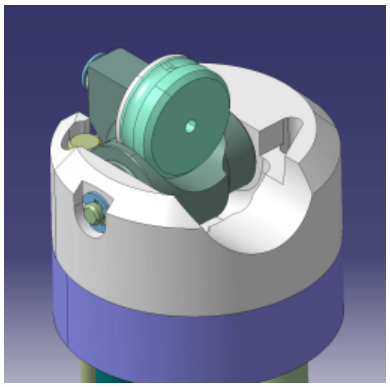

Figure 3.4: Goniometer head showing the two rotation axes. The central hole in the main disk is used for mounting the sample.

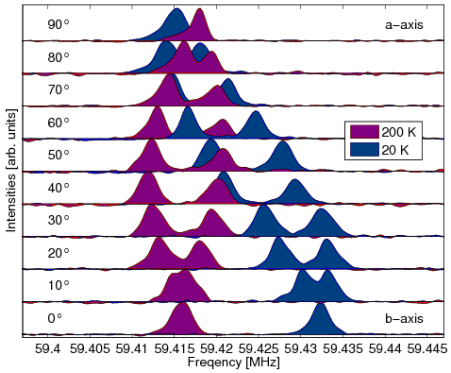

Figure 3.5: ^{29}Si NMR spectra of $BaCu_2Si_2O_7$ vs. the crystal angle against the 7 T applied field. A change in temperature from 200 K (red) to 20 K (blue) modifies the hyperfine interactions and, hence, the NMR spectra. Note the single lines observed along the (high-symmetry) a and b crystallographic axes, respectively.

References

1. T. Giamarchi, Ch. Rüegg, and O. Tchernyshyov, *Nature Phys.* **4**, 198 (2008).
2. S. Sachdev, *Nature Phys.* **4**, 173 (2008).
3. T. Shiroka, F. Casola, V. Glazkov, A. Zheludev, K. Prša, H.-R. Ott, and J. Mesot, *Phys. Rev. Lett.* **106**, 137202 (2011).
4. F. Casola, T. Shiroka, S. Wang, K. Conder, E. Pomjakushina, J. Mesot, and H.-R. Ott, *Phys. Rev. Lett.* **105**, 067203 (2010).
5. S. Wang, E. Pomjakushina, T. Shiroka, G. Deng, N. Nikseresht, Ch. Rüegg, H. M. Rønnow, and K. Conder, *J. Cryst. Growth* **313**, 51 (2010).
6. Ch. Rüegg, private communication.

Chapter 4

Nanoscale imaging and Nanoscale Magnetism

(http://www.microstructure.ethz.ch)

Head
Prof. Dr. D. Pescia

Academic Staff

Dr. T. Kirk (January-August)	L. De Pietro (PhD Student)	Dr. U. Ramsperger (Postdoc)
Dr. A. Vindigni(Postdoc)	H. Cabrera (PhD student)	D. Zanin (PhD student, starting July)

Technical Staff
Th. Bähler (80%)

Academic Guests
Prof. Dr. M. Erbudak
Prof. Dr. Mohamed El Gomati (University of York, UK, 09. January 2011)
Prof. Dr. Wolfgang Werner (Technical University of Vienna, Austria, 09.01.2011)
Prof. Dr. John Xanthakis (National Technical University of Athens, Greece, 09.01.2011)
Prof. Dr. Giovanni Stefani (Universita "Roma tre", Italy, 09.01.2011)
Dr. Ilona Müllerova (Institute of Scientific Instruments, Czech Republic, 09.01.2011)
Prof. Dr. Rafal Dunin-Borkowski (Technical University of Denmark, 09.01.2011)

4.1 Nanoscale Imaging

Technical characterization of Near Field-Emission Scanning Electron Microscopy

D. A. Zanin, H. Cabrera, L. De Pietro, M. Pikulski, M. Goldmann, U. Ramsperger, T.L. Kirk, D. Pescia

In the last years an instrument for surface microscopy has been developed, which we have called NFESEM (T.L. Kirk, "Near field-emission scanning electron microscopy", *in Applied Electron Microscopy - Angewandte Elektronenmikroskopie*, Vol. 9, Edited by J. Zweck, Logos Verlag, Berlin, 2010). In NFESEM electrons are emitted from a tip – placed at few tens of nanometers away from the surface to be investigated – via the field emission (FE) process, impinge and interact with the atoms at the surface of the sample and produce secondary electrons electrons (SE), which are ejected from the surface and can escape the strong electric field environment existing in the tip-surface region. By scanning the tip parallel to the surface, using the ultra-precise positioning techniques known from Scanning Tunneling Microscopy technology, and measuring the FE and/or SE current, a topographic image of the surface was obtained, with subnanometer spatial vertical resolution and few nanometers lateral spatial resolution. The bias voltage used in NFESEM is typically some 10 V: NFESEM is therefore a low voltage "scanning electron microscope" (SEM). So far, NFESEM was used to produce a set of images at characteristic surfaces, with the aim of demonstrating its feasibility and of checking its potential spatial resolution. No step was taken to understand the physical processes underlying the instrument in a quantitative way, like the number of SE electrons actually emitted from the surface and reaching the SE-detector, or the fundamental physical properties of the tip. This task was performed in the year 2011 by a set of Semester and Master theses. Some preliminary results are summarized here.

4.1.0.1 Primary beam generation

Typical field emitters are fabricated from cylindrical 99.98% (metals basis) polycrystalline tungsten (W) wires with a diameter of 0.250 mm. Our current tip preparation consists of two parts: a preparation in ambient conditions where the W-tip is effectively produced via an electrochemical etching technique, called here "ex-situ" preparation, and a heat treatment performed inside an UHV System and therefore called "in-situ" preparation. The shape of the tip as recorded by Scanning Electron Microscopy (left) and Transmission Electron Microscopy (right) is shown in the figure.

Quantitative determination of SE-yield

NFESEM, like every other SEM technique, needs to detect small electron currents originating from SE electrons. This is performed in our experimental set up by accelerating the SE electrons toward a scintillator. The SE impinging onto the scintillator produce electron-hole pairs, which recombining generate light quanta (typical quantum efficiency is about 2%). Next, the photons produced are guided through a light-pipe and are reconverted into electrons by a photocathode placed at the entrance of a Photo Multiplayer (PMT), with a quantum efficiency of about $5 - 20\%$. The photoelectrons are then accelerated to the first of a series of dynodes, which have a very high electron yield and effectively multiply the number of photoelectrons. The current exiting the PMT is converted into a voltage across a resistor. Thus, the SE electron current entering the detector is converted into an output voltage that is proportional to the input current. The key question yet unresolved about the SE-detection is the actual SE-yield. By this we mean – given a FE-current – which fraction of it is actually detected in the present set up. The SE-yield is actually the product of different quantities, none of which is measured individually in our experiment: the actual number of electrons excited, the effective angular and energy acceptance, and the performance of the SE-detector. For planning purposes, however, it turned out that the question of knowing at least the product of all these processes should be very telling about the actual efficiency of NFESEM technology. So we set up to calibrate our SE-detection in an ad-hoc built UHV calibration instrument, by using an electron beam of well-defined, known current and recording the corresponding output voltage, in order to establish the gain (V/A) of our SE-detection. The following figure

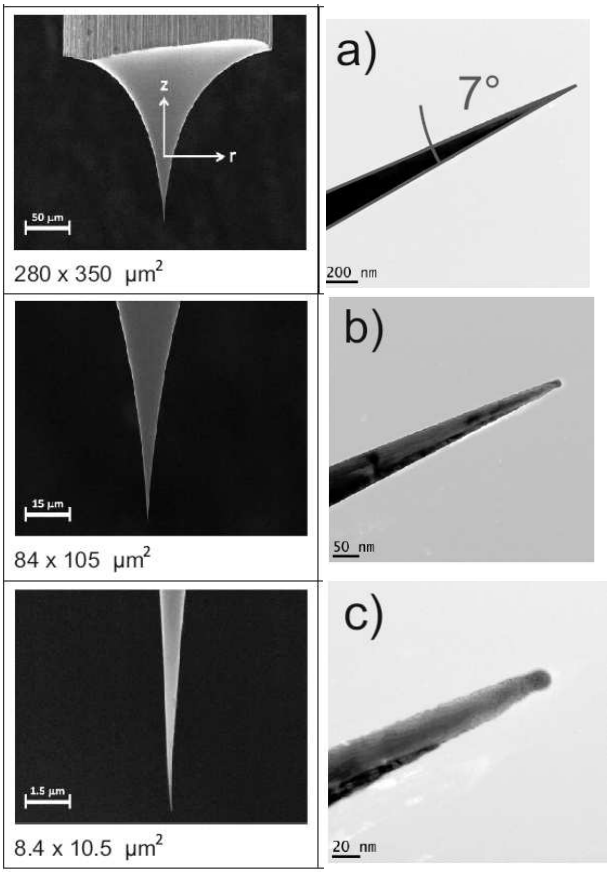

Figure 4.1: Typical FE tip observed at various spatial scales.

gives calibrated NFESEM images of a (110)-surface of a W(110)-single crystal. The scan range is given along the horizontal and vertical axes. The top image show the recorded field emission current averaged while the tip is scanned from left to right and from right-to-left. The bottom image, instead, displays the recorded SE-current. The images are rendered with a contrast based on a the grey scale given on the right of the images, which indictes the actually measured currents. All images show some strong current fluctuations which occur abruptly, and are probably due to some abrupt change in the field emission current due to sudden tip transformation. These changes are typically occurring while the tip is scanned along the horizontal direction, and thus appear at sharply defined horizontal lines. On the other hand, a set of fainter lines is also visible, which run approximately along the diagonal of the images and divide the images into almost parallel stripes. These are the monoatomic steps (step height ≈ 0.2 nm) separating the terraces which are well-known on the W(110)-surface. The calibrated images allows to read out an approximated, averaged SE-yield $\frac{<I_{SE}>}{<I_{FE}>} \approx 0.3\%$ (the symbol $<>$ means average over the image).

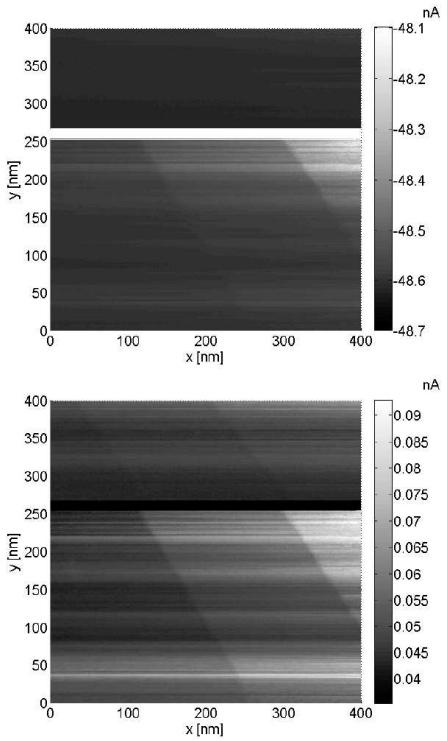

Figure 4.2: FE (top) and SE (bottom) NFESEM images of a W(110)-surface

4.2 Nanoscale Magnetism

Static and dynamic properties of single-chain magnets with sharp and broad domain walls

O.V. Billoni, V. Pianet, D. Pescia, A. Vindigni, Phys. Rev. B, **82**, p. 064415 (2011)

The interest in the physics of domain walls in 1d model magnetic systems originate from the possibility of moving them in single chain magnets or nanowires using an applied magnetic field or an injected current, with the aim of performing logic operations, see e.g. "Magnetic Domain-Wall Racetrack Memory", Stuart S. P. Parkin, Masamitsu Hayashi and Luc Thomas, Science **320**, 190, (2008)). A still unresolved question – both experimentally and theoretically – is the role of temperature during the domain wall motion. In particular, the thermal diffusion of domain walls affect the stability of domains in single chain magnets and thus limits their application as magnetic storage units and for controlled domain motion. The quest to improve thermal stability of single chain magnets and 1d-wires calls for a better understanding of their physical static and dynamic properties. We have started a theoretical work in this direction and here we report some essential results obtained in 2011.
As a reference model for 1d magnet we consider the following classical Heisenberg Hamiltonian:

$$H = -\sum_{i=1}^{N} \left[J\vec{S}_i \cdot \vec{S}_{i+1} + D(S_i^z)^2 + \vec{H} \cdot \vec{S}_i \right] \tag{4.1}$$

where D represents the anisotropy energy, favoring the z-direction, J is the ferromagnetic exchange coupling and $\vec{H}$ an external applied field. Each spin variable $\vec{S}_i$ is a three-component unit vector associated with the i–th lattice point. This model sustains two types of domain walls: a "sharp" domain wall and a "broad " domain wall, see the figure. In the figure we plot the domain wall energy ε_{dw} as a function of the ratio $\frac{D}{J}$, obtained from a discrete-lattice calculation (solid line), and from transfer matrix respectively time-quantified Monte Carlo calculations (crosses and circles). Most remarkably, for $D/J \leq 2/3$, the minimal DW energy is realized by a spin profile in which several spins are not aligned along the easy axis, z (see the sketch in the inset up on the left): in this case, DWs spread over more than one lattice spacing and we speak of a *broad* DWs. For $D/J > 2/3$, the minimum DW energy is realized if the transition between $S_i^z = +1$ to $S_i^z = -1$ occurs within one lattice spacing: we speak of a *sharp* DWs (see the sketch in the inset down on the right). Most remarkably, the transition between the two types of walls is well defined, as shown by the singularity of the curve in the figure.

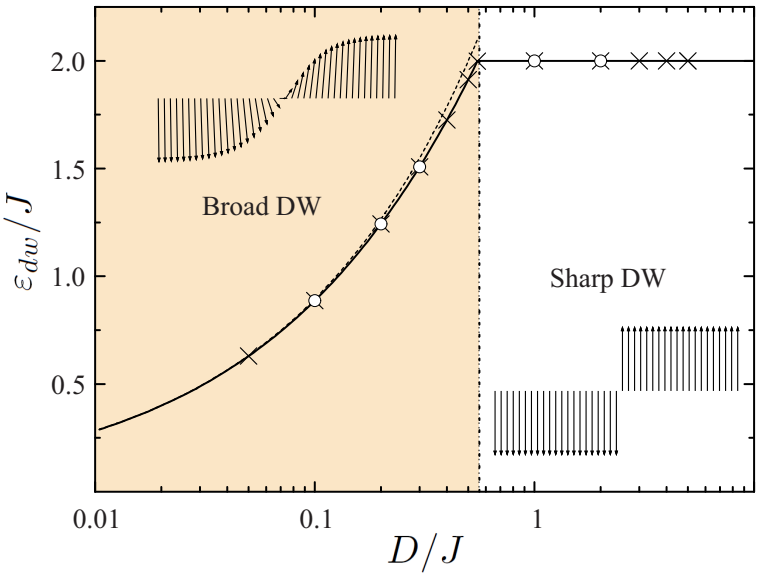

Figure 4.3: Energy of a domain wall as a function of the strength of the magnetic anisotropy. The transition form "sharp" to "broad" is well defined.

The main question we started to address – using a combination of analytical methods, transfer matrix and time resolved Monte Carlo calculations – is the following: are physical properties of domain walls in 1d magnets affected by the sharpness of the domain wall? Our results show indeed that there are conspicuous differences between the two limits, like e.g. the diffusion coefficient for thermally driven domain wall motion, which follows an Arrhenius behavior as a function of the temperature, with a finite activation energy in the sharp wall regime. In the broad wall regime, instead, the diffusion coefficient does not follow an activated mechanism but rather grows linearly with temperature, reminding the behavior of a particle in a viscous medium. Further results are expected when the temperature is properly taken into account within a full dynamical Landau-Lifschitz equation.

Chapter 5

Optical and Magneto-optical Spectroscopy

(http://www.solidphys.ethz.ch/spectro)

Head
Prof. Dr. L. Degiorgi

Academic Staff
Dr. A. Lucarelli Dr. C. Mirri A. Dusza

Administrative Staff
I. Mettler

5.1 Anisotropic in-plane optical conductivity in detwinned $Ba(Fe_{1-x}Co_x)_2As_2$

A. Dusza, A. Lucarelli and L. Degiorgi

work in collaboration with J.-H. Chu, H.-H. Kuo and I.R. Fisher, Stanford University, California, U.S.A.

In many unconventional superconductors including cuprates and Fe-based pnictides, superconductivity emerges from a complicated soup of competing phases in the normal state when magnetism is suppressed by doping, pressure or other external parameters. This multiplicity of phases includes nematicity, defined as the spontaneously broken C4 rotational symmetry of the square lattice, and a novel form of magnetism, arising from either orbital currents or antiferromagnetic fluctuations. In the Fe-based pnictide superconductors, nematic correlations and antiferromagnetic fluctuations have also been recently connected with symmetry breaking competing phases.

Measurements of the dc resistivity as a function of temperature of the single domain (detwinned) parent compounds $BaFe_2As_2$, $SrFe_2As_2$ and $CaFe_2As_2$ (i.e., so called 122 iron pnictides) reveal a modest in-plane dc anisotropy for temperatures below the structural tetragonal-orthorhombic transition at T_s, with the resistivity in the ferromagnetic direction (orthorhombic b-axis) larger than along the antiferromagnetic direction (orthorhombic a-axis). The transport properties revert to an isotropic in-plane conductivity once the structural transition is completely suppressed upon doping. For temperatures above T_s, single domain $BaFe_2As_2$ specimens display a persisting band splitting and a large induced in-plane resistivity anisotropy that is not observed for overdoped compositions. Both thermodynamic and transport measurements do not support an additional phase transition above T_s for unstressed crystals, so that the induced anisotropy above T_s is the result of a large nematic susceptibility. The structural transition breaks the four-fold symmetry of the high-temperature lattice and thus leads to an anisotropic conducting state. This broken rotational symmetry is consequently expected to have a direct impact in the optical properties.

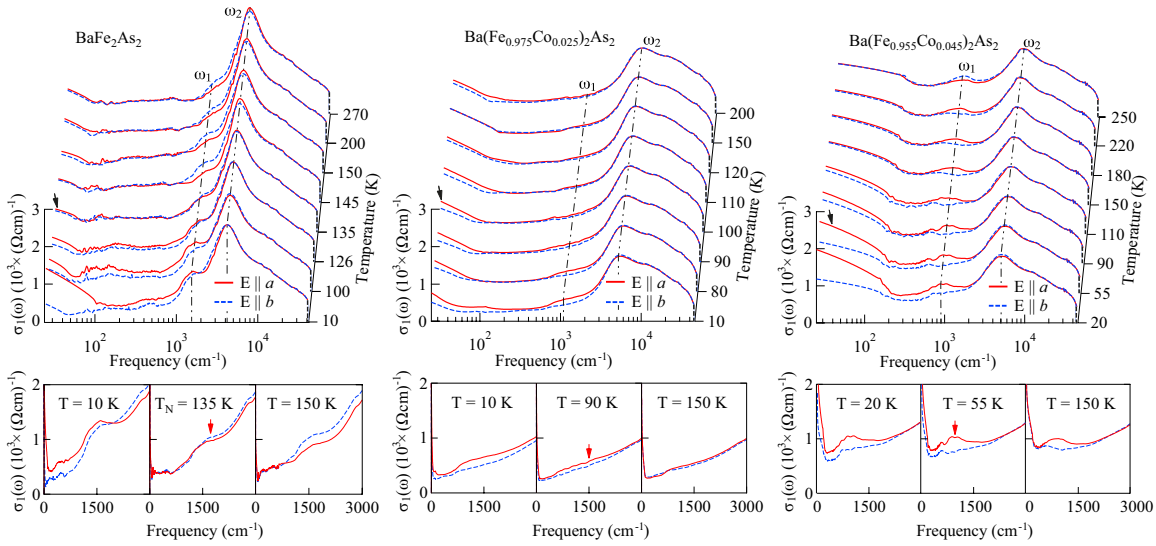

Figure 5.1: Temperature dependence of the optical conductivity of detwinned $BaFe_2As_2$, $Ba(Fe_{0.975}Co_{0.025})_2As_2$ and $Ba(Fe_{0.955}Co_{0.045})_2As_2$ in the whole measured spectral range for two polarizations, parallel to the a-axis direction (E$\|a$, red solid line) or perpendicular to it (E$\|b$, blue dashed line). The black arrows indicate $\sigma_1(\omega)$ at the temperature close to the structural phase transition at T_s, while the red arrows (bottom panels) indicate the center of the MIR-band close to T_N. The dashed-dotted and dashed double-dotted line (top panels) mark the frequency ω_1 and ω_2 (see text).

We study the anisotropic in-plane optical conductivity of detwinned $Ba(Fe_{1-x}Co_x)_2As_2$ single crystals for x=0, 2.5% and 4.5% in a broad energy range (3 meV-5 eV) across their structural and magnetic transitions. Detwinned specimens were achieved with the crystal held under uniaxial pressure. Figure 5.1 shows the real part $\sigma_1(\omega)$ of the optical conductivity of detwinned $Ba(Fe_{1-x}Co_x)_2As_2$ for different temperatures along both polarization directions. In the visible and UV energy interval $\sigma_1(\omega)$ is characterized by polarization independent broad absorption bands which overlap with a dominant NIR contribution peaked at about 5000 cm^{-1}. The temperature and doping dependent optical anisotropy in $\sigma_1(\omega)$ is mainly evident in the FIR and MIR regions. In the FIR region, there is a strong polarization

dependence of the itinerant charge carriers contribution to $\sigma_1(\omega)$. Along the a-axis $\sigma_1(\omega)$ shows a more pronounced metallic behavior which gets enhanced below the magnetic phase transition at T_N ($\leq T_s$), leading to the stripe-like spin order pointed out above. Along the b-axis $\sigma_1(\omega)$ below T_N is depleted due to the formation of a pseudogap, prior to displaying a metallic-like upturn for $\omega \rightarrow 0$. The strong absorption peak dominating $\sigma_1(\omega)$ at about 5000 cm^{-1} develops into a pronounced shoulder on its MIR frequency tail at about 1500 cm^{-1}. This latter MIR-band in $\sigma_1(\omega)$ shows a strong polarization and doping dependence, as highlighted in Fig. 5.1 (bottom panels). Interestingly enough, for increasing doping the maximum of the MIR-band shifts to lower frequencies indicating that the MIR-band is significantly affected by the doping (dotted-dashed lines in top panels and red arrows in the bottom panels of Fig. 5.1).

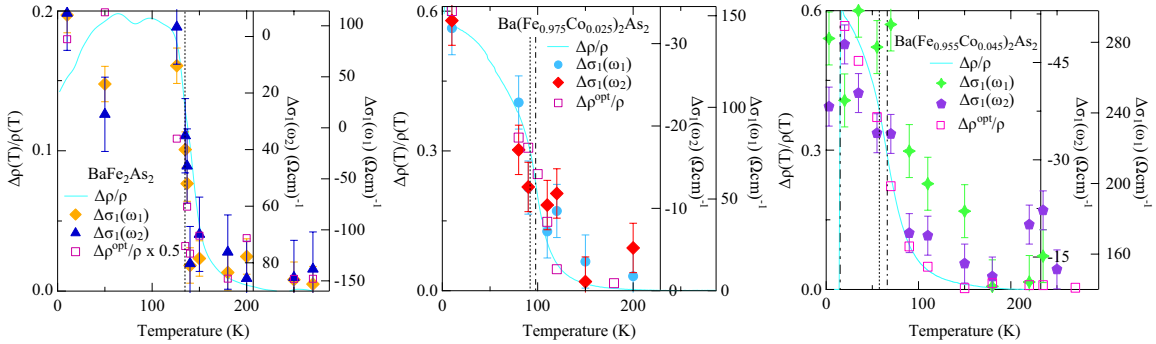

Figure 5.2: Temperature dependence of the dichroism $\Delta\sigma_1(\omega)$ of $BaFe_2As_2$, $Ba(Fe_{0.975}Co_{0.025})_2As_2$ and $Ba(Fe_{0.955}Co_{0.045})_2As_2$ at ω_1 and ω_2 (Fig. 5.1) compared to $\frac{\Delta\rho}{\rho}$ obtained from the dc transport data, as well as from the metallic (Drude) contribution in $\sigma_1(\omega)(\Delta\rho^{opt}/\rho)$. The vertical dotted-dashed, dotted and double-dotted-dashed lines mark the structural, magnetic and superconducting phase transitions at T_s, T_N and T_c, respectively.

It is especially interesting to compare the temperature dependence of the dc ($\frac{\Delta\rho}{\rho}$=$\frac{2(\rho_b-\rho_a)}{(\rho_b+\rho_a)}$) and optical ($\Delta\sigma_1(\omega) = \sigma_1(\omega, E \parallel a) - \sigma_1(\omega, E \parallel b)$) anisotropy. Two characteristic frequencies, identifying the position of the peaks in $\sigma_1(\omega)$ (Fig. 5.1), are selected in order to follow the temperature dependence of $\Delta\sigma_1(\omega)$; namely, ω_1=1500 cm^{-1} and ω_2=4300 cm^{-1} for $x = 0$; ω_1=1320 cm^{-1} and ω_2=5740 cm^{-1} for $x = 0.025$; ω_1=912 cm^{-1} and ω_2=5182 cm^{-1} for $x = 0.045$. It is remarkable that the temperature dependence of $\Delta\sigma_1(\omega)$ at ω_1 and ω_2 follows the temperature dependence of $\frac{\Delta\rho}{\rho}$ in all compounds, extracted from the dc properties and from the metallic contribution in $\sigma_1(\omega)$ (Fig. 5.2). $\Delta\sigma_1(\omega_i)$ ($i = 1, 2$) saturates at constant values well above T_s and then displays a variation for $T < 2T_s$. Here we first underscore that the rather pronounced optical anisotropy, extending up to temperatures higher than T_s for the stressed crystals, clearly implies an important pressure-induced anisotropy in the electronic structure, which is also revealed by ARPES measurements. Significantly, the absolute variation of the dichroism across the transitions at selected frequencies is larger for x=0 than for x=0.025 and 0.045, contrary to the anisotropy in the dc resistivity. This could imply that changes in the electronic structure follow a similar trend to doping as the lattice orthorhombicity.

We also compare our optical results with the outcome of the full-potential linear augmented plane-wave (LAPW) calculations. Figure 5.3 shows the low temperature measured (top panels) and calculated (bottom panels) optical conductivity for both the a- and b-axis and for the three dopings. For a direct comparison we have normalized all the measured and calculated $\sigma_1(\omega)$ to their respective maxima, thus obtaining $\tilde{\sigma}_1(\omega)$. The overall anisotropy of $\sigma_1(\omega)$ at low temperatures as well as the general features, like the MIR (black arrows in Fig. 5.3) and NIR absorption bands, are fairly well caught by the calculation. The predictions of the enhancement of the MIR-band and the metallic contribution of $\sigma_1(\omega)$ in the FIR range along the a-direction and their depletion along the b-direction are indeed fairly close to the experimental findings. Moreover, the center of the calculated MIR-band (black arrows in Fig. 5.3 bottom panels) shifts at lower frequencies for increasing dopings which also mimics the data. The MIR-band is linked to the modeled magnetic stripe configuration which was shown to correspond to the energy-minimum configuration of these systems. Therefore, the LAPW calculation strongly supports a "magnetic origin" of the MIR-band which would originate from the Fermi topology reconstruction in the magnetically ordered state.

Summarizing, for temperatures below the Neel transition, the topology of the reconstructed Fermi surface mainly determines the anisotropy of the low frequency optical response. For temperatures above T_s, uniaxial stress leads to

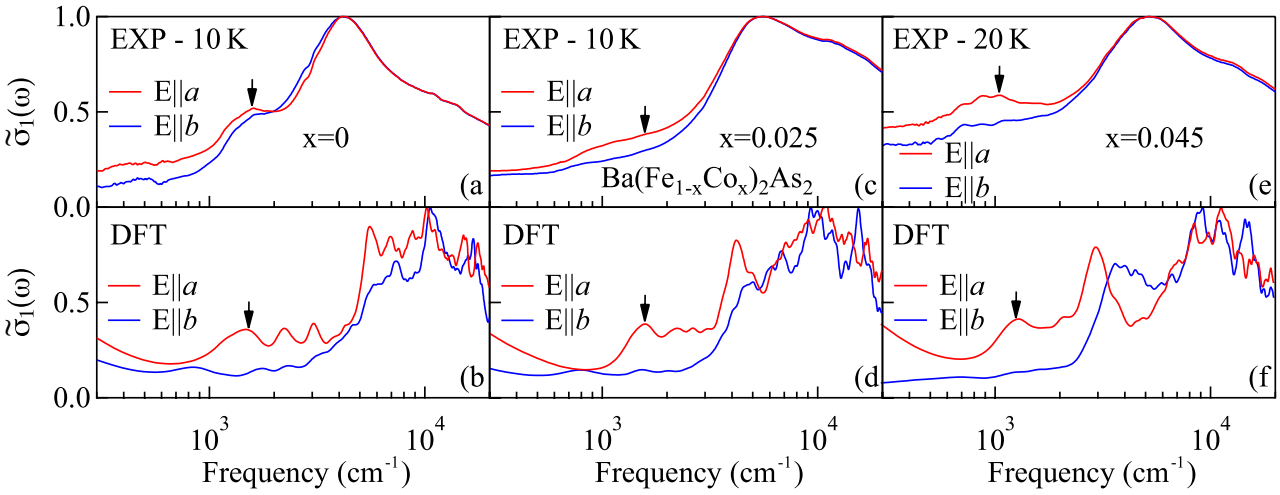

Figure 5.3: Normalized optical conductivity $\tilde{\sigma}_1(\omega)$ of $BaFe_2As_2$ (a,b), $Ba(Fe_{0.975}Co_{0.025})_2As_2$ (c,d), and $Ba(Fe_{0.955}Co_{0.045})_2As_2$ (e,f) measured (top panels) at the lowest temperatures with light polarized along the a- and b-axis and obtained by DFT calculations (bottom panels) along the antiferromagnetically oriented spins and parallel to the ferromagnetic stripes. The black arrows indicate the MIR-band in the measurements and calculations.

a finite in-plane anisotropy. The anisotropy of the optical conductivity, leading to a significant dichroism, extends to high frequencies in the mid- and near-infrared regions. The temperature dependence of the dichroism at all dopings scales with the anisotropy ratio of the dc conductivity, suggesting the electronic nature of the structural transition. Our findings bear testimony to a large nematic susceptibility that couples very effectively to the uniaxial lattice strain. In order to clarify the subtle interplay of magnetism and Fermi surface topology we compare our results with theoretical calculations obtained from density functional theory within the LAPW method, discovering a rather astonishing agreement between theory and experiment.

5.2 Incommensurate magnetic order in $TbTe_3$

F. Pfuner and L. Degiorgi

work in collaboration with S.N. Gvasaliya, O. Zaharko, L. Keller, J. Mesot, V. Pomjakushin, ETH Zuerich and PSI Villigen, Switzerland, and J.-H. Chu and I.R. Fisher, Stanford University, California, U.S.A.

The RTe_3 family of compounds (R=rare earth) have recently attracted renewed interest as a model system for layered (two-dimensional) charge-density-wave (CDW) materials. RTe_3 crystallizes in an orthorhombic structure, composed of double layers of planar Te-sheets separated by corrugated R-Te layers. The average chemical structure can be described using the $Cmcm$ space group (in this setting the lattice parameters a and c are close to each other, whereas b is approximately 6 times longer). A CDW state with modulations along the c-axis is present in all RTe_3 materials. However, the members with the heaviest rare-earth elements exhibit a second CDW phase transition at lower temperatures that is characterized by a modulation wavevector $q_a \sim 1/3a^*$. The critical temperatures of these two CDW transitions show opposite trends as a function of the R-atom mass. Whereas T_{CDW1} decreases towards heavier members of the family (*i.e.*, going from La to Tm), the T_{CDW2} associated with the a- axis incommensurability is higher for heavier compounds. For the specific composition addressed in our study, $TbTe_3$, transport and diffraction experiments yield T_{CDW1} = 336 K. Although transport measurements do not clearly reveal the presence of a second CDW transition, STM measurements performed at 6 K do show an ordering pattern that is associated with the wavevector $\sim 2/3a^*$. More recent high resolution x-ray diffraction measurements confirm the presence of a transverse CDW at low temperatures, with wave-vector $\sim 0.683a^*$, though T_{CDW2} is at present unknown.

In addition to hosting an incommensurate CDW, RTe_3 also hosts long range antiferromagnetic order at low temperatures for magnetic rare earth ions. The magnetic phase transitions of RTe_3 have been studied using magnetisation,

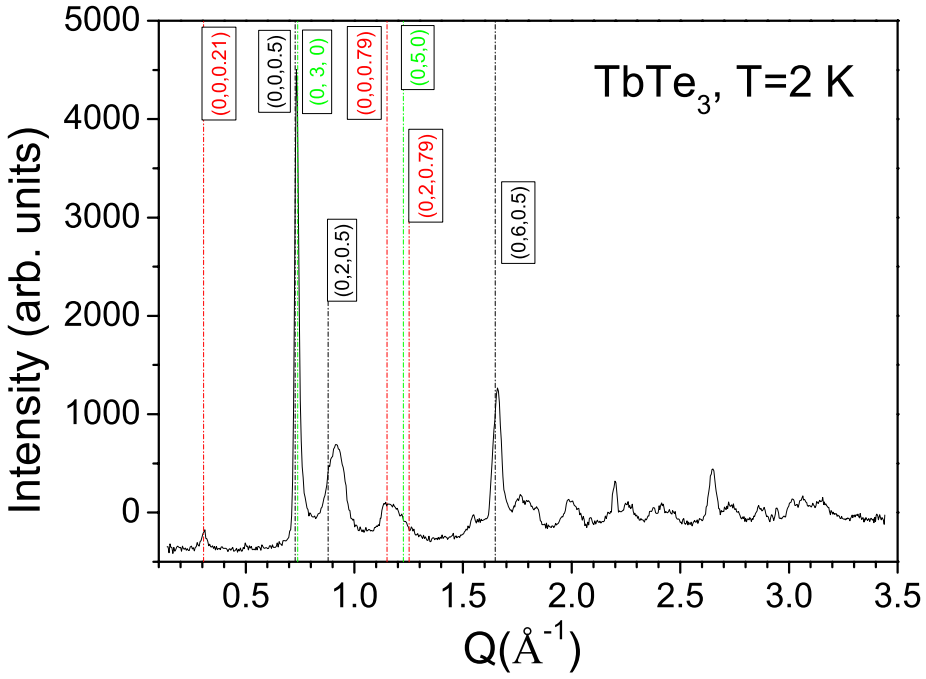

Figure 5.4: Indexed magnetic reflections for $TbTe_3$ at 2 K in a powder diffraction pattern (the contribution from the chemical structure is eliminated by subtracting the powder spectrum taken at T=60 K). The indexed peaks were identified by single-crystal neutron diffraction experiments. Labels in the brackets are the (H, K, L) indices of the peaks given in terms of the average $Cmcm$ structure. The peaks that are associated with the magnetic propagation vector $q_{mag1} = (0, 0, 0.21)$ are labeled in red, those associated with the magnetic propagation vector $q_{mag2} = (0, 0, 0.5)$ are shown in black, and finally, with $q_{mag3} = (0, 1, 0)$ - in green. Note that the Bragg peaks, that are labeled for simplicity as $(0, K, L) \pm (0, 0, 0.21)$, in fact have a non-zero component of modulation along the $(< 0, K, 0 >)$ direction and more precisely should be described as $(0, K, L) \pm (0, 0.01, 0.21)$.

calorimetry and electrical resistivity. However, the nature of the long-range magnetic order in this family of compounds has not yet been studied by diffraction techniques, and the effect of the incommensurate lattice modulation on the magnetic structure is unknown. To bridge this gap we have performed neutron scattering experiments in the representative compound $TbTe_3$, which exhibits three closely located magnetic phase transitions at the following temperatures: T_{mag1} = 5.78 K, T_{mag2} = 5.56 K and T_{mag3} = 5.38 K.

Figure 5.4 shows the magnetic diffraction pattern measured in $TbTe_3$ at 2 K. Some of the magnetic peaks could be indexed in terms of the average chemical cell and are labeled in Fig. 5.4 (due to the complexity of the pattern the use of single-crystal neutron diffraction data was essential for this step). Clearly, most of the magnetic Bragg peaks are at positions incommensurate with the average chemical structure of the material. It may be speculated that the broad magnetic peaks observed in the vicinity of $Q \simeq 0.9$Å and $Q \simeq 1.2$Å are composed by many magnetic Bragg peaks which are located close to each other in wave-vector space, due to the rather large value of the lattice parameter b.

Figure 5.5 shows false-color maps of neutron intensities taken in a close vicinity of the $(0, 0, 0.21)$ incommensurate magnetic reflection in the temperature range $1.5 - 6$ K. At the base temperature this reflection has incommensurate components both along the $< 0, K, 0 >$ and $< 0, 0, L >$ directions. However, the incommensurate component along the $< 0, K, 0 >$ direction appears to be small and diminishes above T_{mag3} in a step-like way. Above T_{mag3} the incommensurate components along the $< 0, 0, L >$ direction is also temperature-dependent. For a more quantitative analysis the scans for each temperature are fitted assuming a Gaussian shape for a Bragg reflection. The resulting temperature dependence of the position and intensity of the peak $(0, 0, 0.21)$ is shown in Fig. 5.6. The modulation vector along the $< 0, 0, L >$ direction stays constant within the precision of the measurements below T_{mag3}. Above T_{mag3} the propagation vector increases smoothly and reaches the value of $(0, 0, 0.242 \pm 0.001)$ at T_{mag1}. The modulation vector along the $< 0, K, 0 >$ direction is also constant $(0, 0.01 \pm 0.001, 0)$ below T_{mag3}, while above this temperature

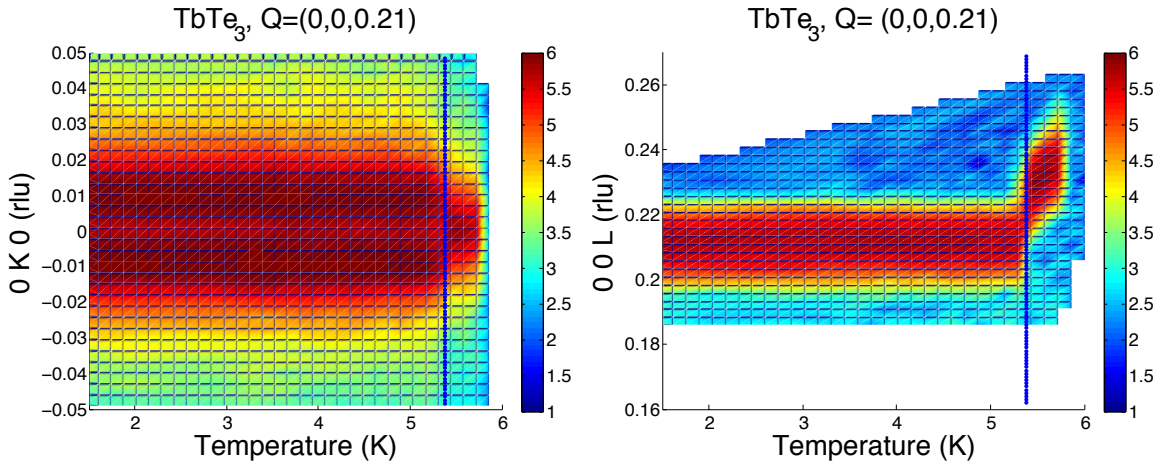

Figure 5.5: The temperature evolution of the intensity distribution taken in the vicinity of the (0,0,0.21) position of $TbTe_3$. Vertical solid lines on both plots denote T_{mag3} = 5.38 K. Note that below T_{mag3} the reflection is incommensurate in both $< 0, K, 0 >$ and $< 0, 0, L >$ directions.

the component of the modulation vanishes. The intensity measured around the $(0, 0, 0.21)$ position appears to be nearly temperature-independent below T_{mag3}. Above this temperature however, the overall intensity observed in the vicinity of the $(0, 0, 0.21)$ position drops by a factor of 2, as can be deduced from Fig. 5.6b-d. Further the intensity gradually decreases and above T_{mag1} we could not detect any scattering above the background level around that position. In the whole studied temperature range the width of the peaks is limited by resolution. Gradual decrease of the Bragg intensity suggests a continuous character of the phase transition that the crystal undergoes at T_{mag1}, whereas an abrupt change in magnetic intensity at T_{mag3} points to a first order phase transition.

Summarizing, a long-range incommensurate magnetic order emerges in $TbTe_3$ at T_{mag1} = 5.78 K as a result of continuous phase transitions. We observe that near the temperature T_{mag1} the magnetic Bragg peaks appear around the position (0,0,0.24) (or its rational multiples), that is fairly close to the propagation vector $(0, 0, 0.29)$ associated with the CDW phase transition in $TbTe_3$. This suggests that correlations leading to the long-range magnetic order in $TbTe_3$ are linked to the modulations that occur in the CDW state.

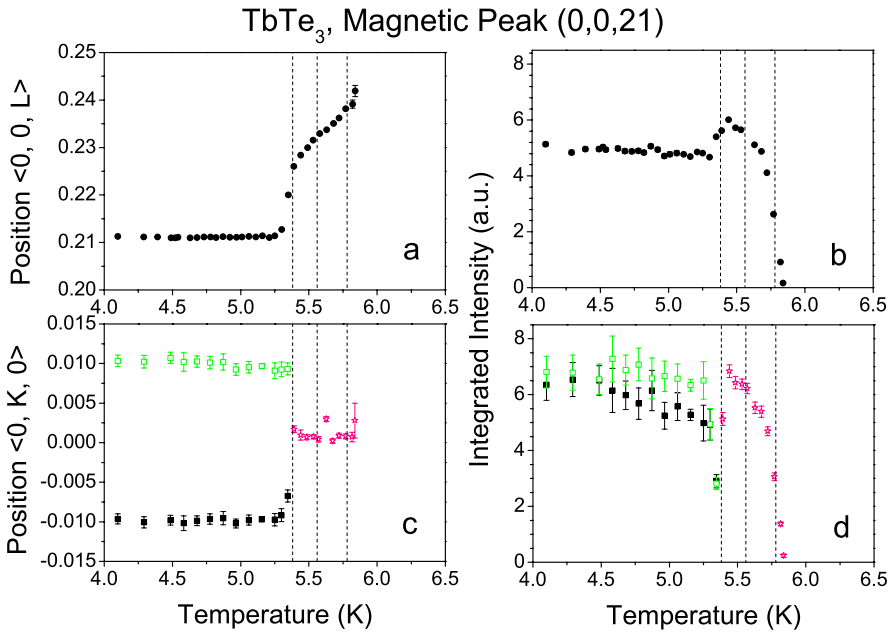

Figure 5.6: The temperature evolution of the propagation vectors (left column) and of the intensity (right column) measured around the position (0,0,21). Green symbols denote the position and the intensity of the (0,0 + δ,0.21) satellite, whereas black squares stand for the (0,0 − δ,0.21). Vertical dashed lines denote the temperatures of the magnetic phase transitions.

Chapter 6

Solid-State Dynamics and Education

(http://www.eduphys.ethz.ch/)

Head
Prof. Dr. A. Vaterlaus

Academic Staff
Dr. Yves Acremann
Audra Baleisis
Andreas Fognini
Dr. Christian Helm
Andreas Lichtenberger
Dr. Thomas Michlmayr
Martin Mohr
Gerard Salvatella-Orgilles
Dr. Guillaume Schiltz
Dr. Clemens Wagner

Master Students
Christoph Wetli

Technical Staff
Thomas Bähler

6.1 Formative Assessment in High School Teaching of Physics

A. Lichtenberger, C. Wagner, A. Vaterlaus

Among a few other techniques formative assessment has been recognized as one of the most promising tools to improve teaching. It has a very broad definition, which has been recently summarized in five tenets (D. Wiliam in "The Nature of Learning". Edited by Dumont H, Istance D, Benavides F, OECD, 2010.)

1. Engineering classroom activities that elicit evidence of learning
2. Clarifying, sharing and understanding learning intentions and criteria for success
3. Providing feedback that moves learners forward
4. Activating students as instructional resources of each other
5. Activating students as owners of their own learning

Based on these tenets we have derived a model of formative assessment, which can be applied to high school teaching of physics. It consists of four different strategic lines (see Fig. 6.1).

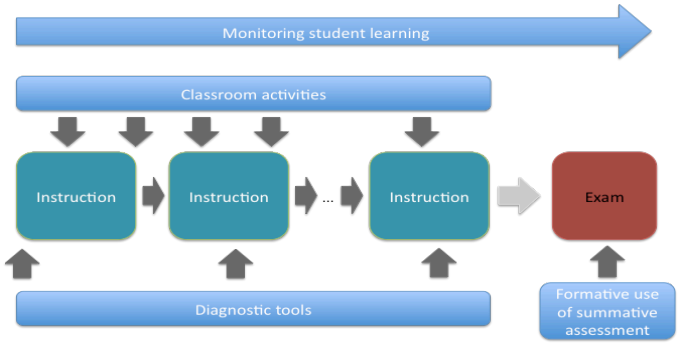

Figure 6.1: Model of formative assessment. It is composed of four lines, the formative classroom activities (fostering conceptual thinking), the monitoring tool (students self-assessment), the diagnostic tool (detection of misconceptions) and the formative use of summative assessment.

First, regular instructions have to be supplied with formative classroom activities. These activities pursue different goals. They provide direct feedback for the student about how he has absorbed the new material. The teacher immediately gets feedback about the effectiveness of his instructions. However, since formative activities focus on concept learning they also shift the teaching goal from solving numerical problems towards understanding physics concepts. Central to formative assessment is that students self-assess their own learning. It is important that students can estimate the difference between their actual knowledge and the learning goals. To support this kind of self-reflection we develop a monitoring tool, which allow the students to assess the difference in an easy and efficient manner. The diagnostic tool is used to verify the impressions about teaching and learning teachers and students have. It is designed to detect the proper acquisition of concepts, however, also misconceptions are detected, which are still present. To eliminate the misconception all applications of a diagnostic tool are followed by a reflective lesson. During these lessons students have time to work on specific concepts and to catch up. The detailed analysis of concept knowledge and misconceptions is one of the main goals in our implementation of the model. Not only students get an individual feedback but also the teacher gets a feedback about the performance of the class. This feedback should be used to remove ambiguities from teacher's instructions to make them as clear as possible.

6.2 A model of concept learning

C. Wagner

In order to get a better understanding of concept learning and in particular of misconception unlearning we started to model this transition. Our new approach consists of two variables, one for the concept and one for the misconception. The evolution of a concept has a learning term and an unlearning term. The same also holds for the evolution of misconceptions. However, learning of concepts is hampered in the presence of strong misconceptions and misconceptions foster the unlearning of concepts. In contrast, solid concepts suppress the development of misconceptions. Putting these conditions into mathematical terms we get a model to simulate the transition from a high misconception and a low concept level (misconception fixed point) to a low misconception and a high concept level (concept fixed point). The model was then fitted to a data set recorded by Andrew Heckler and Eleanor Sayre (Am. J. Phys. 78 (2010) 768-777). The authors investigated concept learning at the undergraduate level at the University of Ohio. Every few days different students (in the average 12) were asked to solve the same problem in electric circuit theory. We used the time course of concept learning to determine the parameters of the model (see Fig. 6.2).

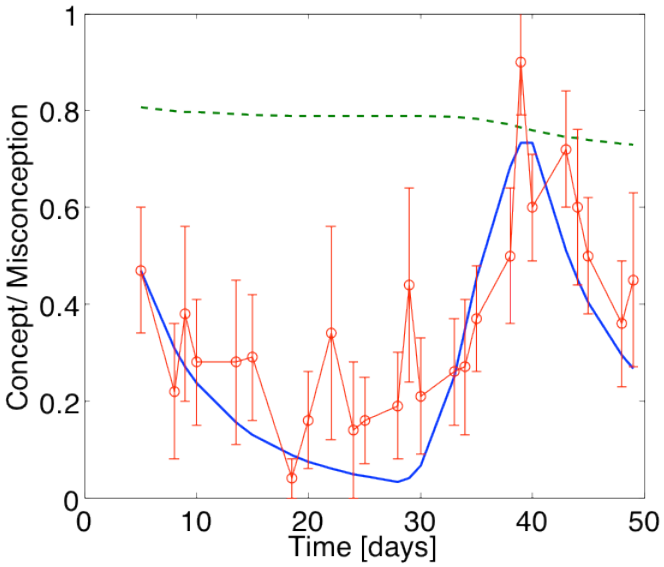

Figure 6.2: Concept learning. Data points (red circles) are obtained by A. Heckler et al. The blue line corresponds to the fitted concept level whereas the green dashed line represents the misconception level. Lecturing electric circuit theory took place between day 28 until day 39.

6.3 E-Learning and teaching support

G. Schiltz, A. Vaterlaus

6.3.1 Strategic activities

21 courses have been supplemented by the learning management system Moodle in 2011. 12 introductory lectures (service and internal), 4 teacher training courses and 5 MSc lectures with a total of 3575 students were affected. Moodle was mainly used to support the course organization and to serve as a repository for course material. For some lectures, however, supplementary pedagogical scenarios, such as self-assessment tests, formative evaluations and collaborative tasks have been set up. Two training sessions, one for teaching assistants in exercise classes and one for teaching assistants in laboratory classes have been developed and carried out in 2011 by members of the LFKP in co-operation with the LET (Lehrentwicklung und Technologie). 18 participants successfully participated in these courses.

6.3.2 Innovedum/Filep projects

The following projects ended in 2011. Based on the positive results achieved during the funding period, all of them are now transferred to the regular teaching portfolio.

- ”Fachdidaktik II” (A. Vaterlaus).
- ”Erweiterte Physik-Vorlesungsexperimente” (B. Batlogg).
- ”Brückenpodcast” (W. Wegscheider).

6.3.3 Learning support

Concept questions as formative assessment tools were successfully used in 5 lectures (fig 6.3).

Figure 6.3: Students answering concept questions with flash cards

Summary podcasts (audio/visual weekly summary) were provided for 4 lectures (fig 6.4).

6.3.4 Promotion and Network

The teaching activities pursued at the department have been communicated to a greater public (3 conference presentations, 2 community presentations). Results related to the summary podcasts were discussed in two publications: Schiltz, G. / Brändle U. / Reinhardt, A. / Valkering, M. (2011) Lehr- und Lerntechnologie an der ETH Zürich. In:

Figure 6.4: Weekly summary podcast on iPhone

Dittler U. (ed.): E-Learning: Einsatzkonzepte und Erfolgsfaktoren des Lernens mit interaktiven Medien, 3rd edition. München: Oldenbourg, p. 35-47. Schiltz, G. (2011) Bridging lectures with summary podcasts. In: Yu, Fu-Yun et al. (eds.): Proceedings of the 19th International Conference on Computers in Education ICCE 2011: November 28, 2011 - December 2, 2011 : Chiang Mai, Thailand. Chiang Mai: National Electronics and Computer Technology Center, p. 771-773.

6.4 Ultrafast demagnetization observed by spin resolved photoemission spectroscopy

A. Fognini, T. Michlmayr, G. Salvatella, C. Wetli, U. Ramsperger, Y. Acremann, A. Vaterlaus

in collaboration with

C. Stamm, M, Beye, A. Eschenlohr, A. Föhlisch (Helmholtz Zentrum Berlin)

F. Sorgenfrei, M. Dell'Angela, W. Wurth (University of Hamburg)

N. Gerasimova (DESY)

S. de Jong, R. Kureja, A. Scherz, J. Stöhr, H.A. Dürr (SLAC)

J. Raabe (PSI)

G. Schönhense (University of Mainz)

Magnetism and its dynamical properties are at the basis of our information society. On long time scales and large length scales ferromagnetic cores of transformers prove essential for the electric power grid. On the nanosecond and nanometer scale magnetic domains are used to store information on hard disk drives. One of the forefront areas in modern magnetism is the use of ultrashort infrared or optical photon pulses to manipulate the magnetization. It has been observed that the magnetization of a ferromagnet seams to drop within less than a picosecond after excitation by a femtosecond laser pulse. This phenomenon is surprising as demagnetization requires the transfer of angular momentum from the spin system to the lattice of the solid. At room temperature the spin orbit coupling is expected to be too weak to explain ultrafast demagnetization.

Since optical photons trigger the sample through electronic excitations, the fundamental questions revolve around the processes and timescales associated with energy and angular momentum transfer between the three fundamental thermodynamic reservoirs of the sample: the electronic system, the spin system and the lattice. The sum of the magnetic moment of all the electrons forms the magnetization, which is macroscopically measurable. Only a small fraction of the electrons close to the Fermi energy is relevant for the transport aspects of magnetism. These electrons cause phenomena like giant magneto-resistance and the magneto-optical Kerr effect. In thermal equilibrium magneto-optical Kerr measurements show the spin polarization of electrons close to the Fermi energy, which is proportional to the magnetization of the solid. In the case of ultrafast demagnetization processes it is not clear if the electrons close to the Fermi energy loose their spin polarization at the same time as all the other valence electrons.

The most direct way of measuring demagnetization processes is to detect the spin polarization of photoelectrons. All other optical methods like magneto-optical Kerr as well as circular dichroism measurements depend on the delicate band structure of the valence band, which is altered by the infrared pump beam. In contrast spin polarized photoelectron spectroscopy offers direct insight into the true magnetization of the ferromagnet. In order to obtain a reliable measure of the magnetization, which is a Brillouin zone average over all filled spin polarized band states, one needs to employ high-energy "probe" photons in the form of the soft x-rays available at a free electron laser (FEL). As spin is conserved in elastic photoemission with linearly polarized radiation, the spin polarization of the elastic valence electrons provide an accurate measure of the magnetization, or more precisely, a measurement of the spin part of the magnetization.

In our experiment a ferromagnetic sample is exposed to a 800 nm pump laser beam. The pump pulse of 100 fs duration excites a 10 nm Fe film serving as the magnetic sample. After a variable time delay the probe pulse from the free electron laser in Hamburg (FLASH) excites photoelectrons from the sample (see figure 6.5). As the FEL probe pulse has a photon energy of 180 eV it excites electrons from the valence band and core electrons. As the high energy electrons scatter with valence electrons on the way to the surface a cascade of lower energy electrons is created. This cascade carries an average spin polarization of the valence band. In order to measure the spin polarization of the photoelectrons a Mott spin polarimeter is used.

In 2011 we had two beam times at FLASH. During our first beamtime at FLASH in March 2011 we successfully demonstrated the feasibility of time and spin resolved photoemission experiments using FEL radiation. This experiment had the goal of confirming the existence of ultrafast demagnetization processes in iron. The FEL induced photoelectrons were collected by an electrostatic lens and transferred into the Mott spin polarimeter. As this experiment did not contain an energy filter the detected electrons were mostly part of the cascade. Figure 6.6 shows the time dependence of the spin polarization after demagnetization by the 800 nm laser pulse. The spin polarization drops

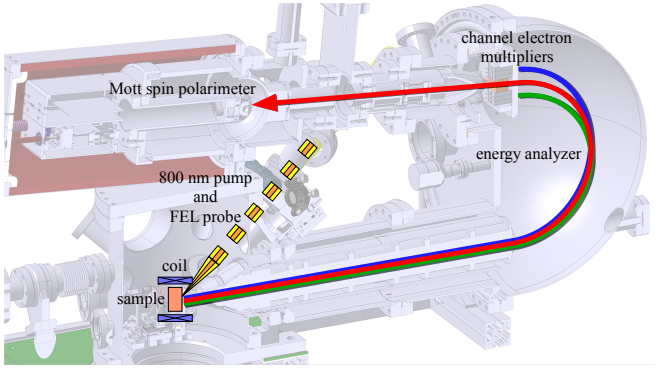

Figure 6.5: Principle of the experiment: The ferromagnetic sample is exposed to the laser pump beam followed by the FEL pulse. The pump- and probe beams are collinear. The FEL pulse photo-excites electrons which are energy analyzed and accelerated into the Mott spin polarimeter. The spin polarization is measured along the magnetization direction of the sample.

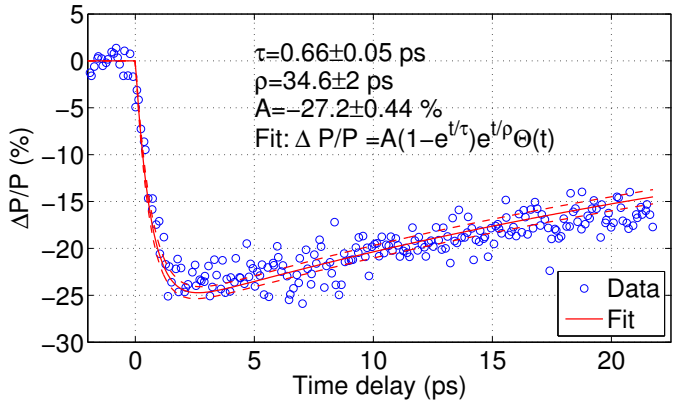

Figure 6.6: Results from our first beamtime at FLASH in March 2011. The spin polarization drops as a function of the pump probe delay time within less than a picosecond. As more data points were taken on the transition, the noise level is smaller around zero delay time than for longer delay times. The time resolution is limited by the timing jitter between the FEL and the 800nm laser, which will be improved.

within less than a picosecond and slowly recovers on the 100ps time scale. This clearly demonstrates the feasibility of time and spin resolved photoemission experiments and shows that the magnetization indeed drops within less than a picosecond after excitation. Here we are not just looking at the spin polarization of electrons close to the Fermi energy, but at the cascade electrons which represent an average of the whole valence band.

For our second beam time in July 2011 we added a hemispherical electron energy analyzer to the experimental setup. This way we can select the energy of the photoelectrons before detection in the Mott spin polarimeter. For future experiments we intend to detect the demagnetization effect for different parts of the valence band. During the second beam time the timing diagnostic system at FLASH was improved so we achieved a higher temporal resolution than during the first beam time. We can see that the spin polarization of the cascade electrons decays within less than 100 fs after excitation by the pump pulse.

Chapter 7

Quantum Device Lab

(http://qudev.ethz.ch/)

Head
Prof. Dr. A. Wallraff

Academic Staff

Dr. A. Abdumalikov	P. Arnold	R. Barmettler
M. Baur	S. Berger	C. Eichler
Dr. A. Fedorov	Dr. S. Filipp	Dr. J. Fink
T. Frey[1]	J. Govenius	C. Gross
E. Ilgünsatiroglu[2]	K. Juliusson	C. Lang
G. Littich[3]	Y. Liu	S. Miesch
J. Mlynek	M. Oppliger	M. Pechal
M. Peterer	G. Puebla-Hellmann	Dr. K. Reim
Y. Salathe	L. Steffen	T. Thiele
A. van Loo		

[1] joint PhD student with Prof. Dr. K. Ensslin, ETH Zürich, Switzerland
[2] joint PhD student with Prof. Dr. A. Imamoglu, ETH Zürich, Switzerland
[3] joint Master student with Prof. Dr. H. Haeffner, UC Berkeley, USA

Technical Staff

H. Aeschbach	J. Lütolf

Administrative Staff

Dr. F. Bay	G. Strahm

7.1 Experimental State Tomography of Itinerant Quantum Microwave Fields

C. Eichler, D. Bozyigit, C. Lang, L. Steffen, M. Baur, J. Fink, S. Filipp, A. Wallraff

Quantum properties of radiation are typically investigated at optical frequencies where single field excitations (photons) can be detected with almost unit efficiency. Due to recent progress in the field of circuit quantum electrodynamics, where microwaves are used to control and read-out the state of superconducting quantum circuits, it has become an interesting task to understand propagating microwave radiation on a quantum level as well. In our recent experiments we have generated different kinds of non-classical microwave radiation fields and characterized their properties in a detection scheme where linear amplifiers and field quadrature detectors are used instead of single photon counters. First, we have built a single microwave photon source and demonstrated photon anti-bunching of the emitted radiation within time-correlation function and state tomography measurements. Second, we have studied two-mode correlations in a squeezed state generated by a parametric amplifier. A careful analysis of the statistical correlations between signal and idler modes demonstrated the entanglement between microwave photons of different frequency.

7.1.1 Reconstruction of single photon Fock states

The general goal of photon state tomography is to reconstruct the density matrix of a radiation field mode described by a bosonic field operator a. One way of collecting all the necessary information for such a reconstruction is to measure the statistical moments $\langle (a^\dagger)^n a^m \rangle$ of the field. We evaluate these moments from measured 2-dimensional probability distributions of the field quadrature components X and P. Even in the presence of significant amplifier noise – which is 80 times larger than the single photon signal in our experiments – we are able to determine the moments with high precision up to order $n + m = 4$.

The resulting moments when a single photon state $|1\rangle$ is prepared are shown in Fig.7.1(a). We observe that all off diagonal moments are close to zero which is a feature of Fock states and thermal states. However, we can distinguish the single photon state from a thermal state by evaluating the fourth order moment $\langle (a^\dagger)^2 a^2 \rangle$ which is close to 0 indicating antibunching of the prepared single photon states. In contrast, a thermal state with the same mean photon number would display a diagonal 4th order moment of approximately 2. We have also prepared and analyzed superposition states of the type $(|0\rangle + e^{i\phi}|1\rangle)/\sqrt{2}$. For this class of states, the mean amplitude ideally equals the mean photon number $|\langle a \rangle| = \langle a^\dagger a \rangle = 0.5$ which we also observe in our experiments. To further confirm the validity of our scheme, we have generated classical coherent states $|\alpha\rangle$ with amplitude $\alpha = 1$ and $\alpha = 0.5$ for which results are also in agreement with the expectations. From the measured moments we have reconstructed the Wigner function $W(\alpha)$ for the single photon Fock state [Fig. 7.1(b)] and its superposition with the vacuum. In both cases we observe negative values of $W(\alpha)$ indicating the quantum character of the observed states.

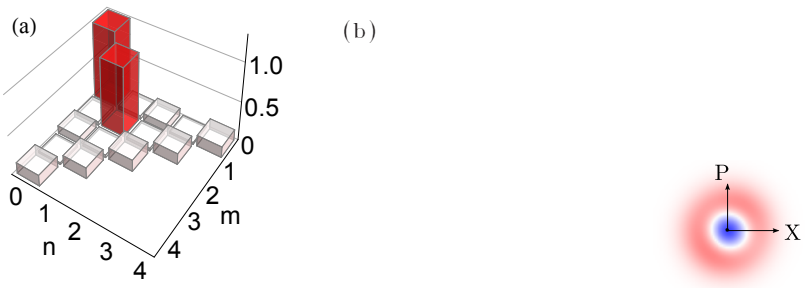

Figure 7.1: (a) Absolute value of the moments $|\langle (a^\dagger)^n a^m \rangle|$ up to 4th order for a single photon Fock state. (b) Wigner function $W(\alpha = X + iP)$ for a single photon Fock state and (f) a superposition state both reconstructed from the measured moments shown in (a) and (b).

7.1.2 Observation of Two-Mode Squeezing in the Microwave Frequency Domain

In a second set of experiments we have analyzed squeezed radiation emitted from a parametric amplifier – a device which is of great technological interest since it can be used as a quantum limited low noise amplifier. Our parametric amplifier is realized as a $\lambda/4$ transmission line resonator terminated by an array of superconducting quantum interference devices (SQUIDs). The SQUIDs provide a tunable, nonlinear inductance which allows for tuning the resonance frequency [Fig.7.2(a)] and to achieve parametric gain by driving the resulting Kerr nonlinearity with a coherent pump tone. The gain can be adjusted to a desired value by tuning the pump frequency and power accordingly [Fig.7.2(c)]. The parametric amplification can be understood as a four-wave mixing process where 2 pump photons are converted into a pair of entangled signal and idler photons at the upper and lower sideband of the pump ($2\omega_p = \omega_s + \omega_i$).

To verify the entanglement between the photons generated within this parametric down-conversion process we have fixed the pump tone at a specific value and have analysed correlations between the photons with positive and negative detuning from the pump tone. To this goal we simultaneously measure both the quadrature components X_1, P_1 of the signal mode a_1 and X_2, P_2 of the idler mode a_2 which both lie within the band of amplification [Fig.7.2(d)]. We store the results in two-dimensional histograms for the six possible pairs of the four quadrature components. For each pair we first acquire a reference histogram with the pump turned OFF [Fig. 7.2(e)] and a second histogram with the pump turned ON. The differences between such histogram pairs [Fig. 7.2 (f)-(i)] show a systematic change in the detected quadrature statistics when the resonator output in modes $a_{1,2}$ changes from the vacuum state to the two-mode squeezed state. For the single mode histograms $\{X_1, P_1\}$, $\{X_2, P_2\}$ we observe a phase independent increase in the quadrature fluctuations, reflected in the higher probability of measuring larger quadrature values [Fig. 7.2(f) and (g)]. Since the increase in fluctuations is circular symmetric it corresponds to a phase-preserving amplification in each of the individual modes a_1 and a_2. However, for the cross-histograms $\{X_1, X_2\}$, $\{P_1, P_2\}$ we find an increase in the fluctuations along one diagonal axes, indicated by the positive valued regions in the histogram differences [Fig. 7.2(h) and (i)], and a decrease in the other direction. Both these observed features are characteristic for a two-mode squeezed state. A detailed analysis of the measured histograms shows that the signal and idler modes at the parametric amplifier output are indeed non-separable and the photons of different frequencies are entangled.

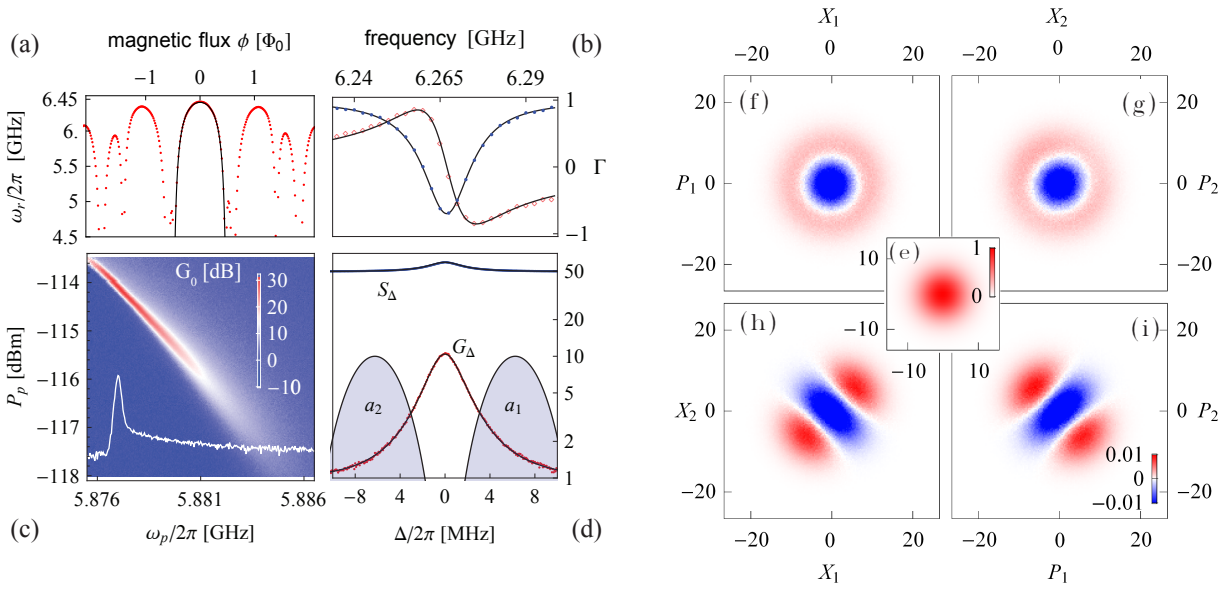

Figure 7.2: (a) Measured (dots) and calculated (solid line) resonance frequency $\omega_r/2\pi$ vs. magnetic flux ϕ. (b) Measured real (blue dots) and imaginary (red diamonds) part of the reflection coefficient Γ in the linear regime for magnetic flux $\phi = 0.23$ and fit to theory (lines). (c) Measured maximum gain G_0 as a function of pump frequency $\omega_p/2\pi$ and pump power P_p. A horizontal cut through the data at $P_p \approx -114\,\mathrm{dBm}$ is shown as a white line. (d) Measured gain G_Δ (red dots) and power spectral density S_Δ (blue dots) for a fixed pump tone as a function of detuning Δ. The 3 dB bandwidth of the gain curve with a maximum gain of 10 dB is $B/2\pi \approx 3.6$ MHz. The filter functions defining modes a_1 and a_2, are shown on a logarithmic scale (arb. units) as the lines enclosing the shaded areas. (e) Quadrature histogram $\{X_1, P_1\}$ when the pump tone is turned OFF given in units of its maximal value. (f)-(i) Difference between quadrature histograms with pump tone turned ON and OFF for 4 different quadrature pairs in the same units as (e).

[1] Experimental State Tomography of Itinerant Single Microwave Photons. C. Eichler, D. Bozyigit, C. Lang, L. Steffen, J. Fink, S. Filipp, and A. Wallraff. Phys. Rev. Lett. 106, 220503 (2011).

[2] Observation of Two-Mode Squeezing in the Microwave Frequency Domain. C. Eichler, D. Bozyigit, C. Lang, M. Baur, L. Steffen, J. M. Fink, S. Filipp, and A. Wallraff. Phys. Rev. Lett. 107, 113601 (2011)

7.2 Second-order correlation function measurements of microwave photons

C. Lang, D. Bozyigit, C. Eichler, L. Steffen, J. M. Fink, A. A. Abdumalikov, M. Baur, R. Bianchetti, P. J. Leek, S. Filipp, M. P. da Silva, A. Blais, and A. Wallraff

At optical frequencies the radiation produced by a source, such as a single-photon emitter, is frequently characterized by analyzing the temporal correlations of emitted photons using single-photon counters. At microwave frequencies, however, there are no efficient single-photon counters yet. Instead, we developed field programmable gate array (FPGA) based electronics to efficiently measure first- and second-order correlation functions of propagating microwave fields using microwave beam splitters, linear amplifiers, and quadrature amplitude detectors. This technique is demonstrated with radiation sources ,which are characterized by different photon number statistics, including pulsed and continuously driven single-photon sources. For both types of single-photon sources we observe photon antibunching in second-order cross-correlation function measurements. We also investigate first-order correlations and observe resonance fluorescence and Rayleigh scattering in Mollow-triplet-like spectra for the continuously driven single-photon source.

Our circuit quantum electrodynamics (QED) setup is composed of two essential ingredients: a photon source and a quadrature amplitude detection system from which we extract the photon statistics. The single-photon sources consist of a single superconducting artificial atom with transition frequency ω_a coupled to a superconducting transmission line resonator with resonance frequency ω_r.

For the continuously driven single-photon source we tune the transition frequency of an artificial atom into resonance with the resonator $\omega_r = \omega_a$. Due to the large coupling between the artificial atom and the resonator, excitations do not belong to one of the subsystems but are shared between the two. This results in a nonlinear energy level spectrum known as the Jaynes-Cummings ladder. We drive the system at the input of the resonator with coherent microwave radiation of the frequency that is resonant to the transition between the ground state $|0g\rangle$ and the antisymmetric superposition of one photon in the resonator but atom in the ground and no photon but excited atom $|1-\rangle$. Due to the strong non-linearity of the energy levels only a single photon can enter the resonator at a time. Additional photons are prevented from entering the resonator, as transitions into higher excited states are not resonant with the drive. Only once the photon has left the cavity can the next photon enter into the resonator, realizing a source of single photons. This process is called *photon blockade*.

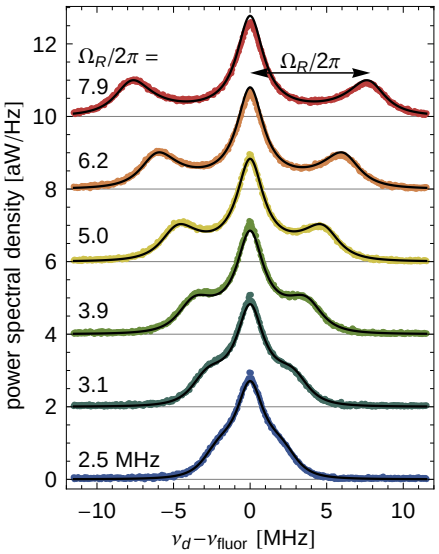

Figure 7.3: Measured resonance fluorescence spectrum *vs.* (indicated) drive amplitude $\Omega_R/2\pi$ (dots) and analytical spectrum (lines).

A nonlinear system, which is only driven by a single frequency ω_d between the ground state and the first excited state, can be modeled as an effective two-level system. It can be shown analytically that the drive dresses each of the two states. The magnitude of the induced splittings grows approximately linear with the drive amplitude Ω_R. We investigate radiation scattered off the system by measuring the power spectral density. Here, we observe not only the coherently Rayleigh-scattered part but also the incoherently scattered resonance fluorescence part of the spectrum. The resonance fluorescence spectrum is characterized by three spectral lines forming a Mollow triplet of a driven effective two-level system, see Figure 7.3. These three spectral lines arise due to spontaneous decay from the dressed excited state $|1-\rangle$ into the dressed ground state $|0g\rangle$ (four decay channels, two of

which are degenerate). The spectrum is in excellent agreement with the analytical two-level model, and we observe the expected linear dependence of the side peak frequency with the drive amplitude Ω_R.

The radiation scattered by the effective two-level system is expected to have single-photon character, which we proof by measuring the second-order cross-correlation between the two output arms of a beamsplitter which is positioned between the source and the heterodyne detection system. The second-order cross-correlation function $g^{(2)}(\tau)$ provides a measure of the probability to detect power at time $t+\tau$ in one arm of the beamsplitter given power detected at time t at the other arm of the beamsplitter. In the case of a single-photon source, the photon is detected only in one output but never in both outputs at once leading to $g^{(2)}(0) = 0$. Figure 7.4(a) shows a measurement of the second-order cross-correlation of the continuous single-photon source. We observe the expected antibunching of the single-photon source at $\tau = 0$. The measurement confirms the expectation to observe an enhanced probability of detecting a second photon at a later time $\tau = \Omega_R/\pi$ when the drive has re-excited the system from the ground state into the excited state where a spontaneous decay can happen emitting a second photon.

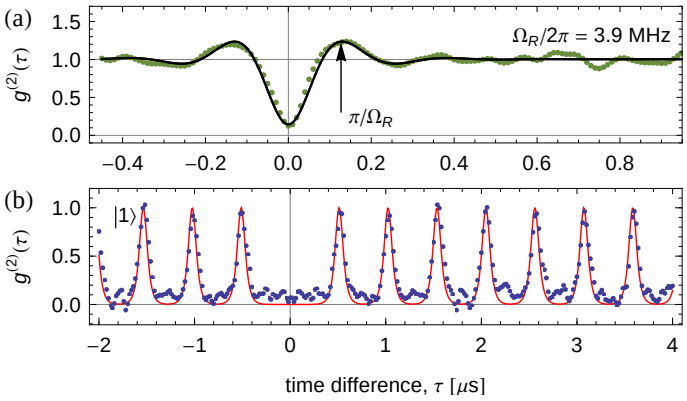

Figure 7.4: Second-order cross-correlation function measurements (dots) for the continuous (a), and pulsed (b) single photon source with theoretically expectation (lines).

In our pulsed single-photon source we deterministically generate a single photon in the resonator every $\delta\tau = 512\,\mathrm{ns}$. After the photon generation the atom is detuned from the resonator, and the photon leaves the resonator after a cavity decay towards the microwave beamsplitter. Figure 7.4(b) shows the measurement of the second-order cross-correlation function for this pulsed singe-photon source. Again, we do not detect photons in both output arms of the beamsplitter simultaneously ($\tau = 0$) proving the single-photon character of the radiation. At the times around $n\,\delta\tau$ we see the correlations between subsequent single photons that leave the beamsplitter at random outputs. These correlations are the same at all time differences $n\,\delta\tau$ for all integer numbers $n \neq 0$. The peak at τ around 0 is absent as a single photon can only be detected in a single output of the beamsplitter but never in both outputs simultaneously.

[1] C. Lang, D. Bozyigit, C. Eichler, L. Steffen, J. M. Fink, A. A. Abdumalikov, M. Baur, S. Filipp, M. P. da Silva, A. Blais, A. Wallraff, Phys. Rev. Lett. **106**, 243601 (2011)

[2] D. Bozyigit, C. Lang, L. Steffen, J. M. Fink, C. Eichler, M. Baur, R. Bianchetti, P. J. Leek, S. Filipp, M. P. da Silva, A. Blais, A. Wallraff, Nat. Phys. **7**, 154 (2011)

[3] D. Bozyigit, C. Lang, L. Steffen, J. M. Fink, C. Eichler, M. Baur, R. Bianchetti, P. J. Leek, S. Filipp, A. Wallraff, M. P. da Silva, A. Blais, J. Phys.: Conf. Ser. **264**, 012024 (2011)

7.3 Preparation of qubit dark states using individual addressing

S. Filipp, M. Baur, R. Bianchetti, J. M. Fink, M. Göppl, A. F. van Loo, L. Steffen, and A. Wallraff

In the circuit quantum electrodynamics architecture (QED) a coplanar microwave resonator can be used to transmit information between distant superconducting qubits using the resonator as a common 'quantum bus'. The interaction can be mediated by exchange of real photons, when the qubits are resonant with the cavity, i.e. if adding a single quantum of energy to either the qubits or the resonator costs an equal amount of energy. Alternatively, qubits can couple by exchange of virtual photons, short-lived excitations of the vacuum. Virtual photons lead to a transverse interaction between qubits, when they are non-resonant with the cavity but resonant with each other. In this parameter regime a single excitation cannot be localized within the coupled qubit-qubit system resulting in maximally entangled energy eigenstates (Figure 7.5(a)).

7.3.1 Virtual photon mediated qubit-qubit coupling

We have measured the magnitude of the virtual photon mediated qubit-qubit coupling J by sweeping the transition frequency of one qubit across resonance with a second qubit. The value of J determines the size of the splitting shown in Figure 7.5(b). In our experiments [1] we have spectroscopically measured the magnitude of the inter-qubit coupling J at different frequencies of the qubits and extracted the enhanced coupling in dependence of their detuning from the resonator frequency ω_0 (Figure 7.5(c)). We have also shown that higher-harmonic resonator modes have to be taken into account to explain the value of J around the fundamental resonator mode.

In addition to the clearly resolved avoided crossing, the two-photon transition to the doubly excited qubit state becomes allowed when the qubits are resonant with each other. In this situation also a dark state forms, revealed by the vanishing upper branch of the spectrum in Figure 7.5(b). Both of these features follow from the symmetry properties of the system with respect to the driving microwave field.

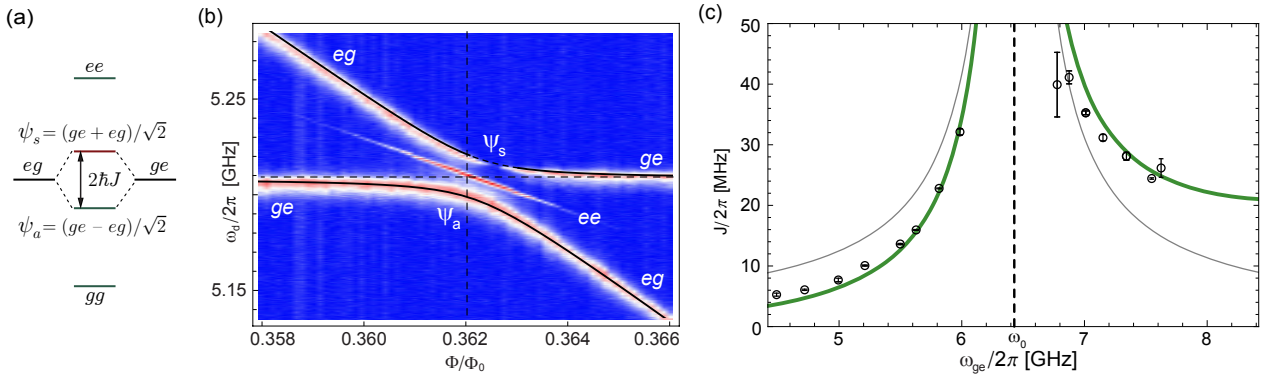

Figure 7.5: (a) Energy level diagram of two transmon qubits coupled via a microwave resonator. At resonance the maximally entangled states ψ_a and ψ_s are formed. (b) Spectroscopic measurement of an avoided level crossing as function of flux threading the first qubit loop with the second qubit at a fixed frequency. (c) Experimentally extracted value of the coupling strength J as a function of qubit frequency ω_{ge} (dots) in the vicinity of the fundamental resonator mode ω_0. The gray thin line indicates calculated values of J for frequency-independent qubit-resonator coupling strength considering a single mode. The asymmetry of J is theoretically reproduced, if four resonator modes are taken into account (green thick line).

7.3.2 Subradiance of the dark state prepared by local phase controlled microwave signals

When two coupled qubits are driven through the common resonator close to its *fundamental* mode only the anti-symmetric state can be excited, while the symmetric eigenstates remains dark as shown in Figure 7.5(b). Similarly, in the vicinity of the *first harmonic* mode only the symmetric state can be excited: From the perspective of the microwave field, the qubits positioned at the ends of the resonator, where the microwave field in the cavity is equal both in sign and amplitude, cannot be distinguished and a photon excitation must be shared symmetrically between the qubits. By individual addressing, the qubits can, however, be discriminated and the transition to the anti-symmetric state of the coupled two-qubit state can be enabled by properly choosing the local phase of the microwave drive [2]. This scheme is depicted in Figure 7.6(a); a micrograph of the setup is shown in Figure 7.6(b). Equivalently, since the resonator supports only microwave photons, which do not allow the distinction between individual qubits, only the decay of the symmetric state by photon emission into the resonator is allowed, whereas the decay of the dark, anti-symmetric state is forbidden. Using the local phase control technique we have prepared the qubits in this dark state and observed its enhanced lifetime as compared to the symmetric bright state (Figure 7.6(c)), a characteristic feature of subradiance. The dark state lifetime is limited mainly by the single qubit lifetimes $1/\gamma_i$ into other, non-resonator decay channels, but not by the resonator induced Purcell decay γ_κ. In the future, multi-qubit extensions of this control technique can be used to prepare and study highly correlated quantum states of cavity-coupled qubits.

[1] Multimode mediated qubit-qubit coupling and dark-state symmetries in circuit quantum electrodynamics. S. Filipp, M. Göppl, J. M. Fink, M. Baur, R. Bianchetti, L. Steffen, and A. Wallraff. Phys. Rev. A 83, 063827

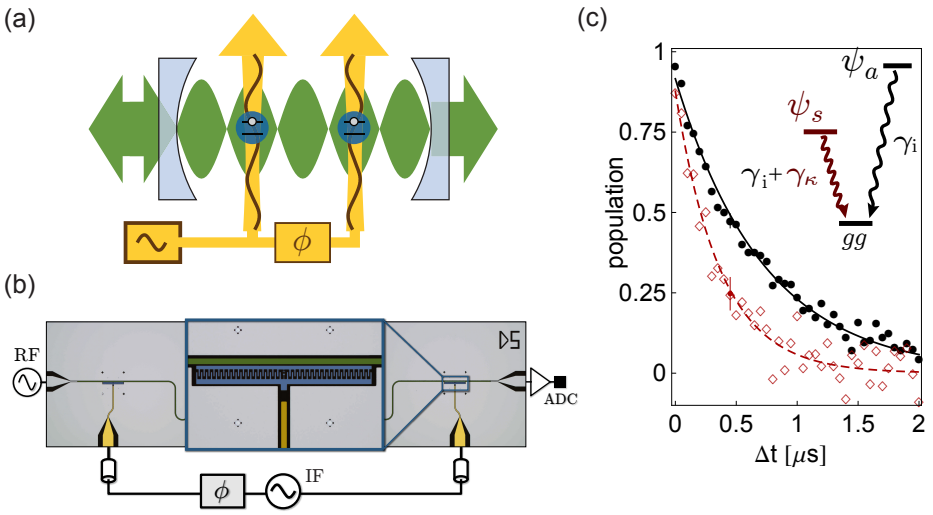

Figure 7.6: (a) Local phase control of a two-qubit system in a cavity. (b) Optical micrograph of the setup comprising two transmon qubits (blue), local control lines (yellow) and the transmission line resonator acting as a microwave cavity (blue). (c) Population of the bright, symmetric state ψ_s (red diamonds) and the dark, anti-symmetric state ψ_a (black dots) as a function of time.

(2011).

[2] Preparation of subradiant states using local qubit control in circuit QED. S. Filipp, A. F. van Loo, M. Baur, L. Steffen, and A. Wallraff. Phys. Rev. A 84, 061805 (2011)

Chapter 8

Semiconductor Quantum Materials

(http://www.mbe.ethz.ch/)

Head
Prof. Dr. W. Wegscheider

Academic Staff

Ch. Charpentier	Dr. St. Fält	Dr. T. Feil
A. Maier	S. Peters	Ch. Reichl
S. Riedi	Dr. W. Stumpf	W. Wüster

Technical Staff

J. Gmür	S. Heider	M. Sturzenegger

Academic Guests
Prof. W. Dietsche (26.09.2011 - 18.11.2011)

Administrative Staff

C. Egli	C. Vinzens

8.1 Raman Spectroscopy in the Quantum Hall Regime

T. Feil, C. Reichl, W. Wegscheider

High-mobility two-dimensional electron gases at low temperatures and high magnetic fields can condense in a host of incompressible fluid states. A study of the excitations of these states directly addresses the magnitude of the involved interactions. We use the resonant Raman scattering technique to probe these excitations. Thereby a laser is scanned across a luminescence channel of the system. When the laser is close to resonant with that channel, light scattered inelastically from collective excitations of the corresponding ground state appears as an additional peak in the vicinity of the laser line. The frequency difference between laser and the additional peaks directly reflects the excitation energies. Fig. 8.1 shows such a resonant Raman scan. White lines in the plot correspond to luminescence channels while the gray line is a Raman signal at fixed distance from the laser line. In this particular case, the peak is associated with the roton minium of the excitation spectrum (cf. inset Fig. 8.1); i.e. a point on the excitation dispersion with large density of states.

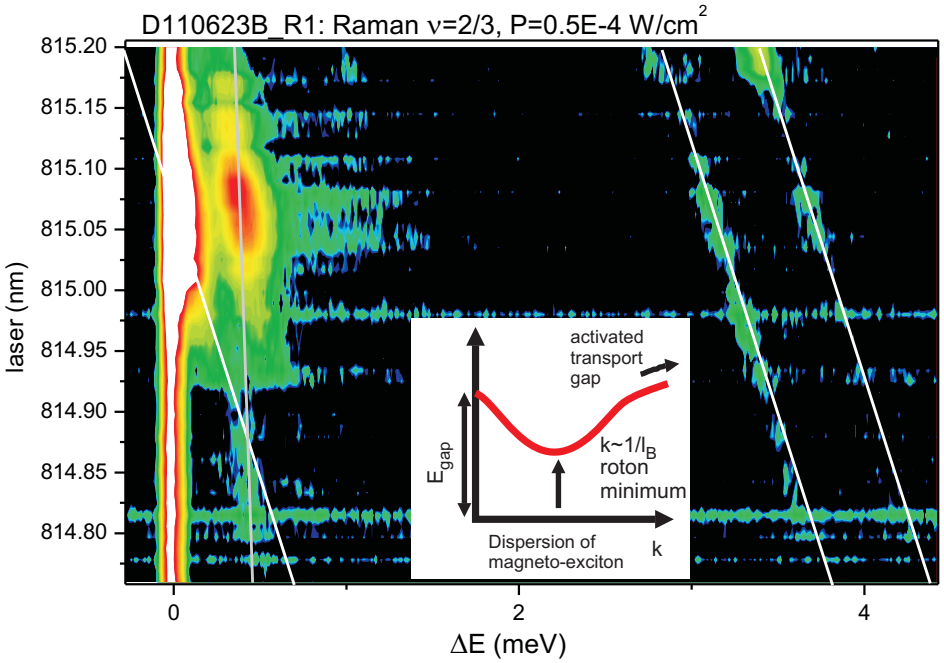

Figure 8.1: Magneto-Raman spectra taken at $\nu = 2/3$ using different laser excitation wavelengths.

8.2 Ballistic Hole Transport in Quantum Wires

S. Riedi, C. Reichl, S. Fält, W. Wegscheider

In 1990 L. Pfeiffer and co-workers presented first results of a new method in molecular-beam epitaxy (MBE). They cleaved an MBE grown [100] GaAs wafer in situ and continued growth on the freshly exposed [110] edge. Accordingly, this procedure is called cleaved-edge-overgrowth (CEO). In 1994 they reported the first measurements of electron transport in a ballistic quantum wire (QWR) fabricated by CEO MBE. This was the starting point for a series of ever more sophisticated experiments investigating the electronic and optical properties of such wires. Nevertheless, it was not before 2005, when L. Pfeiffer et al. reported first ballistic hole conduction in such wires. Although

analogous experiments as for electron conduction are thinkable, holes show a different behavior in terms of effective mass, g-factor and spin-orbit interaction with the lattice. It was with one of these hole QWRs, when in 2010 the first observation of a predicted spin-orbit gap in a 1D sample, where counter-propagating spins build up a spin current, was published. Understanding the flow of spins is the basis for future spin-based electronic applications (spintronics). Using the spin degree of freedom, the design of faster building blocks, which produce less heat, compared to conventional electronics based on the control of the charge flow, will be possible.

Last year, the following efforts have been made in our group to produce even cleaner ballistic hole GaAs QWRs made by CEO MBE (see Fig. 8.2) to extend the investigations conducted by L. Pfeiffer et al.. In a fist step a GaAs/AlGaAs multilayer structure is grown onto a [100] GaAs substrate, including a carbon-modulation-doped quantum well structure which results in a 2D hole gas (2DHG). After removing it from the MBE system, the wafer is chemically thinned from the back to less then 100 μm and cleaved into square pieces. QWR defining Ta top-gates are then sputtered on the samples in a photolithographic lift-off process. Prior to a second growth step, a mechanical arm inside the MBE sweeps across the samples and cleaves them at a pre-established scratch mark, which has been inscribed earlier outside the MBE using a scribing machine. This exposes a fresh [110] crystalline surface, which is immediately overgrown by a second p-doped multilayer sequence. Finally, the metal gates and the 2DHGs between the gates are contacted with In solder and In-Zn respectively.

By applying a sufficient positive bias on the different gates, it should be possible to fully deplete the 2DHG directly below them, which divides the 2DHG into isolated regions which are only connected via the QWR defined by the cleave and the 2DHG of the second growth step. When a positive voltage in excess of that needed for local 2D depletion under the gates is adjusted, the hole density in the QWR can be controlled.

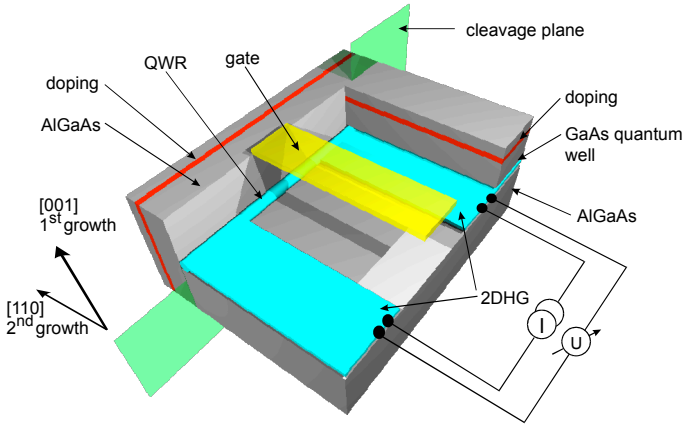

Figure 8.2: Schematic view of the CEO QWR measurement setup.

8.3 InAs/(Ga,Al)Sb Heterostructures - Prospects for a 2D Topological Insulator

C. Charpentier, W. Wegscheider

Topological insulators - characterized by a gapped bulk and counterpropagating edge modes in the presence of time reversal symmetry - have been in the focus of interest since their theoretical prediction and subsequent experimental realizations in 3D (Bi_2Se_3, Sb_2Te_3 etc.) and 2D (HgTe/CdTe) and inspired a number of future applications, including spintronics, quantum computing and in combination with a superconductor: the generation of Majorana fermions.

Two-dimensional topological insulators can be realized in semiconductor systems that present bands inverted with respect to their usual arrangement by a strong spin-orbit coupling (HgTe) or by hybridization of neighboring electron and hole systems (combined InAs/GaSb quantum wells (CQWs) between AlSb barriers) according to theoretical calculations. So far, only the HgTe/CdTe system has been realized and studied. The InAs/GaSb CQW with its unique

type II band alignment allows to tune the band gap of the hybridized electron-hole gas by electric fields and would allow to use the well-established III-V semiconductor technology.

End of 2010 and beginning of 2011, we have set up a molecular beam epitaxy (MBE) system for the growth of Sb and As based III-V semiconductors and could start the fabrication of InAs/AlSb QWs in August 2011. A first achievement are the routinely attained very high mobilties in InAs/AlSb QWs ($\mu = 550.000$ cm^2/Vs with $n = 7.8 \cdot 10^{11}$ cm^{-2}), second only to a $\mu = 10^6$ cm^2/Vs sample reported by the Kroemer group (University of California at Santa Barbara). In December 2011, we have started the fabrication of AlSb/InAs/GaSb CQWs that are being characterized by electronic transport measurements in magnetic fields up to 16T at 300mK. Experimental feedback will help to optimize the growth routines and layer sequences.

Preliminary results reveal that conventional lithographic techniques can be successfully adapted to pattern these heterostructures for the fabrication of micron-sized devices, which can be investigated by means of transport experiments. In collaboration with the Nanophysics group of Prof. Ensslin, we are developing procedures to fabricate structures on micro- and nanometer scales to further investigate the InAs/GaSb CQWs.

8.4 Gate-induced Two-dimensional Electron Systems in Undoped GaAs/AlGaAs Heterostructures

S. Peters, C. Reichl, W. Wegscheider

High sample quality is crucial for fundamental studies of electron-electron interactions. For instance, fractional quantum Hall effect (FQHE) states are sensitive to disorder such that the surpassing of a certain threshold value in mobility seems to be a prerequisite for well pronounced FQHE states. Whereas modulation-doping techniques based on remote ionized impurities reduces the impact of the dopant-induced disorder on the electron system, one can completely get rid of it by inducing a 2DES by means of a top gate. A further advantage of the gate-induced 2DES is the possibility for adjusting the electron density.

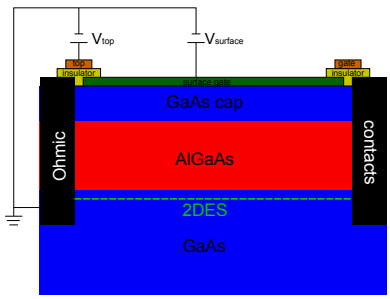

Figure 8.3: Schematic of an undoped heterostructure field-effect device including the lateral ohmic contacts to the 2DES induced at the GaAs/AlGaAs interface.

The principle of fabricating two-dimensional electron gases in undoped GaAs/AlGaAs heterostructures is illustrated in Fig. 8.3. Positive gate voltages serve to draw electrons into the GaAs/AlGaAs interface forming a 2DES. The carrier density can be adjusted by varying the applied voltages. Crucial for operation is to ensure the vertical diffusion of the lateral contacts to the GaAs/AlGaAs interface layer where the electrons will reside. In order to improve the contacting we chose a two-level gating technique, which is included in Fig. 8.3. Since biases can be applied separately to the top gate and the surface gate the carrier densities in the contact region and in the device region can be controlled independently. Thus contacting can be accomplished by inducing a high density in the contact region. In 2011 we

designed a lithography mask and prepared first samples in FIRST lab. Photolithography is used to define both the contact areas at the sample edges and the two gates. It turned out that the etching below the GaAs/AlGaAs, which is carried out before the contact material is evaporated, is critical as the AlGaAs layer is exposed to air and oxidation is evoked. After improving the preparation process we hope to obtain samples showing a variety of FQHE states. These states, in particular the $5/2$ state, could be investigated regarding the dependance of the adjustable electron density, in order to gain further insight into the underlying electron correlations.

8.5 Spin Hall Effect in GaAs/AlGaAs 2DHSs

A. Maier, C. Reichl, W. Wegscheider

The spin Hall effect (SHE) has attracted considerable interest in theoretical solid state physics over the last few years. In analogy to the anomalous Hall effect the SHE is a spin current perpendicular to the applied electric field, but it is realized in nonmagnetic systems. One differentiates between extrinsic SHE, which results from spin-dependent scattering off impurities, and intrinsic SHE, which is generated by spin-orbit coupling within the band structure of the material system. Here one can further distinguish between the Rashba coupling, which arises from structure inversion asymmetry, e.g. an asymmetric potential of the quantum well, and the Dresselhaus coupling caused by bulk inversion asymmetry, e.g. the lacking of an inversion center in zinc-blende structures. In order to gain information on the degree of spin accumulation at the edges of such a sample a lateral pn-junction was grown. This was accomplished by the cleaved edge overgrowth technique (see Fig. 8.4), where a sample is cleaved and overgrown in situ with an n-doped layer perpendicular to the first growing direction, thus forming a light emitting diode (LED) at the interface. In the following photolithographic procedure, the 2DHS was etched away except for some channels which guide an applied electric current parallel to the pn-junction. The forward biased pn-junction emits light in the near IR (see Fig. 8.4), which should be circularly polarized due to the spin accumulation.

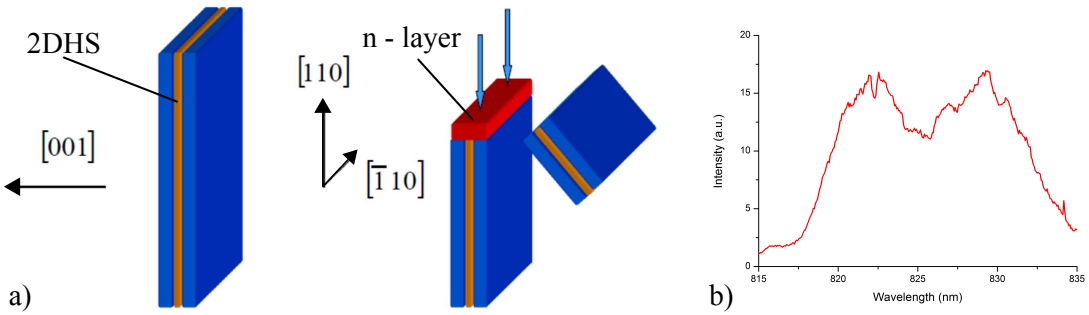

Figure 8.4: (a) The CEO technique: First the 2DHS is grown in the [001] direction (left hand side). Then the sample is cleaved in the MBE-machine and overgrown with a n-doped layer in the [110] direction (right hand side). The interface forms the lateral pn-junction. (b) Emission spectrum from the lateral pn-junction.

8.6 Molecular Beam Epitaxy of Ultrapure Semiconductor Heterostructures

Ch. Reichl, S. Fält, W. Wegscheider

With the high-mobility MBE system transferred from the University of Regensburg, growth operations started in November 2010, after extensive maintenance procedures were performed. The research focus lied and lies on the design and production of ultrapure two-dimensional electron gases (2DEGs) in the AlGaAs/GaAs material system, supporting the extremely fragile 5/2 fractional quantum hall state. This electron state is believed to be crucial for the aspired realization of topological quantum computing. A focus was the investigation of different doping schemes to

minimize potential disorder, thus improving electron mobility as well as development of a stable 5/2 state in the 2DEG-samples. Sample quality rose steadily, yielding an electron mobility of 22.3 $\cdot 10^6$ cm^2/Vs so far. Magneto-transport measurements at very low temperatures (below 20 mK) also showed a continuous development towards pronounced 5/2 states. Recent measurements displayed the even more fragile 7/2 state, which emphasizes the extremely high quality of the produced semiconductor material. Future research foci will be set on the purification of raw materials for epitactical growth and in the intensification of measurements temperatures around 300 mK (which are reached relatively easy, compared to 20 mK) to establish a relationship between the occurance of 5/2 and other less fragile fractional Quantum Hall states.

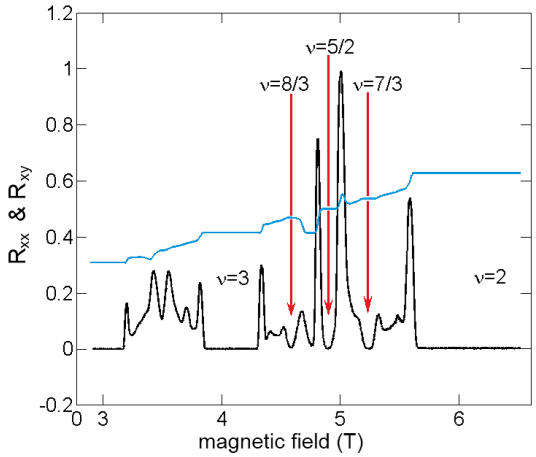

Figure 8.5: Longitudinal and Hall resistance of a ultra-high mobility 2DEG sample showing clearly a well developed ν = 5/2 state.

8.7 Low-Dimensional In(Ga)As Heterostructures for Quantum Dot Applications

W. Stumpf, Ch. Reichl, Ch. Charpentier, S. Fält, W. Wegscheider

Our research also aims at the high quality growth of low-dimensional quantum materials based on indium compounds using our ultra-clean MBE environment, i.e. InAs quantum dots (QDs) and two-dimensional InAs quantum wells. As elaborated in the preceding text, GaAs 2DEGs allow ultra-high mobilities, but moreover can be used to investigate zero-dimensional physics using gate-defined QDs. Optically active QDs can also be realized by self-assembly of InAs (SAQDs) embedded in a matrix of GaAs. These SAQDs can be grown in close proximity to the GaAs 2DEG to create a hybrid system. The high purity of the growth materials will also permit to narrow the exciton linewidth of InAs QDs in order to enable probing of physical processes in SAQDs and the nearby gate-defined QDs of the 2DEG by means of resonant lasers. This makes this hybrid structure a prime candidate to transfer the well controlled electron spin state from a gate-defined QD of the 2DEG by coherent coupling to SAQD in order to define an optical interface to control single photon polarization as it would be very useful in quantum communication and computation. The ultra-clean growth environment also allows a 2DEG to be formed in an InAs channel. While this structure would not enable as high mobilities as a GaAs-based 2DEG due to intrinsic strain, there is still interesting physics to be learned from these devices. We also intend to use this type of structure as a tool for growth optimization and to determine limits of the indium source material.

8.8 Optical Properties of High Mobility Two-dimensional Electron Systems

W. Wüster, F. Haupt, S. Smolka, W. Wegscheider

In the integer quantum Hall effect the corresponding energy gap is given by the single particle cyclotron energy whereas in the fractional quantum Hall effect it is governed by the specific electron-electron interactions of the many particle state. The robustness of quantum Hall states is inherently given by the protection of the energy gap, independent of sample geometries or local perturbations (dirt, impurities, etc.). Quantum Hall states are topologically protected leading to the amazing degree of quantization of conductance in electronic transport measurements.

Our goal is to better understand the properties of the strongly correlated fractional quantum Hall states and the interactions that govern those many-particle states. One way to access this information contained in the electronic system is to exploit the properties of the semiconductor material (GaAs) containing our two dimensional electron system: it has a band-gap that allows for optical inter-band excitations. The optical creation of an electron-hole pair allows us to communicate with the two dimensional electron system through its interaction with the exciton. In the simplest single particle picture we may think of one electron of the two dimensional electron system that recombines with the photo-excited hole. The energy of the emitted light (photoluminescence energy) now strongly depends on the initial electronic state of our electron in the two dimensional system.

We succeeded to perform simultaneous optical photoluminescence and electronic transport measurements of a two dimensional electron system residing in a 20 nanometer wide GaAs quantum well. The sample was mounted in a dilution refrigerator at a base temperature of 100 mK. Optical access was provided via an optical fiber. Figure 8.6 depicts a photoluminescence (PL) measurement as a function of the magnetic field and reveals a considerable deviation of the PL energy from the linear single particle Landau level dispersion. The overall PL energy lies systematically below the single particle energy. This deviation can be explained in terms of the photo-excited hole: in the limit of very high magnetic fields the trion (a complex of two electrons bound to a hole) will be the ground state. We also observed strong correlations between the filling factor (extracted from the overlaid transport curve) and features in the PL energy and oscillator strength. These results show that many body interactions play an important role which we will further investigate by optical means.

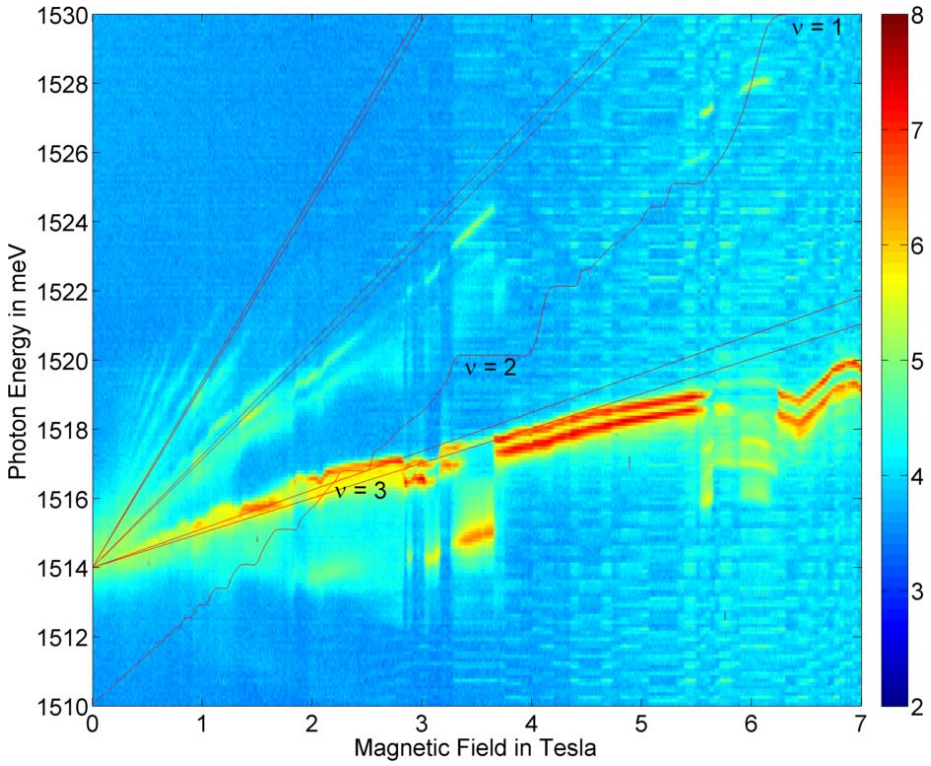

Figure 8.6: Photo luminescence spectrum of a high mobility two dimensional electron system (logarithmic color scale). The two strongest transitions are due to recombination of electrons in the lowest Landau level of the conduction band with heavy holes in the lowest Landau level of the valence band. The simple single particle model suggests a linear dispersion (red lines) which is strongly modified by the many body nature of the problem. Variations in the energy and intensity of the transitions can be correlated with the filling factor (red overlaid transport curve).

Chapter 9

Neutron scattering and magnetism

(http://www.neutron.ethz.ch/)

Head
Prof. Dr. A. Zheludev

Academic Staff
Dr. S. Gvasaliya
Dr. S. Muehlbauer
Dr. W. Lorenz
E. Wulf
Dr. D. Huevonen
S. Chillal
D. Schmidiger
Dr. M. Mansson
M. Thede
M. Goldmann

Academic Guests
K. Povarov (Kapitza Institute, Moscow, Russia), Oct-Dec 2011
E. Popova (Ioffe Institute, St. Petersburg, Russia), Oct-Nov 2012
Prof. S. Lushnikov (Ioffe Institute, St. Petersburg, Russia), Oct. 2011
Dr. J. Wang (Renmin University, Beijing, China), March-May 2011

Administrative Staff
B. Abt

9.1 Phase transitions and excitations in quantum magnets

Nowadays, the central role of quantum magnetic materials is to serve as well-characterized tunable prototypes for the study of some very general and fundamental phenomena in the realm of quantum many-body physics. In this context, we have furthered our experimental studies of quasiparticle confinement and quantum phase transitions in a novel spin-ladder compound DIMPY, complex field-induced incommensurate phases of $Ba_2CuGe_2O_7$, and finite-temperature effects in the quasi-2D spin liquid PHCC. In all cases, the primary focus was on neutron scattering, as it is the only technique that provides direct access to the correlation functions of interest.

9.1.1 Two magnon bound state in a strong-leg spin ladder

D. Schmidiger

The quantum $S = 1/2$ antiferromagnetic spin ladder is one of the most important models in quantum magnetism. In the last few years, the limiting case of a strong-rung ladder was extensively studied both experimentally and theoretically (IPA-$CuCl_3$ [1], Hpip [2]). Its physics can be understood in terms of weakly coupled dimers on the rung and hardly dispersive dimer triplet excitations. In contrast to this dimerized limit, the strong-leg spin ladder is better described as a pair of weakly coupled chains. It features a Haldane gap and the dispersive magnon excitation can be described in terms of confined spinons. The first organometallic realization of such a strong-leg Heisenberg spin ladder is the compound Bis-(2,3-dimethylpyridinium) Tetrabromocuprate (Dimpy, $J_{\mathrm{leg}} = 1.42$ meV and $J_{\mathrm{rung}} = 0.82$ meV [3]). We've studied the two-magnon excitation spectrum with two different inelastic neutron scattering methods in order to demonstrate one particular difference between the two coupling limits:

In the strong-rung case, the two-magnon excitation spectrum features a weak continuum and corresponds to the simultaneous excitation of two individual and non-interacting dimer-triplets. In the strong-leg case, the situation is completely different. Figure 9.1b presents the DMRG calculation of the two-magnon excitation spectrum. Most of the spectral weight is contained in a two-magnon bound state below the continuum persisting throughout more than 60 % of the Brillouin zone while the two-magnon continuum itself is orders of magnitude weaker. Therefore, magnon quasiparticles are not propagating freely but feel a strong short-ranged attractive potential in which bound states occur.

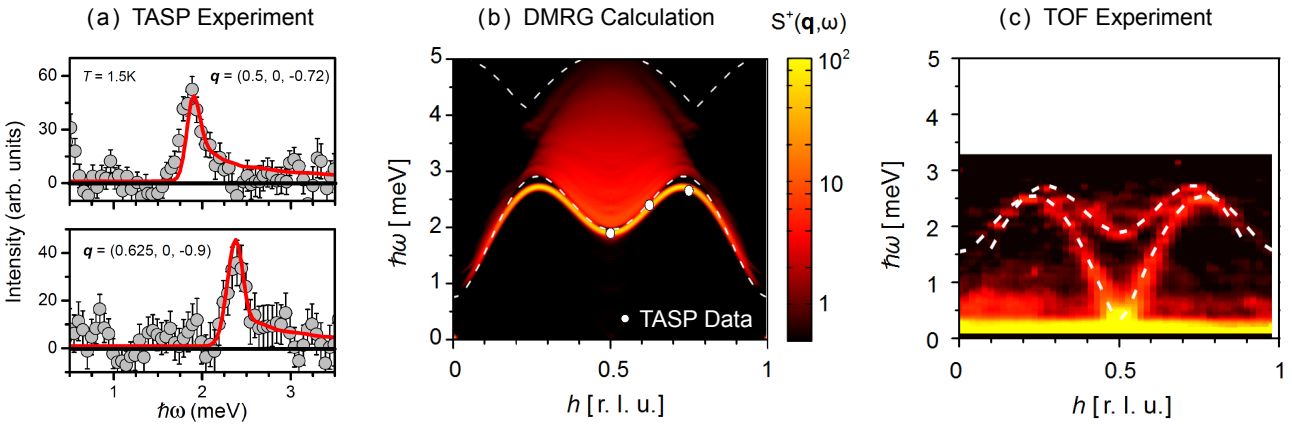

Figure 9.1: (a) Triple-axis INS experiments showing the two-magnon excitation. (b) DMRG calculation performed by P. Bouillot: Two-magnon continuum and bound state. (Circles: Data as in (a)). (c) Time-of-flight data from the CNCS instrument demonstrating one- and two-magnon excitations. (Broken lines: DMRG)

Inelastic neutron scattering measurements were performed at the TASP spectrometer (PSI, fig. 9.1a), with 4 co-aligned and fully deuterated Dimpy single crystals [4]. In constant-q scans, the two-magnon bound state is clearly visible as a peak. The red full line indicates the numerical calculation (fig. 9.1b) convoluted with instrumental resolution. The measured peak positions are shown as white circles in fig. 1b. In addition, time-of-flight experiments were performed

at the CNCS spectrometer at Oak Ridge (fig. 9.1c). In these experiments, both the one- and two-magnon excitations could be observed throughout most of the Brillouin zone.

[1] T. Masuda *et al.*, Phys. Rev. Lett. **96**, 047210 (2006)
[2] P. Bouillot *et al.*, Phys. Rev. B **83**, 054407 (2011)
[3] D. Schmidiger *et al.*, Phys. Rev. B **84**, 144421 (2011)
[4] D. Schmidiger *et al.*, Phys. Rev. Lett.- in press (2012); arXiv:1112.4307v1.

9.1.2 Small Angle Neutron Scattering on the Dzyaloshinskii-Moriya Helimagnet $Ba_2CuGe_2O_7$

S. Mühlbauer

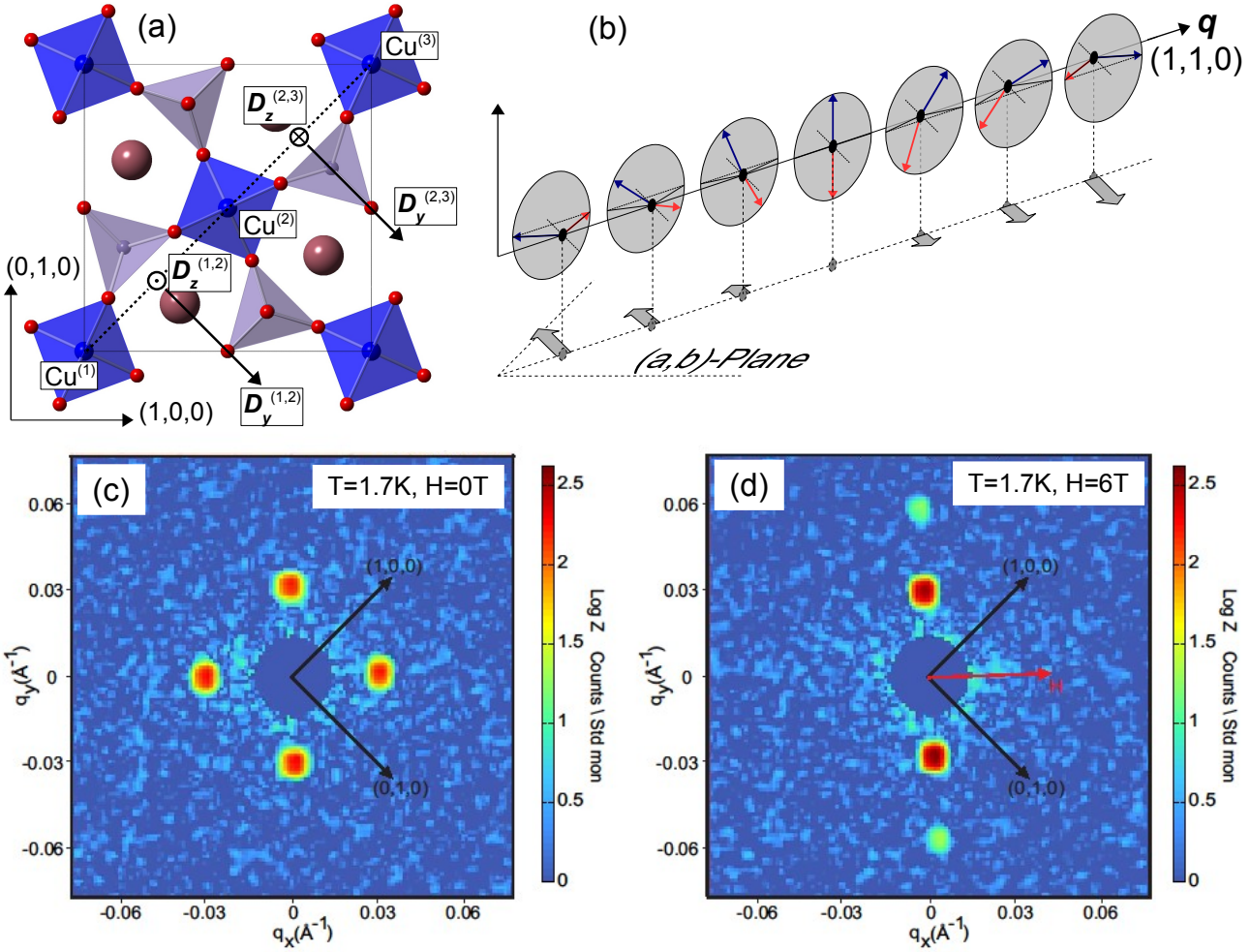

Figure 9.2: (a) Crystallographic structure of $Ba_2CuGe_2O_7$ viewed along the c-axis. (b) Zero field distortion of the almost AF cycloidal structure, leading to an alternating uniform magnetization. Shown is a projection of AF spins along the (-1,1,0) direction. (c) Typical SANS data taken at $T = 1.7$ K, $H = 0$ T (c) and $T = 1.7$ K, $H = 6$ T (d).

Motivated by the discovery of topologically stable skyrmion phases in MnSi [1] and by the potential multiferroicity, helical spin-structures have gained lots of interest. Besides exchange frustration, magnetic spirals can be promoted by the Dzyaloshinsky-Moriya interaction (DM) [2] for antisymmetric exchange paths. Such is the non-centrosymmetric tetragonal antiferromagnet (AF) $Ba_2CuGe_2O_7$ which shows an incommensurate, almost AF cycloidal spin structure [3]. The existence of stable skyrmion phases was predicted for $Ba_2CuGe_2O_7$ [4], however, such structures have not been observed so far. In contrast, a complex, highly orientation dependent phase diagram [5] was found.

The basic feature of $Ba_2CuGe_2O_7$ is a square arrangement of Cu^{2+} ions in the (a, b)-plane (a depiction of the unit

cell is given in Fig. 9.2 (a)). Nearest-neighbor in-plane AF exchange along the diagonal of the (a, b)-plane is the dominant magnetic interaction. The interaction between Cu-atoms from adjacent planes is weak and ferromagnetic (FM). The DM vector consists of two components: For Cu-bonds along (1,1,0), $\mathbf{D_y}$ points along the diagonal of the (a, b)-plane in the (1,-1,0) direction. $\mathbf{D_z}$ is parallel to the tetragonal c-axis and sign-alternating for neighboring bonds. It has been established by neutron diffraction [3] that the almost AF cycloid, observed below $T_N = 3.2\,\mathrm{K}$ is stabilized by $\mathbf{D_y}$. The influence of $\mathbf{D_z}$ has been neglected in all quantitative descriptions of $Ba_2CuGe_2O_7$ so far. By simple geometric considerations, a sign alternating FM canting of spins has been predicted by theory [4], in the presence of $\mathbf{D_z}$. The FM moment is aligned in the (a, b)-plane. A schematic depiction is given in panel (b). However, up to now, no experimental evidence of the effects of $\mathbf{D_z}$ could be given.

We have used small angle neutron scattering (SANS) to investigate potential FM correlations of $Ba_2CuGe_2O_7$. Fig. 9.2 (c) and (d) depict typical SANS data obtained at $T = 1.7$ K. Magnetic satellite reflections at ($\pm\xi$,$\pm\xi$,0), $\xi \sim 0.0273$ are observed at zero field (c), clearly indicating a FM distortion of the cycloid. For magnetic field applied in the basal (a, b)-plane, a single domain state is realized (d). For increasing field, weak higher harmonics with increasing weight are observed at even multiples of the propagation vector at 2ξ. The existence of even higher harmonics is readily explained by an asymmetric distortion of the cycloidal structure, caused by the magnetic field, which compresses next-nearest periods of the cycloid. In conclusion, our SANS study gives first direct experimental evidence for the effect of the staggered DM vector $\mathbf{D_z}$, clearly pointing out the need for further theoretical effort to understand the magnetic phase diagram.

[1] S. Mühlbauer *et al.*, Science **323**, 5916 (2009).
[2] I. E. Dzyaloshinskii, J. Phys. Chem Solids 4, **241** (1958). T. Moriya, Phys. Rev. **120**, 91 (1960).
[3] A. Zheludev, *et al.*, Phys. Rev. B **56**, 14006 (1997) and references therin.
[4] A. N. Bogdanov, *et al.*, Phys. Rev. B **66**, 214410 (2002). A. N. Bogdanov, *et al.*, J. Magn. Mater. **272**, 332 (2004).
[5] S. Mühlbauer, *et al.*, Phys. Rev. B **84**, 180406 (2011).

9.1.3 Magnon lifetimes in a 2-dimensional spin liquid

M. Goldmann

The low-temperature dynamics of quasi one-dimensional (1D) quantum spin liquids is rather unique due to peculiarities of 1D topology. On the experimental side, the lack of instrumental resolution and sensitivity was overcome only recently [1,2] to validate certain universal scaling laws predicted by theory. The new frontier is higher dimensions, where universality arguments can not be made, and the problem is considerably more complex from the theoretical standpoint. To provide experimental support, we employed state of the art neutron spectroscopy technique to study finite-temperature effects on exciatations in a prototypical quasi-2D spin liquid.

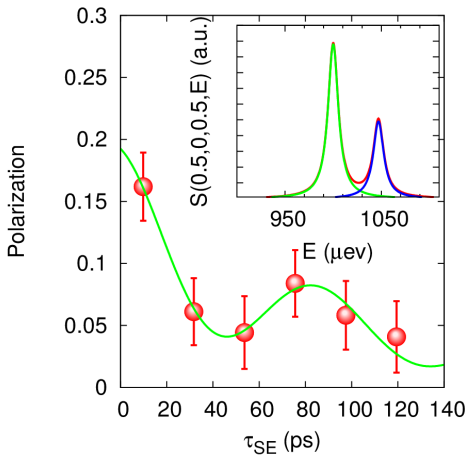

Figure 9.3: Neutron beam polarization as a function of spin echo time in PHCC measured at T = 0.5 K at (0.5,0,0.5). The inset shows the calculated scattering function.

Our target material is piperazinium hexacholorodicuprate (PHCC). This compound is a nearly isotropic (Heisenberg) quasi 2D quantum spin liquid that has been studied extensively by inelastic neutron scattering (INS) [3]. Its derivatives are being extensively studied in our group in the context of Bose Glass physics (see section 9.2.1) [4]. Our first goal was to determine the line width of the magnons in the $T \rightarrow 0$ limit. We focused on excitations at the minimum of their dispersion, i.e., at the antiferromagnetic zone-center, where the spin gap is observed. We employed a combination of INS techniques, namely triple axis spectrometry (TAS) and neutron resonance spin echo (NRSE). The initial TAS study carried out at TASP at PSI showed resolution limited line widths. However, subsequent NRSE investigation at TRISP at the FRM-II facility in Munich led to the observation of a zero field splitting of the magnon line at low temperatures. We were only able to resolve this distinct feature due to the exceptionally high resolution achieved by NRSE. The two magnon lines are split by approximately 50 μeV as shown in figure 9.3. This accurate understanding of the base-temperature spectrum provided the basis of ongoing NRSE and TAS experiments at elevated temperatures, which will be the central focus of this project. All the neutron work is a tight collaboration with Dr. Balint Nafradi from the group of Prof. Forro at EPFL.

The observed zero field splitting of the magnon line in PHCC is in full agreement with parallel ESR studies performed in collaboration with Dr. Glazkov (Kapitza Institute, Moscow, Russia) [5]. Although less direct than NRSE, these systematic measurements detected an even smaller additional splitting of lower-energy excitation doublet. They also provided us with the anisotropy of the g-tensor, which is necessary to understand phase transitions in applied fields (see section 9.2.1). Figure 9.4 shows typical ESR spectra measured for different orientations and temperatures.

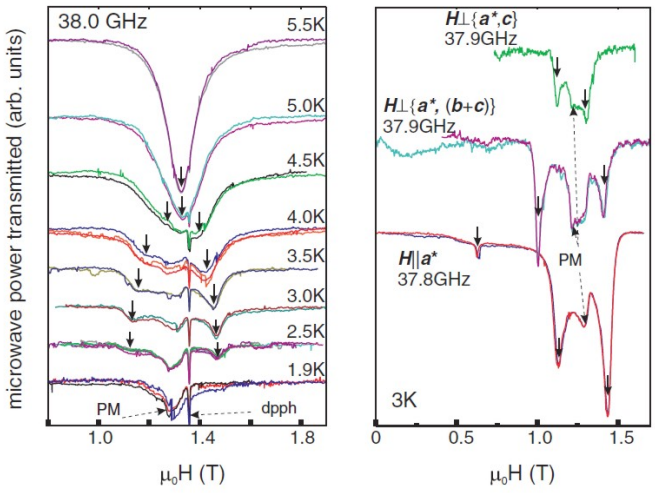

Figure 9.4: Left panel: Temperature dependence of ESR absorption (f = 38.04 GHz, $H||a$.). Right panel: ESR absorption spectra for different orientations at 3.0 K. Vertical arrows mark positions of the resonance absorption due to the triplet excitations.

[1] A. Zheludev *et al*, Phys. Rev. Lett. **100**, 157204 (2008).

[2] B. Náfrádi *et al*, Phys. Rev. Lett. **106**, 177202 (2011).

[3] M. B. Stone *et al.*, PRB **64**, 144405 (2001); New J. Phys. **9**, 31 (2007); Nature **440**, 190 (2006).

[4] D. Hüvonen *et al.*, arXiv:1201.6143v1.

[5] V. Glazkov *et al*, Phys. Rev. B **85**, 054415 (2012).

9.2 Static disorder in quantum magnets

An important component of our research in quantum magnetism is the study of disorder. Quantum ground states, particularly in low-dimensional and frustrated systems, are famously susceptible to randomness. Magnetic materials are now seen as prototypes for the study of magnon localization, Mott and Bose Glasses, and peculiar "almost localized" Random Singlet phases. The study of disorder calls for supplementing momentum-resolved experiments

(neutron scattering) with local-probe measurements, such as μ-SR. During the reporting period,we have achieved considerable progress in understanding excitations and phase transitions in halogen-site-disordered PHCC, ordering in weakly-coupled disordered chains $BaCu_2SiGeO_7$ and a rare *anti*ferromagnetic spin glass $PbFe_{1/2}Ta_{1/2}O_3$.

9.2.1 Spin dynamics in a bond-disordered spin liquid

D. Hüvonen

In quantum spin liquids, elementary excitations are $S = 1$ quasiparticles. In most cases, these *magnons* are long-lived. It is well known that at finite temperatures their lifetimes are reduced due to a finite magnon density and the resulting two-magnon collisions ([1] and references therein). One can expect that the introduction of a weak spatially random component to exchange interactions will produce a similar effect. In the presence of disorder,magnon lifetimes will be reduced even at $T \to 0$ due to collisions with bond-strength defects.

We have performed experiments to study this phenomenon in a quasi-two-dimesional quantum magnet piperazinium hexachlorodicuprate (PHCC) [2]. In PHCC the s = 1/2 Cu^{2+} ions are connected through a complex semi-frustrated network of exchange interactions by Cu-Cl-Cl-Cu bonds in the crystallographic (ac)-planes. We introduce disorder in PHCC by substituting a fraction of the nonmagnetic exchange interaction-mediating Cl ions for the larger ionic radii Br. Such a substitution affects bond angles and lengths, and thereby locally modulates the strength of superexchenge interactions. For neutron scattering studies we have grown fully deuterated samples with 3.5% and 7.5% Br [3].

Initial measurements were performed on the TASP triple axis spectrometer at PSI (Fig. 9.5 left) [4]. Here the solid lines are fits of Lorentzian energy profiles convoluted with the 4-dimensional instrumental resolution function. Compared to pure PHCC, where the magnons are long lived, we observe a clear broadening of excitation lines. From the resolution limited excitation line in pure material, the intrinsic linewidth is increased to Γ=0.1meV and Γ=0.25meV for 3.5% and 7.5% samples, respectively. An ongoing analysis of temperature evolution of the line profiles will allow to make comparisons with temperature induced magnon damping mentioned above.

In addition to drastic reduction of magnon lifetimes, disorder decreases the magnon bandwidth. The magnon spectrum of 3.5% Br sample is seen from the right panel of Fig. 9.5. Here we show two cuts from the full 4-dimensional low energy spectrum measured at time-of-flight instrument CNCS at Oak Ridge National Laboratory. A full quantitative analysis of the data is underway. The observed reduction of bandwidth in disordered samples could have the same origin as a similar effect at finite temperatures: due to collisions magnon motion becomes less propagative and more diffusive [5].

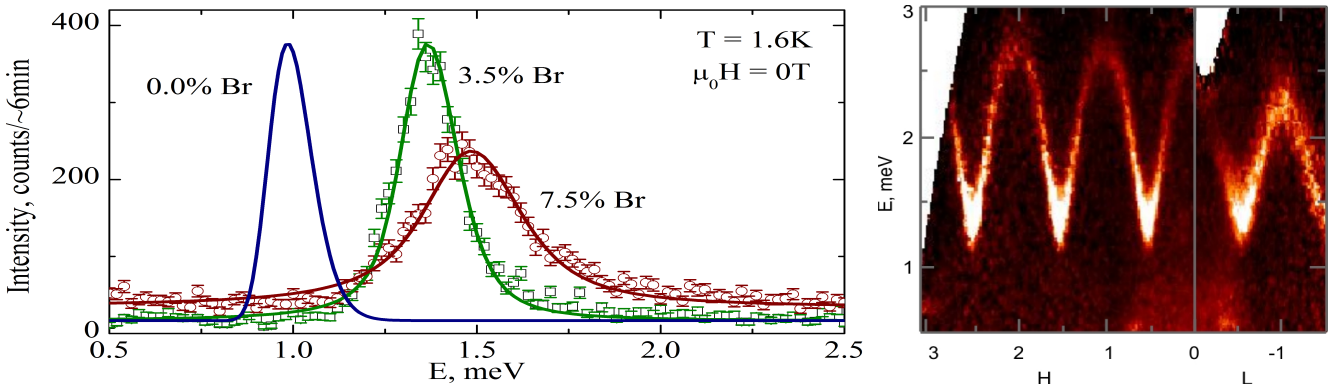

Figure 9.5: Inelastic neutron scattering results. *Left*: constant Q scans at AF zone center (0.5 0.5 -0.5) for 3.5% and 7.5% Br substituted PHCC. Solid lines are simulation and fits of Lorentzian energy profiles convoluted with the 4-dimensional instrumental resolution function for pure and disordered samples, respectively. *Right*: cuts along H and L reciprocal lattice directions from the full 4-dimensional low energy spectrum showing the magnon.

[1] A. Zheludev *et al.*, Phys. Rev. Lett. **100**, 157204 (2008);B. Nafradi *et al.*, Phys. Rev. Lett. **106**, 177202, (2011).
[2] M. Stone et al. New Journal of Physics **9**, 31 (2007).
[3] T. Yankova *et al.*, arXiv:1110.6375 accepted for publishing in the Philosophical Magazine (2011).

[4] D. Hüvonen *et al.*, arXiv:1201.6143 (2012).
[5] Y. Sasago *et al*, Phys. Rev. B **55**, 8357 (1997).

9.2.2 Ordering of coupled Random Singlet chains studied by μSR

M. Thede

In quantum systems, arbitrarily weak disorder may qualitatively alter the ground state. A case in point are gapless quantum spin chains. In the absence of disorder, they realize the Tomonaga-Luttinger spin liquid, where correlations are "protected" by particle-hole symmetry. Introducing disorder in the form of random bonds yields the Random Singlet (RS) phase [1] with quite distinctive universal properties. In experiments on real materials, one has to deal with quasi-one-dimensional spin systems that order in three dimensions at a sufficiently low temperature. However, peculiarities of the RS state in $d = 1$ will translate to unusual features of the ordered phase in $d = 3$ [2].

To experimentally verify this effects we studied the spin-$1/2$ Heisenberg chain compound $BaCu_2(Si_xGe_{1-x})_2O_7$ by μSR. The in-chain exchange constant is $J = 24$ meV for the silicate ($x = 0$) and $J = 50$ meV for germanate ($x = 1$). J is increased by the presence of Ge through its larger ionic radius, which alters the Cu-O-Cu bond angle and consequently the strength of the superexchange interaction. For $x = 0.5$ this results in bond strength disorder and RS properties, as confirmed by magnetic and NMR measurements [3].

We employed μSR to study magnetic ordering in the $x = 0$, $x = 1$ and x=0.5 materials. Both disorder-free compounds show well defined oscillations that indicate long range magnetic order (see Fig. 9.6 left). Two very different muon precessions frequencies are observed in each material due to the presence of two muon sites. The ordering temperatures are T_N=9.2 K for the silicate and T_N=10 K for the germanate. In contrast, the μSR time spectra for $x = 0.5$ do not show any oscillations. They are best described by a stretched exponential $A = A_1 exp(-\lambda t)^\beta + A_{Bg}$. This indicates a broad distribution of fields at the muon sites, which start to develop around 1 K (see Fig 9.6 right). The mean precession frequency is much smaller than of the pure compounds. This behavior is qualitatively consistent with expectations for weakly coupled RS chains.

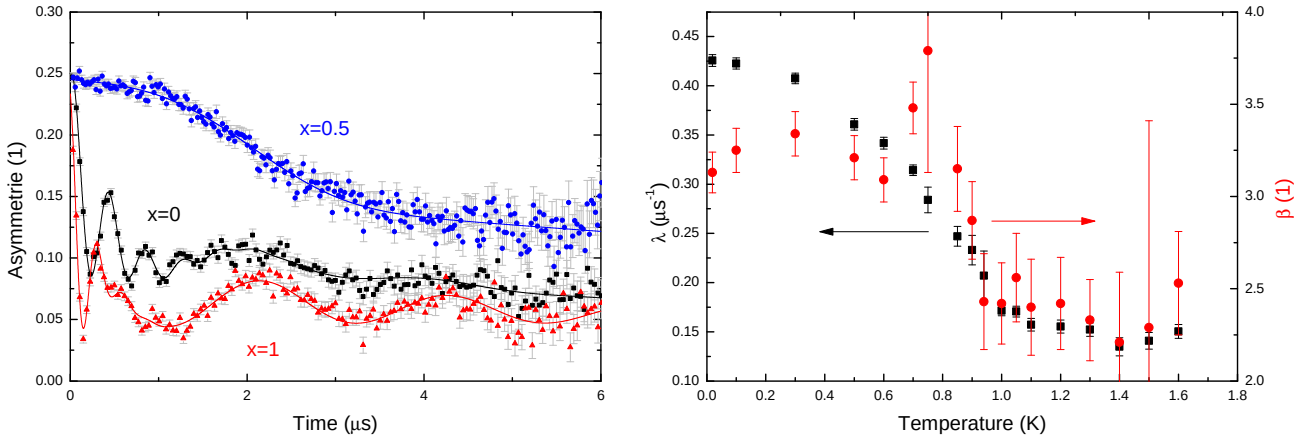

Figure 9.6: left: μSR spectra and fits of $BaCu_2(Si_xGe_{1-x})_2O_7$ for different concentrations right: Fit parameters for the $BaCu_2(Si_0.5Ge_{0.5})_2O_7$ compound as a function of temperature

[1] C. Dasgupta *et al.*, Phys. Rev. B **22**, 1305 (1980); C. Doty *et al.*, Phys. Rev. B **45**, 2167 (1992); H.J. Schulz, Phys. Rev. Lett. **84** 3434, (2000).
[2] A. Joshi *et al.*, Phys. Rev. B **67**, 174403 (2003).
[3] A. Zheludev *et al.*, Phys. Rev. B **75**, 054409 (2007); T. Shiroka *et al*, Phys. Rev. Lett. **106**, 137202 (2011)A.

9.2.3 Bulk Magnetic Properties of $PbFe_{0.5}Ta_{0.5}O_3$

S. Chillal

The chemically disordered cubic system $PbFe_{1/2}Nb_{1/2}O_3$ (PFN) shows a rare co-existence of antiferromagnetism and spin glass properties (AFSG). The interest in this phenomenon has prompted studies of related materials. One of these, $PbFe_{1/2}Ta_{1/2}O_3$ (PFT), is very similar to PFN in terms of the chemical structure. Its magnetic properties are, to date, a source of controversy. Early reports suggest a single Néel temperature at 133 K or 180 K [1]. More recent studies indicate two transition temperatures at ∼55 K and ∼180 K [2], which is in accordance with first principle calculations [3]. However, powder neutron diffraction results show that the Fe^{3+} spins in PFT are arranged in a simple G-type antiferromagnetic structure that remains unchanged down to ∼10 K [4]. To resolve these apparent contradictions, we have performed detailed studied of the bulk magnetic properties of PFT.

Figure 9.7a shows the magnetization of PFT plotted as a function of temperature in zero field cooled (ZFC) and field cooled (FC) regimes in an applied field of 100 Oe field. The anomaly seen at ∼150 K = T_N is the antiferromagnetic ordering transition. The feature at ∼10 K =T_g signifies the emergence of a spin glass (SG) state, directly from the ordered antiferromagnetic phase. The SG character of the low-temperature phase was confirmed by ac-susceptibility measurements. T_g shifts to higher temperature with increasing frequency, as shown in the inset of figure 9.7. The SG phase is further confirmed by the presence of a memory effect. A typical observation in spin-glasses, $M - H$ hysteresis loop, opens in the SG phase of PFT and disappears just above T_g as shown in figure 9.7.b).

We conclude that the coexistence of antiferromagnetism and spin glass properties is quite robust in this family of materials and is not overly sensitive to the non-magnetic substitute. The nature of magnetic ground state of PFT is yet to be verified through neutron diffraction studies.

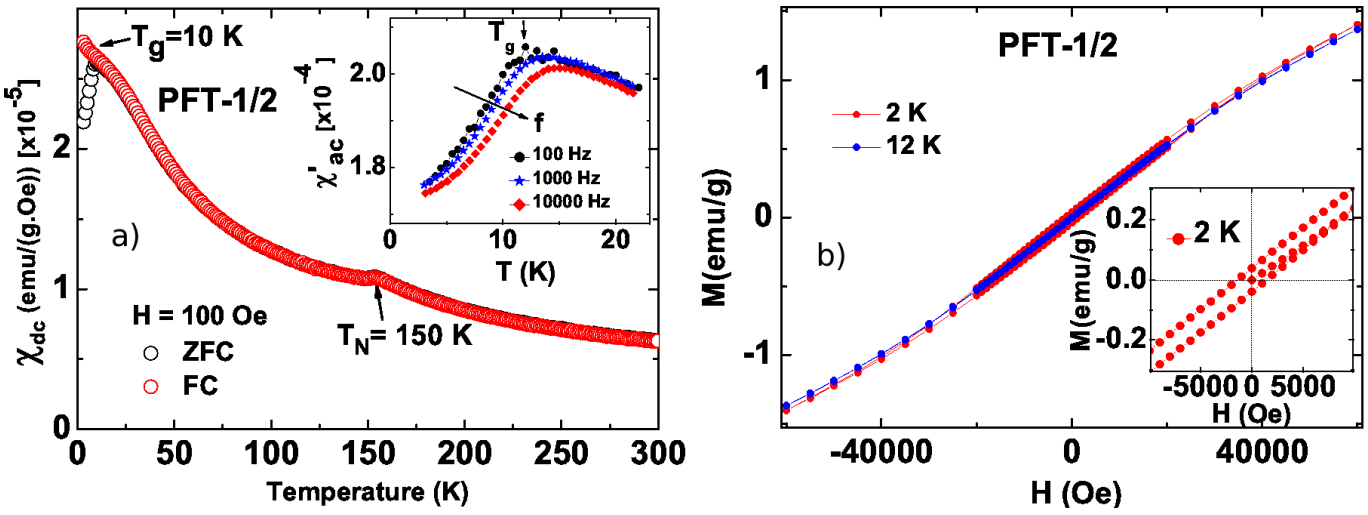

Figure 9.7: a) Magnetization in ZFC and FC regimes. The inset shows ac-susceptibility data where T_g shifts to higher temperatures as the frequency of the applied field increases. b)$M - H$ curves measured above and below T_g.

[1] GL.I. Shvorneva *et al.,* Sov Phys JETP **22**, 722(1965); S. Nomura *et al.,* Japanese jornal of App Phys **7**, 600(1968).
[2] R. Martinez *et al.,* Phys Rev B **82**, 1(2010).
[3] N. Lampis *et al.,* Phys Rev B **69**, 1(2004).
[4] S.A Ivanov *et al.,* Journal of Phys: Cond Matt **13**, 25(2000).

9.3 New research directions

We believe that a constant search for new promising directions and novel experimental techniques is a key component of any successful research effort. To supplement our extensive capabilities in neutron spectroscopy, we have begun

to develop a high-resolution Raman light scattering installation. Simultaneously, we have initiated a search for new quantum magnets with a strong emphasis on geometric frustration and multiferroic properties.

9.3.1 Installation of a Raman spectrometer and the First Results

S.N. Gvasaliya

Raman spectroscopy is a very efficient tool for studying elementary excitations in condensed matter systems. To complement our activity in neutron spectroscopy of solids, we have installed a Raman scattering setup in the laboratory. At present, the spectra can be excited by a semiconductor laser operating at $\lambda = 532.2$ nm. By a confocal microscope the incident beam might be focused on the sample down to few μm. For analysis, we employ a TriVista TR557 triple-grating spectrometer equipped with a liquid nitrogen cooled CCD- detector. The resolution of the setup can be as good as $\sim 0.1\text{cm}^{-1}$, and under favorable conditions the spectra might be recorded down to nearly 1 cm^{-1} from elastic line. Helium flow cryostat with high temperature option allows covering the temperature range of 3.5 K – 650 K.

In the first experiments we addressed the problem of first order Raman spectra observed in cubic relaxor ferroelectrics [1]. For this aim we have studied the disordered non-ferroelectric compound $BaMg_{1/3}Ta_{2/3}O_3$ (BMT) in the temperature range 5 – 600 K. The results were then compared to those on the closely related relaxor ferroelectric $PbMg_{1/3}Ta_{2/3}O_3$ (PMT) [2]. Figure 9.8 shows spectra taken in a backscattering geometry from a single crystal of BMT in two polarizations: polarizers in front and after the sample were parallel (diagonal) and orthogonal (off-diagonal). From the polarization properties and temperature dependencies, we can identify the first-order Raman lines in the spectra of BMT and assign their symmetries as shown. The central finding is that, contrary to expectation, the Raman spectra of BMT and PMT are quite similar. This suggests a disorder-induced origin for the most intense spectral lines.

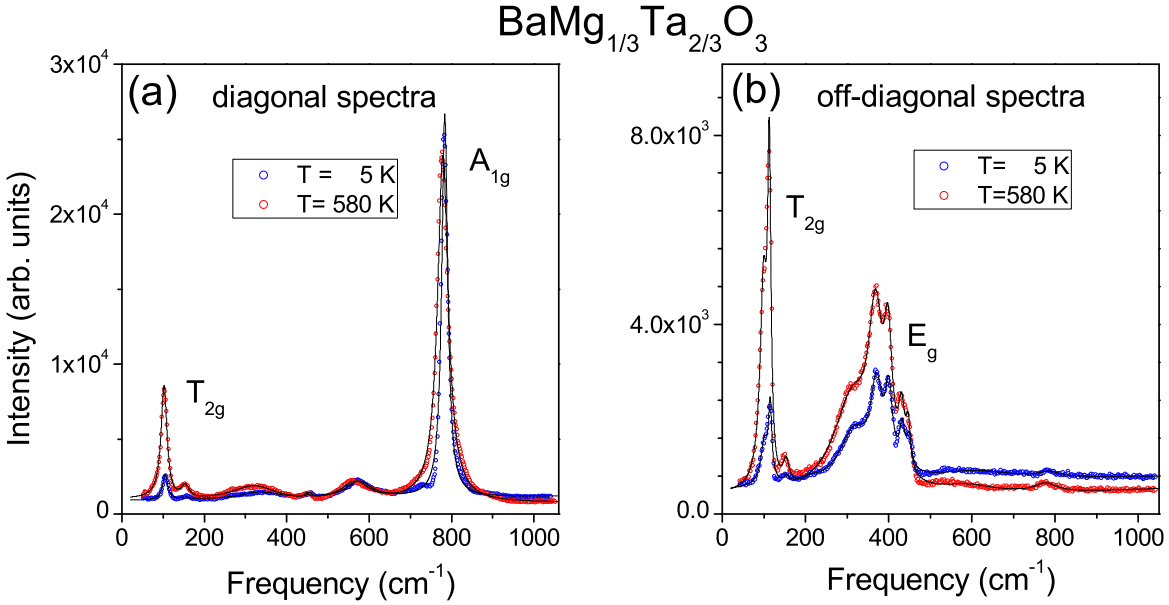

Figure 9.8: Raman spectra from BMT taken in HH (a) and HV (b) geometry. Solid lines correspond to the fits by an appropriate number of harmonic oscillators weighted by the Bose population factor.

[1] I.G. Siny, S.G. Lushnikov, R.S. Katiyar, and V.H. Schmidt, Ferroelectrics **226**, 191 (1999).
[2] S.G. Lushnikov, S.N. Gvasaliya, R.S. Katiyar, Phys Rev B **70**, 172101 (2004).

9.3.2 Search for of novel frustrated quantum magnets

W. EA. Lorenz

A large variety of extraordinary magnetic ground states and most notably of complex dynamics have been revealed in the study of quasi-low-dimensional magnetic materials. The same applies to frustrated systems, like pyrochlores, Kagome-lattices and frustrated chain materials which have attracted manifold interest both experimentally and theoretically. A multitude of compounds which are well described structurally but whose magnetic properties remained unstudied are turning out to be interesting model systems in the field of frustrated magnetism and/or multiferroicity. Three specific cases attracted our attention.

The crystallographic structure of scarce mineral dolerophanite, Cu_2SO_5, exhibits various features promising interesting magnetic properties. The material is composed of SO_4 and OCu_4 tetrahedra [1], the latter of which form a two-dimensional structure as displayed in Fig. 9.9 (left). From the Cu-O-Cu binding angles antiferromagnetic and anti-symmetric exchange interactions can be inferred. The topology of the layer is a complex relative of the Kagome-lattice and alike exhibits magnetic frustration. We have started a study of the magnetic properties of the compound in collaboration with the ETH Laboratory of Inorganic Chemistry. From ongoing studies of the magnetic structure we intend to understand the apparent interplay of frustration and antisymmetric exchange in this exceptional material.

The compound $Ba_2VOSi_2O_7$ [2] is isostructural to the well studied canted anti-ferromagnet $K_2V_3O_8$ (cf. Fig. 9.1). In this non-centrosymmetric space group $P4bm$, a canting of moments out of collinear orientation is not induced by geometric frustration, as in Cu_2SO_5, but solely due to lattice symmetry. $Ba_2VOSi_2O_7$ is hence expected to serve as a model system for the study of anti-symmetric exchange in comparison to $K_2V_3O_8$ [3] as well as to the closely related $Ba_2CuGe_2O_7$ [4]. Our first magnetic characterization on samples obtained in collaboration with Kurt Mattenberger at Physics of New Materials group at the ETH Laboratory for Solid State Physics indicates a significant reduction of exchange interactions compared to $K_2V_3O_8$.

We have been able to obtain large single crystals of $K_2Cu(SO_4)Cl_2$ [5], another scarce mineral whose magnetic properties have not been previously characterized. The material is comprised of zig-zag-chains of Cu[4+2] octahedra, interacting via apical chlorine ions (cf. Fig. 9.9 (right)). From the structure one expects frustrated antiferromagnetic interactions between nearest and next-nearest neighbor interaction. Our first thermodynamic studies show that the compound is indeed magnetically well one-dimensional and weakly frustrated. The rather low exchange integrals as well as the potential chlorine substitution by bromine suggest utilizing this compound for a study of the influence of disorder onto the saturation field in weakly frustrated systems.

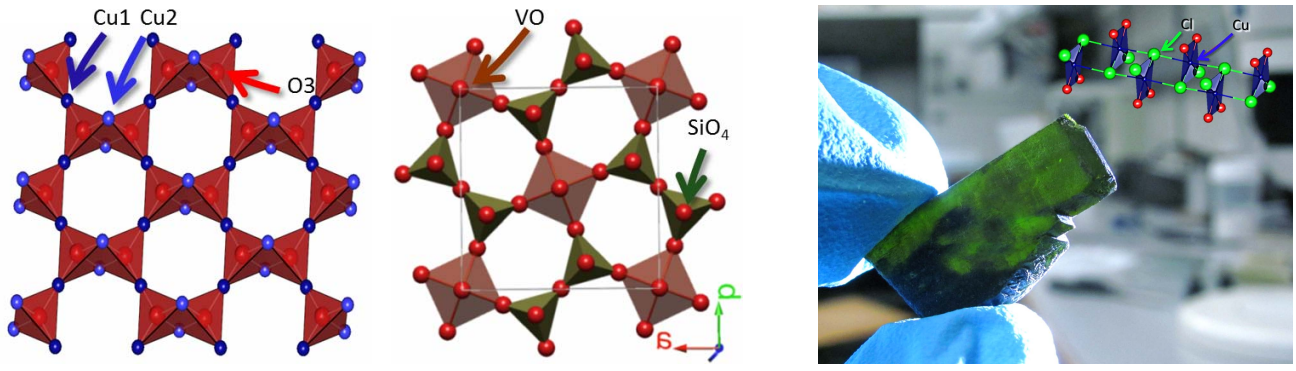

Figure 9.9: Systematic sketchs of the Cu-O-layers in Cu_2SO_5 (left), and $Ba_2VOSi_2O_7$ (middle). Right: Aqueous solution grown single crystal of chlorine substituted $K_2Cu(SO_4)Cl_2$ a protyotypical frustrated spin chain.

[1] H. Effenberger, Monatsh. Chem. **116**, 927 (1985).
[2] K. Ramesha and J. Gopalakrishnan, Solid State Sci.**3** 113 (2001).
[3] M. D. Lumsden *et al.*,, Phys. Rev. Lett. **86**, 159 (2001).
[4] S. Mühlbauer *et al.*,, Phys. Rev. B **84**, 180406 (2011), and references therein
[5] C. Giacovazzo *et al.*,, Z. Kristallogr., **144**, 226 (1976).

Chapter 10

Spin Physics and Imaging

(www.spin.ethz.ch/)

Head
Prof. Christian Degen

Academic Staff

Kevin Chang	Michael Loretz	Brad Moores
Dr. Romana Schirhagl	Ye Tao	

Academic Guests

Johannes Cremer	Tobias Rosskopf

Technical Staff

Cecil Barengo	Julia Tamborini

10.1 Construction of Low-Temperature MRFM Systems for Nano-MRI

Y. Tao, B. Moores, and C. Degen

Access to three-dimensional structures of molecules with atomic resolution would provide a fuller understanding of physical, chemical, and biological processes. As of 2012, rendering structures on the atomic scale presents both a difficult challenge and a major need in science and technology. To meet these needs, we are working to improve the spatial resolution of Magnetic Resonance Imaging (MRI) to about 1 nm. Our experimental approach is based on Magnetic Resonance Force Microscopy (MRFM), a scanning probe method for detecting spin magnetic moments that can achieve sensitivities better than 100 proton nuclei. This sensitivity translates to a spatial imaging resolution of about 5-10 nm.

MRFM consists of a sample attached to the end of an ultrasensitive cantilever. Nuclear spins in the sample are attracted and repelled by a nearby nanomagnet, causing a force on the cantilever. The spins can be periodically flipped using radio-frequency magnetic fields to induce mechanical oscillations in the cantilever, which can be very sensitively measured using laser interferometry. Our current work is focused on improving two central parameters for achieving a better detection sensitivity: Lowering the experimental temperature, which reduced random excitation of the cantilever, and reducing mechanical dissipation. The two efforts will allow us to measure smaller forces.

We are currently setting up an MRFM within a closed-cycle dilution refrigerator (Leiden Cryogenics), capable of a base temperature of 20 mK. One disadvantage of these systems is the high level of magnetic and electric noise produced the pulse-tube cooling circuit, which we have largely eliminated using a series of vibration isolation stages combined with a rigid frame designed by the D-PHYS engineering office. In parallel, we are currently developing single-crystal diamond cantilevers that could potentially offer better quality factors than the state-of-the-art silicon. In addition, we are working on fabricating improved magnetic nanotips to increase the magnetic force generated per spin.

10.2 Single Spin Sensor Attached to an AFM Tip

R. Schirhagl, K. Chang, M. Loretz, J. Cremer, T. Rosskopf, C.L. Degen

Detection of weak magnetic fields at nanometer lengthscales is a long-standing problem in physics. The ability to detect magnetic signatures with high spatial resolution would be important, for example, to better understand superconductivity, to realize spin-based quantum devices, or to perform high-resolution NMR microscopy and spectroscopy. A main goal of our group is to perform magnetometry with a magnetic sensor attached to an atomic force microscope (AFM) tip, which greatly improves the spatial resolution of conventional magnetometry. The Nitrogen Vacancy (NV-) center, a defect center in diamond, is a promising candidate for such a sensor due to its optically-detectable sensitivity to magnetic fields.

To this end, a home-built AFM was combined with a confocal microscope. Fluorescence detection enables us to select a diamond nanocrystal (diameter < 50 nm) with an NV- center, which is naturally present in 0.1% of nanodiamonds. In order to attach a diamond nanocrystal with an AFM tip, it is necessary to modify the surface of the tip (see 10.1.1(c)). The OH groups on the surface of a silicon AFM-tip are brought to reaction with ethanolamine. The electropositive NH_2 groups on the AFM tip can interact with the electronegative surface of oxygen terminated nanodiamonds. The modified AFM tip is then brought in contact with the diamond, which sticks and attaches to the tip. The presence of the diamond on the tip can be confirmed by SEM (see 10.1. 1(d)).

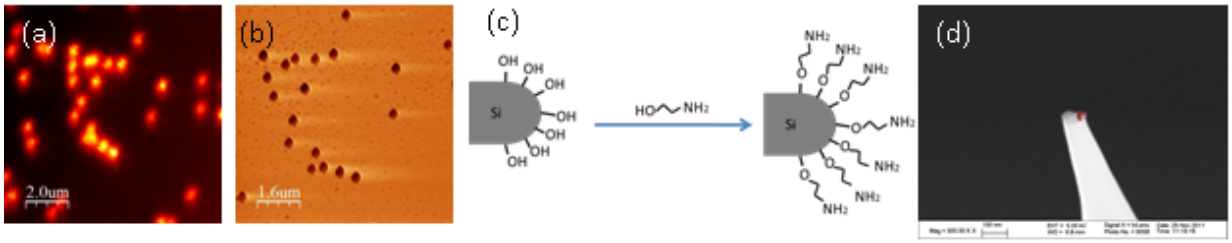

Figure 10.1: (a) Confocal image of fluorescent beads and (b) the same area on an AFM-scan. (c) A schematic drawing of the chemical reaction between OH groups on the surface of a standard silicon AFM-tip and ethanolamine. This reaction was used to obtain an AFM-probe with an electropositive surface enabling us to pick up electronegative diamond particles. (d) SEM image of the resulting AFM/tip after picking up a nanodiamond (false color).

In a next step, these magnetic sensing probes will be used to scan the magnetic signature of different nanostructured test samples.

Chapter 11

Publications

Y. Acremann, H.C. Siegmann
Nanoscale dynamics in magnetism
Handbook of nanophysics. 1, Principles and methods

A. Alfonsov, F. Murányi, V. Kataev, G. Lang, N. Leps, L. Wang, R. Klingeler, A. Kondrat, C. Hess, S. Wurmehl, A. Köhler, G. Behr, S. Hampel, M. Deutschmann, S. Katrych, N. D. Zhigadlo, Z. Bukowski, J. Karpinski, and B. Büchner
High-field electron spin resonance spectroscopy study of $GdFeAsO_{1-x}F_x$ superconductors
Phys. Rev. B **83**, 094526 (2011)

A. Bachowski, K. Ruebenbauer, J. Bukrowski, K. Rogacki, Z. Bukowski, and J. Karpinski
Shape of spin density wave versus temperature in AFe_2As_2(A = Ca, Ba, Eu): A Mössbauer study
Phys. Rev. B **83**, 134410 (2011)

M. Baur, S. Filipp, R. Bianchetti, J.M. Fink, M. Goeppl, L. Steffen, P.J. Leek, A. Blais, and A. Wallraff
Measurement of Autler-Townes and Mollow transitions in a strongly driven superconducting qubit
Phys. Rev. Lett. **102**, 243602 (2009)

D. P. Bernstein, B. Bräuer, R. Kukreja, J. Stöhr , T. Hauet J. Cucchiara, S. Mangin, J.A. Katine, T. Tyliszczak, K.W. Chou , Y. Acremann
Nonuniform switching of the perpendicular magnetization in a spin-torque-driven magnetic nanopillar
Phys. Rev. B **83**, 180410(R) (2011)

D. Bischoff, J. Güttinger, S. Dröscher, T. Ihn, K. Ensslin, and C. Stampfer
Raman spectroscopy on etched graphene nanoribbons
J. Appl. Phys. **109**, 073710 (2011)

L. Bockhorn, P. Barthold, D. Schuh, W. Wegscheider, and R.J. Haug
Magnetoresistance in a High-mobility Two-dimensional Electron Gas
Phys. Rev. B **83**, 113301 (2011)

D. Bozyigit, C. Lang, L. Steffen, J. M. Fink, C. Eichler, M. Baur, R. Bianchetti, P. J. Leek, S. Filipp, M. P. da Silva, A. Blais, and A. Wallraff
Antibunching of microwave-frequency photons observed in correlation measurements using linear detectors
Nature Physics **7**, 154-158 (2011)

D. Bozyigit, C. Lang, L. Steffen, J.M. Fink, C. Eichler, M. Baur, R. Bianchetti, P.J. Leek, S. Filipp, M.P. da Silva, A. Blais, and A. Wallraff
Correlation Measurements of Individual Microwave Photons Emitted from a Symmetric Cavity
Journal of Physics: Conference Series **264**, 012024 (2011)

B. Bräuer, R. Kukreja, A. Virkar, H. B. Akkerman, A. Fognini, T. Tyliszczak, and Z. Bao
Carrier mobility in pentacene as a function of grain size and orientation derived from scanning transmission X-ray microscopy
Organic Electronics **12**, p. 1936-1942 (2011)

M. Ciszek, K. Rogacki, and J. Karpinski
Effect of carbon substitution on low magnetic field AC losses in MgB_2 single crystals
Physica C: Superconductivity, doi:10,1016/j.physc.2011.05.057

N. Daniilidis, S. Narayanan, S. A. Moeller, R. Clark, T. E. Lee, P. J. Leek, A. Wallraff, St. Schulz, F. Schmidt-Kaler, and H. Haeffner
Fabrication and heating rate study of microscopic surface electrode ion traps
New Journal of Physics **13**, 013032 (2011) , also arXiv:1009.2834

M. Davanço, M.T. Rakher, W. Wegscheider, D. Schuh, A. Badolato, and K. Srinivasan
Efficient Quantum Dot Single Photon Extraction into an Optical Fiber Using a Nanophotonic Directional Coupler
App. Phys. Lett. **99**, 121101 (2011)

C. L. Degen, and J. P. Home,
Cold-atom microscope shapes up
Nature Nanotechnology **6**, 399 (2011)

L. Degiorgi
Electronic correlations in iron-pnictide superconductors and beyond: lessons learned from optics
New J. Phys. **13**, 023011 (2011)

S. Dröscher, H. Knowles, Y. Meir, K. Ensslin, and T. Ihn
Coulomb gap in graphene nanoribbons
Phys. Rev. B **84**, 073405 (2011)

A. Dusza, A. Lucarelli, F. Pfuner, J.-H. Chu, I. R. Fisher, and L. Degiorgi
Anisotropic charge dynamics in detwinned $Ba(Fe_{1-x}Co_x)_2As_2$
Europhys. Lett. **93**, 37002 (2011) and Europhysics News **42** (3) (2011)

C. Eichler, D. Bozyigit, C. Lang, M. Baur, L. Steffen, J. M. Fink, S. Filipp, and A. Wallraff
Observation of Two-Mode Squeezing in the Microwave Frequency Domain
Phys. Rev. Lett. **107**, 113601 (2011)

C. Eichler, D. Bozyigit, C. Lang, L. Steffen, J. Fink, and A. Wallraff
Experimental State Tomography of Itinerant Single Microwave Photons
Phys. Rev. Lett. **106**, 220503 (2011)

C.V. Falub, U. Mueller, G. Thorwarth, M. Parlinska-Wojtan, C. Voisard, and R. Hauert
In vitro studies of the adhesion of diamond-like carbon thin films on CoCrMo biomedical implant alloy
Acta Mater. **59**, 4678 (2011)

A. Fedorov, L. Steffen, M. Baur, M. P. da Silva, and A. Wallraff
Implementation of a Toffoli gate with superconducting circuits
Nature **481**, 170-172 (2011), also in arXiv:1108.3966

S. Filipp, A.F. van Loo, M. Baur, L. Steffen, and A. Wallraff
Preparation of Subradiant States using Local Qubit Control in Circuit QED
Phys. Rev. A Rapid Comm. **84**, 061805 (2011), also in arXiv:1107.2078

S. Filipp, M. Göppl, J. M. Fink, M. Baur, R. Bianchetti, L. Steffen, and A. Wallraff
Multi-Mode Mediated Qubit-Qubit Coupling and Dark-State Symmetries in Circuit Quantum Electrodynamics
Phys. Rev. A **83**, 063827 (2011), also in arXiv:1011.3732

I.R. Fisher, L. Degiorgi and Z.X. Shen
In-plane electronic anisotropy of underdoped '122' Fe-arsenide superconductors revealed by measurements of detwinned single crystals
Rep. Prog. Phys. **74**, 124506 (2011)

T. Frey, P. J. Leek, M. Beck, K. Ensslin, A. Wallraff, T. Ihn
Characterization of a microwave frequency resonator via a nearby quantum dot
Appl. Phys. Lett. **98**, 262105 (2011), also in arXiv:1104.3535

V.N. Glazkov, G. Dhalenne, A. Revcolevschi, and A. Zheludev
Multiple spin-flop phase diagram of $BaCu_2Si_2O_7$
J. Phys.: Condens. Matter **23**, 086003 (2011)

Z. Guguchia, J. Roos, A. Shengelaya, S. Katrych, Z. Bukowski, S. Weyeneth, F. Murányi, S. Strässle, A. Maisuradze, J. Karpinski, and H. Keller
Strong coupling between Eu^{2+} spins and Fe_2As_2 layers in $EuFe_{1.9}Co_{0.1}As_2$ observed with NMR
Phys. Rev. B **83**, 144516 (2011)

Z. Guguchia, Z. Shermadini, A. Amato, A. Maisuradze, A. Shengelaya, Z. Bukowski, H. Luetkens, R. Khasanov, J. Karpinski, and H. Keller
Muon-spin rotation measurements of the magnetic penetration depth in the iron-based superconductor $Ba_{1-x}Rb_xFe_2As_2$
Phys. Rev. B **84**, 094513 (2011)

Z. Guguchia, S. Bosma, S. Weyeneth, A. Shengelaya, R. Puzniak, Z. Bukowski, J. Karpinski, and H. Keller
Anisotropic magnetic order of the Eu sublattice in single crystals of $EuFe_{2-x}Co_xAs_2$ (x=0,0.2) studied by means of magnetization and magnetic torque
Phys. Rev. B **84**, 144506 (2011)

S. Gustavsson, C. Rössler, T. Ihn, and K. Ensslin
Wenn einzelne Elektronen zählen
Physik Journal **10**, 33 (2011)

J. Güttinger, J. Seif, C. Stampfer, A. Capelli, K. Ensslin, and T. Ihn
Time-resolved charge detection in graphene quantum dots
Phys. Rev. B **83**, 165445 (2011)

J. Güttinger, C. Stampfer, T. Frey, T. Ihn, and K. Ensslin
Transport through a strongly coupled graphene quantum dot in perpendicular magnetic field
Nanoscale Research Letters **6**, 253 (2011)

M. Hirmer, D. Schuh, and W. Wegscheider
Carbon doped InAlAs/InGaAs/InAs Heterostructures: Tuning from n- to p-doping
App. Phys. Lett. **98**, 082103 (2011)

M. Hirmer, M. Hirmer, D. Schuh, W. Wegscheider, T. Korn, R. Winkler, and C. Schuller
Fingerprints of the Anisotropic Spin-split Hole Dispersion in Resonant Inelestic Light Scattering in Two-dimensional Hole Systems
Phys. Rev. Lett. **107**, 216805 (2011)

S.D. Hogan, J.A. Agner, F. Merkt, T. Thiele, S. Filipp, and A. Wallraff
Driving Rydberg-Rydberg transitions from a co-planar microwave waveguide
Phys. Rev. Lett. (2011), also in arXiv:1110.1256

T. Hong, S.N. Gvasaliya, S. Herringer, M.M. Turnbull, C.P. Landee, L.-P. Regnault, M. Boehm, and A. Zheludev
Dynamics of the two-dimensional S=1/2 dimer system $(C_5H_6N_2F)_2CuCl_4$
Phys. Rev. B **83**, 052401 (2011)

R. Häusermann, and B. Batlogg
Gate bias stress in pentacene field-effect-transistors: Charge trapping in the dielectric or semiconductor
Appl. Phys. Lett. **99**, 083303 (2011)

M. Hüfner, B. Küng, S. Schnez, K. Ensslin, T. Ihn, M. Reinwald, and W. Wegscheider
Spatial Mapping and Manipulation of Two Tunnel-coupled Quantum Dots
Phys. Rev. B **83**, 235326 (2011)

M. Hüfner, S. Schnez, B. Kueng, T. Ihn, M. Reinwald, W. Wegscheider, and K. Ensslin
Mapping leakage currents in a nanostructure fabricated via local anodic oxidation
Nanotechnology **22**, 295306 (2011)

R. Kaufmann, G. Isella, A. Sanchez-Amores, S. Neukom, A. Neels, L. Neumann, A. Brenzikofer, A. Dommann, C. Urban, and H. von Känel
Near infrared image sensor with integrated germanium photodiodes
J. Appl. Phys. **110**, 023107 (2011)

R. Khasanov, S. Sanna, G. Prando, Z. Shermadini, M. Bendele, A. Amato, P. Carretta, R. De Renzi, J. Karpinski, S. Katrych, H. Luetkens, and N.D. Zhigadlo
Tuning of competing magnetic and superconducting phase volumes in $LaFeAsO_{0.945}F_{0.055}$ by hydrostatic pressure
Phys. Rev. B **84**, 100501 (2011)

S. Knott, T. Hirschmann, U. Wurstbauer, W. Hansen, and W. Wegscheider
Magnetoresistance Effects and Phase Coherent Transport Phenomena in a Magnetic Nonplanar Two-dimensional Hole System
Phys. Rev. B **84**, 205302 (2011)

K. Kowalik-Seidl, X.P. Vögele, F. Seilmeier, D. Schuh, W. Wegscheider, A.W. Holleitner, and J.P. Kotthaus
Forming and Confining of Dipolar Excitons by Quantizing Magnetic Fields
Phys. Rev. B **83**, 081307(R) (2011)

A. Kriisa, R.G. Mani, and W. Wegscheider
Hall Effects in Doubly Connected Specimens
IEEE Transactions on Nanotechnology **10**, 179 (2011)

M. Kugler, K. Korzekwa, P. Machnikowski, C. Gradl, S. Furthmeier, M. Griesbeck, M. Hirmer, D. Schuh, W. Wegscheider, T. Kuhn, C. Schüller, and T. Korn
Decoherence-assisted Initialization of a Resident Hole Spin Polarization in a p-doped Semiconductor Quantum Well

C. Lang, D. Bozyigit, C. Eichler, L. Steffen, J. M. Fink, A.A. Abdumalikov Jr., M. Baur, S. Filipp, M.P. da Silva, A. Blais, and A. Wallraff
Observation of Resonant Photon Blockade at Microwave Frequencies using Correlation Function Measurements
Phys. Rev. Lett. **106**, 243601 (2011), also in arXiv:1102.0461

M. Le Tacon, T.R. Forrest, Ch. Rüegg, A. Bosak, J. Noffsinger, A.C. Walters, P. Toulemonde, A. Palenzona, N.D. Zhigadlo, J. Karpinski, J.P. Hill, M. Krisch, and D. F. McMorrow
Inelastic X-ray scattering investigations of lattice dynamics in $SmFeAsO_{1-x}F_y$ superconductors
J. Phys. Chem. Solids **72**, 523-526 (2011)

V. Lechner, L.E. Golub, F. Lomakina, V.V. Bel'kov, P. Olbrich, S. Stachel, I. Caspers, M. Griesbeck, M. Kugler, M.J. Hirmer, T. Korn, C. Schüller, D. Schuh, W. Wegscheider, and S.D. Ganichev
Spin and Orbital Mechanisms of the Magnetogyrotropic Photogalvanic Effects in $GaAs/Al_xGa_{1-x}As$ Quantum Well Structures
Phys. Rev. B **83**, 155313 (2011)

G. Li, G. Grissonnanche, A. Gurevich, N.D. Zhigadlo, S. Katrych, Z. Bukowski, J. Karpinski, and L. Balicas
Multiband superconductivity in $LaFeAsO_{0.9}F_{0.1}$ single crystals probed by high-field vortex torque magnetometry
Phys. Rev. B **83**, 214505 (2011)

R.G. Mani, and W. Wegscheider
Comparative Study of Microwave Radiation-Induced Magnetoresistance Oscillations in GaAs/AlGaAs Devices
IEEE Transactions on Nanotechnology **10**, 170 - 173 (2011)

R.G. Mani, and A.N. Ramanayaka
Observation of Linear-Polarization-Sensitivity in the Microwave-Radiation-Induced Magnetoresistance Oscillations
Phys. Rev. B **84**, 085308 (2011)

M. Matusiak, Z. Bukowski, and J. Karpinski
Doping dependence of the Nernst effect in $Eu(Fe_{1-x}Co_x)_2As_2$: Departure from Dirac-fermion physics
Phys. Rev. B **83**, 224505 (2011)

T. Mertelj, P. Kusar, L. Stojchevska, V.V. Kabanov, N.D. Zhigadlo, S. Katrych, J. Karpinski, and D. Mihailovic
Doping dependent quasiparticle relaxation dynamics in $SmFeAsO_{1-x}F_x$ single crystals: comparison of spin-density wave and superconducting states
J. Supercond. Nov. Magn. **24**, 489-493 (2011)

S. Miesch, A. Fognini, Y. Acremann, A. Vaterlaus, and T. Michlmayr
Fe on W(110), a stable magnetic reference system
J. Appl. Phys. **109**, 013905 (2011)

F. Molitor, J. Güttinger, C. Stampfer, S. Dröscher, A. Jacobsen, T. Ihn, and K. Ensslin
Electronic properties of graphene nanostructures
Topical Review, J. Phys. C **23**, 243201 (2011)

P.J.W. Moll, J. Kanter, R.D. McDonald, F.F. Balakirev, P. Blaha, K. Schwarz, Z. Bukowski, N.D. Zhigadlo, S. Katrych, K. Mattenberger, J. Karpinski, and B. Batlogg
Quantum oscillations of the superconductor $LaRu_2P_2$: Comparable mass enhancement $\lambda \approx 1$ in Ru and Fe phosphides
Phys. Rev. B **84**, 004500 (2011)

S. Mühlbauer, S.N. Gvasaliya, E. Pomjakushina, and A. Zheludev
Double-k phase of the Dzyaloshinskii-Moriya helimagnet $Ba_2CuGe_2O_7$
Phys. Rev. B **84**, 180406 (2011)

C. Müller, N.D. Zhigadlo, A. Kumar, M.A. Baklar, J. Karpinski, P. Smith, T. Kreouzis, and N. Stingelin
Enhanced charge-carrier mobility in high-pressure-crystallized poly(3-hexylthiophene)
Macromolecules **44**, 6, 1221-1225 (2011)

U. Müller, C.V. Falub, G. Thorwarth, C. Voisard, and R. Hauert
Diamond-like carbon coatings on a CoCrMo implant alloy: A detailed XPS analysis of the chemical states at the interface
Acta Materialia **59**, 3, 1150-1161 (2011)

B. Náfrádi, T. Keller, H. Manaka, A. Zheludev, and B. Keimer
Low-Temperature Dynamics of Magnons in a Spin-1/2 Ladder Compound
Phys. Rev. Lett. **106**, 177202 (2011)

S. Nakamura, Y. Yamauchi, M. Hashisaka, K. Chida, K. Kobayashi, T. Ono, R. Leturcq, K. Ensslin, K. Saito, Y. Utsumi, and A. C. Gossard
Fluctuation Theorem and Microreversibility in a Quantum Coherent Conductor
Phys. Rev. B **83**, 155431 (2011)

K.C. Nowack, M. Shafiei, M. Laforest, G.E.D.K. Prawiroatmodjo, L.R. Schreiber, C. Reichl, W. Wegscheider, L.M.K. Vandersypen
Single-Shot Correlations and Two-Qubit Gate of Solid-State Spins
Science **333**, 1269 (2011)

A.N. Ramanayaka, R.G. Mani, W. Wegscheider
Microwave-induced Electron Heating in the Regime of Radiation-induced Magnetoresistance Oscillations
Phys. Rev. B **83**, 165303 (2011)

P. Roulleau, S. Baer, T. Choi, F. Molitor, J. Güttinger, T. Müller, S. Dröscher, K. Ensslin and T. Ihn
Coherent electron-phonon coupling in tailored quantum systems
Nature Com. **2**, 239 (2011)

C. Rössler, S. Baer, E. de Wiljes, P.-L. Ardelt, T. Ihn, K. Ensslin, C. Reichl, and W. Wegscheider
Transport Properties of Clean Quantum Point Contacts
New Journal of Physics **13**, 113006 (2011)

A. Sanna, F. Bernardini, G. Profeta, S. Sharma, J. K. Dewhurst, A. Lucarelli, L. Degiorgi, E. K. U. Gross, and S. Massidda
Theoretical investigation of optical conductivity in $Ba(Fe_{1-x}Co_x)_2As_2$
Phys. Rev. B **83**, 054502 (2011)

S. Sanna, P. Carretta, P. Bonfà, G. Prando, G. Allodi, R. De Renzi, T. Shiroka, G. Lamura, A. Martinelli, and M. Putti,
Correlated Trends of Coexisting Magnetism and Superconductivity in Optimally Electron-Doped Oxypnictides
Phys. Rev. Lett. **107**, 227003 (2011)

G. Schiltz, U. Braendle, A. Reinhardt, and M. Valkering
Lehr- und Lerntechnologie an der ETH Zürich
E-Learning : Einsatzkonzepte und Erfolgsfaktoren des Lernens mit interaktiven Medien

D. Schmidiger, S. Mühlbauer, S.N. Gvasaliya, T. Yankova, and A. Zheludev
Long-lived magnons throughout the Brillouin zone of the strong-leg spin ladder $(C_7D_{10}N)_2CuBr_4$
Phys. Rev. B **84**, 144421 (2011)

S. Schnez, C. Rössler, T. Ihn, K. Ensslin, C. Reichl, and W. Wegscheider
Imaging the Lateral Shift of a Quantum Point Contact Using Scanning Gate Microscopy
Phys. Rev. B **84**, 195322 (2011)

S. Schnez, C. Rössler, T. Ihn, K. Ensslin, C. Reichl, and W. Wegscheider
Imaging the lateral shift of a quantum point contact using scanning gate microscopy
Phys. Rev. B **84**, 195322 (2011)

L.R. Schreiber, F.R. Braakman, T. Meunier, V. Calado, J. Danon, J.M. Taylor, W. Wegscheider, and L.M.K. Vandersypen
Coupling Artificial Molecular Spin States by Photon-assisted Tunneling
Nature Communications **2**, 556 (2011)

J. Shiogai, D. Schuh, W. Wegscheider, M. Kohda, J. Nitta, and D. Weiss
Magnitude and Sign Control of Lithography-induced Uniaxial Anisotropy in Ultra-thin (Ga,Mn)As Wires
Appl. Phys. Lett. **98**, 083101 (2011)

T. Shiroka, F. Casola, V. Glazkov, A. Zheludev, K. Prša, H.-R. Ott, and J. Mesot
Distribution of NMR Relaxations in a Random Heisenberg Chain
Phys. Rev. Lett. **106**, 137202 (2011)

T. Shiroka, G. Lamura, R. De Renzi, M. Belli, N. Emery, H. Rida, S. Cahen, J.-F. Marêché, and C. Hérold
μSR investigation of the intercalated graphite superconductor CaC_6
N J Phys. **13** 013038 (2011)

T. Shiroka, G. Lamura, S. Sanna, G. Prando, R. De Renzi, M. Tropeano, M. R. Cimberle, A. Martinelli, C. Bernini, A. Palenzona, R. Fittipaldi, A. Vecchione, P. Carretta, A. S. Siri, C. Ferdeghini, and M. Putti
Long- to short-range magnetic order in fluorine-doped CeFeAsO
Phys Rev. B **84**, 195123 (2011)

C. Stampfer, S. Fringes, J. Güttinger, F. Molitor, C. Volk, B. Terres, J. Dauber, S. Engels, S. Schnez, A. Jacobsen, S. Dröscher, T. Ihn, and K. Ensslin
Transport in Graphene Nanostructures
Frontiers of Physics **6**, 271 (2011)

V.M. Stojanovic, A. Fedorov, C. Bruder, and A. Wallraff
Quantum-control approach to realizing a Toffoli gate in circuit QED
Physical Review B (2011), also in arXiv:1108.3442

M. Studer, M. Hirmer, D. Schuh, W. Wegscheider, K. Ensslin, and G. Salis
Optical Polarization of Localized Hole Spins in p-doped Quantum Wells
Phys. Rev. B **84**, 085328 (2011)

D. Taubert, G. J. Schinner, C. Tomaras, H. P. Tranitz, W. Wegscheider, and S. Ludwig
An electron jet pump: The Venturi effect of a Fermi liquid
J. App. Phys. **109**, 102412 (2011)

D. Taubert, C. Tomaras, G.J. Schinner, H.P. Tranitz, W. Wegscheider, S. Kehrein, and S. Ludwig
Relaxation of Hot Electrons in a Degenerate Two-dimensional Electron System: Transition to One-dimensional Scattering
Phys. Rev. B **83**, 235404 (2011)

D. Taubert, D. Schuh, W. Wegscheider, and S. Ludwig
Determination of Energy Scales in Few-electron Double Quantum Dots
Rev. of Sci. Instr. **82**, 123905 (2011)

D. Tutuc, B. Popescu, D. Schuh, W. Wegscheider, and R.J. Haug
Tunable Nonlocal Coupling Between Kondo Impurities
Phys. Rev. B **83**, 241308(R) (2011)

I. A. Vartanyants, A. Singer, A. P. Mancuso, O. M. Yefanov, A. Sakdinawat, Y. Liu, E. Bang, G. J. Williams, G. Cadenazzi, B. Abbey, H. Sinn, D. Attwood, K. A. Nugent, E. Weckert, T. Wang, D. Zhu, B. Wu, C. Graves, A. Scherz, J. J. Turner, W. F. Schlotter, M. Messerschmidt, J. Luning, Y. Acremann, P. Heimann, D. C. Mancini, V. Joshi, J. Krzywinski, R. Soufli, M. Fernandez-Perea, S. Hau-Riege, A. G. Peele, Y. Feng, O. Krupin, S. Moeller, and W. Wurth
Coherence Properties of Individual Femtosecond Pulses of an X-Ray Free-Electron Laser
Phys. Rev. Lett. **107**, 144801 (2011)

I. A. Vartanyants, A. Singer, A. P. Mancuso, O. M. Yefanov, A. Sakdinawat, Y. Liu, E. Bang, G. J. Williams, G. Cadenazzi, B. Abbey, H. Sinn, D. Attwood, K. A. Nugent, E. Weckert, T. Wang, D. Zhu, B. Wu, C. Graves, A. Scherz, J. J. Turner, W. F. Schlotter, M. Messerschmidt, J. Luning, Y. Acremann, P. Heimann, D. C. Mancini, V. Joshi, J. Krzywinski, R. Soufli, M. Fernandez-Perea, S. Hau-Riege, A. G. Peele, Y. Feng, O. Krupin, S. Moeller, and W. Wurth
Coherence Properties of Individual Femtosecond Pulses of an X-Ray Free-Electron Laser
Physical review. Special topics. Accelerators and beams

R. Völkl, M. Griesbeck, S.A. Tarasenko, D. Schuh, W. Wegscheider, C. Schüller, and T. Korn
Spin Dephasing and Photoinduced Spin Diffusion in a High-mobility Two-dimensional Electron System Embedded in a GaAs-(Al,Ga)As Quantum Well Grown in the [110] Direction
Phys. Rev. B **83**, 241306(R) (2011)

U. Welp, C. Chaparro, A. E. Koshelev, W. K. Kwok, A. Rydh, N. D. Zhigadlo, J. Karpinski, and S. Weyeneth
Anisotropic phase diagram and superconducting fluctuations of single-crystalline $SmFeAsO_{0.85}F_{0.15}$
Phys. Rev. B **83**, 100513 (2011)

S. Weyeneth, P.J.W. Moll, R. Puzniak, K. Ninios, F.F. Balakirev, R.D. McDonald, H.B. Chan, N.D. Zhigadlo, S. Katrych, Z. Bukowski, J. Karpinski, H. Keller, B. Batlogg, and L. Balicas
Rearrangement of the antiferromagnetic ordering at high magnetic fields in SmFeAsO and $SmFeAsO_{0.9}F_{0.1}$ single crystals
Phys. Rev. B **83**, 134503 (2011)

E. Wulf, S. Mühlbauer, T. Yankova, and A. Zheludev
Disorder instability of the magnon condensate in a frustrated spin ladder
Phys. Rev. B **84**, 174414 (2011)

X. W. Yu, V. S. Pribiag, Y. Acremann, A. A. Tulapurkar, T. Tyliszczak, K. W. Chou, B. Bräuer, Z.-P. Li, O. J. Lee, P. G. Gowtham, D. C. Ralph, R. A. Buhrman, and J. Stöhr
Images of a Spin-Torque-Driven Magnetic Nano-Oscillator
Phys. Rev. Lett. **106**, 167202 (2011)

A. Zheludev and D. Hüvonen
Transition from Bose glass to a condensate of triplons in $Tl_{1-x}K_xCuCl_3$
Phys. Rev. B **83**, 216401 (2011)

N.D. Zhigadlo, S. Katrych, M. Bendele, P.J.W. Moll, M. Tortello, S. Weyeneth, V. Yu. Pomjakushin, J. Kanter, R. Puzniak, Z. Bukowski, H. Keller, R.S. Gonnelli, R. Khasanov, J. Karpinski, and B. Batlogg
Interplay of composition, structure, magnetism, and superconductivity in $SmFeAs_{1-x}P_xO_{1-y}$
Phys. Rev. B **84**, 134526 (2011)

Chapter 12

Presentations

(⋆ = invited talk)

12.1 Talks

⋆ Acremann, Y.
X-ray imaging of magneto-dynamics on the nanometer scale
University of Hamburg, Germany, 11.1.2011

⋆ Acremann, Y.
Magnetic vortices: From a 'hidden parameter' to novel switching modes
APS March Meeting 2011, Dallas, TX, USA

⋆ Acremann, Y.
Magnetization dynamics on the nanoscale
SPS annual meeting, Lausanne, June 2011

⋆ Acremann, Y.
Single shot magnetometry using free electron laser radiation
MAGDYN-Conference, Synchrotron Soleil, France, 28.6.2011

⋆ Acremann, Y.
Ultrafast magnetism explored by FEL radiation
Helmholtz-Zentrum Berlin User's meeting, Berlin, Germany, 29.-30.11.2011

Baer, S.
Quantum Hall states in quantum point contacts
NCCR QSIT Seminar: Fractional Quantum Hall States, ETH Zürich, 17.3.2011

⋆ Batlogg, B.
Organic semiconductors
University Fribourg, Fribourg, Switzerland, 04.05.2011

⋆ Batlogg, B.
Organic semiconductors: electronics, opto-electronics and thermoelectricity
EMPA Colloquium, Dübendorf, Switzerland, 07.06.2011

⋆ Batlogg, B.
Quantitative studies and modifications of trap states in organic molecular crystals
ICMAT Int. Conf. on Materials for Advanced Technologies 2011, Singapore, 26.06.2011

⋆ Batlogg, B.
Enhanced OFET performance by trap control
ACS IEEE MRS Joint Workshop on Organic Microelectronics & Optoelectronics
San Francisco, USA, 18.07.2011

⋆ Batlogg, B.
Superconductivity: materials and mechanisms
PSI Summer School 2011, Zugerberg, Switzerland, 17.08.2011

⋆ Batlogg, B.
Improved OFET performance through trap state control
Int. Conf. on Organic Photonics and Electronics, Dublin, Irland, 06.09.2011

⋆ Batlogg, B.
Research Integrity
SNF Annual Meeting NRP 62, Fribourg, Switzerland, 15.09.2011

⋆ De Pietro, L.
Microscopia: come rendere visibili gli atomi
ETH en route, Liceo Lugano 2, Lugano, Switzerland, 18.01.2011

⋆ Degen, C.
Pushing the frontiers of nanoscale spin detection
Physics Colloquium, University of Konstanz, Germany, 21.6.2011

⋆ Degen, C.
Materials aspects to scanning diamond magnetometry
62nd Diamond Conference, Warwick, UK, 7.7.2011

⋆ Degen, C.
Towards nanoMRI using scanning probe techniques
FRIAS Black Forest Focus 6 - Magnetic Resonance Microsystems, 28.7.2011

⋆ Degen, C.
Nanoscale magnetic resonance imaging
Inaugural Lecture, ETH Zurich, 20.9.2011

⋆ Degen, C.
Pushing the Frontiers of Nanoscale Spin Detection
Atomic, Mesoscopic and Optical Physics Colloquium, University of Cambridge, UK, 14.11.2011

⋆ Degiorgi, L.
Optical investigation of the charge dynamics in $Ba(Co_xFe_{1-x})_2As_2$
Workshop on Iron-based Superconductors, Kavli Institute for Theoretical Physics, University of California, Santa Barbara, U.S.A., 10.-21.1.2011

⋆ Degiorgi, L.
Optical investigation of the charge dynamics in $Ba(Co_xFe_{1-x})_2As_2$
Winter Conference on Contrasting Superconductivity of Pnictides and Cuprates, Aspen Center for Physics, Aspen, U.S.A., 22.-28.1.2011

⋆ Degiorgi, L.
Optical properties in correlated materials: the charge dynamics of iron-pnictide superconductors
Colloquium at the Physics Department, William and Mary College at Williamsburg, Williamsburg, U.S.A., 18.3.2011

⋆ Degiorgi, L.
Optical investigation of the charge dynamics in $Ba(Co_xFe_{1-x})_2As_2$
March Meeting of the American Physical Society, Dallas, U.S.A., 21.-25.3.2011

⋆ Degiorgi, L.
Optical investigation of the charge dynamics in $Ba(Co_xFe_{1-x})_2As_2$
Condensed Matter Seminar at the Physics Department, University of Florida at Gainesville, Gainesville, U.S.A., 28.3.2011

⋆ Degiorgi, L.
Optical investigation of the charge dynamics in $Ba(Co_xFe_{1-x})_2As_2$
Condensed Matter Seminar at the Leibniz-Institut für Festkörper- und Werkstoffforschung Dresden, Dresden, Germany, 9.5.2011

⋆ Degiorgi, L.
Optical properties in correlated materials: the charge dynamics of iron-pnictide superconductors
Stuttgarter Physikalisches Kolloquium, Universität Stuttgart und Max-Planck Institute für Festkörper- und Materialforchung Stuttgart, Stuttgart, Germany, 31.5.2011

⋆ Degiorgi, L.
Charge dynamics of iron-pnictide superconductors
Workshop on a New Century of Superconductivity: Iron Pnictides and Beyond, Aspen Center for Physics, Aspen, U.S.A., 26.6.-24.7.2011

⋆ Degiorgi, L.
The charge-density-wave state in the two-dimensional layered rare-earth tri-tellurides
International Workshop on Electronic Crystals, ECRYS 2011, Cargese, France, 15.-27.8.2011

⋆ Degiorgi, L.
Anisotropic charge dynamics in detwinned $Ba(Co_xFe_{1-x})_2As_2$
6th International Workshop on Infrared Microscopy and Spectroscopy with Accelerator Based Sources, Trieste, Italy, 4.-8.9.2011

Dusza, A.
Anisotropic charge dynamics in detwinned $Ba(Co_xFe_{1-x})_2As_2$
2011 Swiss Workshop on Materials with Novel Electronic Properties, Les Diablerets, Switzerland, 29.6.-1.7.2011

⋆ Dusza, A.
Anisotropic charge dynamics in detwinned $Ba(Co_xFe_{1-x})_2As_2$
E-MRS 2011 Fall Meeting, Warsaw, Poland, 19.-23.9.2011

Eichler, C.
Tomography and Correlation Function Measurements of Itinerant Microwave Photons
Quantum Information Processing and Communication (QIPC) 2011, International conference at ETH Zurich, Zurich, Switzerland, 5.9.2011

Eichler, C.
Generation and Reconstruction of Two Mode Squeezed States in the Microwave Domain
APS March Meeting, Dallas, USA, 21.3.2011

⋆ Eichler, C.
Tomography and Correlation Function Measurements of Itinerant Microwave Photons
Moriond 2011 - Quantum Mesoscopic Physics, La Thuile, Italy, 13.3.2011

⋆ Ensslin, K.
Quantum Science and Technology in Switzerland
Swiss-Swedish Meeting on Quantum Materials and Devices, Les Diablerets, Switzerland, 7.-9.1.2011

⋆ Ensslin, K.
Single electron control in quantum materials
Colloquium, IFW Dresden, Dresden Germany, 20.1.2011

⋆ Ensslin, K.
Electrons in quantum dots: one-by-one
Physics colloquium, Uni Innsbruck, Austria, 25.1.2011

⋆ Ensslin, K.
Coherent phonons in graphene double dots
International Winterschool on Electronic Properties of Novel Materials, Kirchberg, Austria, 26.2.-5.3.2011

⋆ Ensslin, K.
Spin states in graphene quantum dots
March meeting of the American Physical Society, Dallas, USA, 21.-25.3.2011

⋆ Ensslin, K.
Graphene quantum circuits
Seminar, University of California, Santa Barbara, USA, 29.3.2011

⋆ Ensslin, K.
Graphene quantum circuits
Seminar, University of California, Los Angeles, USA, 31.3.2011

⋆ Ensslin, K.
Spin and charge control in graphene quantum dots
CIFAR winter school on new developments in quantum materials, nanostructures and qinformation, Whistler, Canada,3.-8.4.2011

⋆ Ensslin, K.
Transport through graphene nanostructures
Imaginenano, Graphene 2011, Bilbao, Spain, 11.-14.4.2011

⋆ Ensslin, K.
Quantenmechanik und Informationsverarbeitung: Waren Sie schon einmal gleichzeitig an zwei Orten?
Seniorenuniversität Zürich, Switzerland, 14.4.2011

⋆ Ensslin, K.
Irreversibility in single-electron tunneling
Workshop on ”Nonlinear spin and charge transport through nanoscopic systems”, Mallorca, Spain, 6.-9.7.2011

⋆ Ensslin, K.
Single-electron counting
Joint CEA-ETHZ workshop, Zurich, Switzerland, 8.6.2011

⋆ Ensslin, K.
Irreversibility in single-electron tunneling
Swiss-Swedish Meeting on Quantum Materials and Devices, Gothenburg, Sweden, 25.-27.8.2011

⋆ Ensslin, K.
Graphene Quantum Circuits
Multidisciplinary Workshop on Nanosciences: From molecular systems to functional materials, Venice, Italy, 19.-23.9.2011

⋆ Ensslin, K.
Irreversibility in single-electron tunneling
Workshop on ”Quantum Spintronics” Sardinia, Italy, 2.-6.10.2011

⋆ Ensslin, K.
Electron counting in and out of equilibrium
Physics colloquium, Lund University, Sweden, 28.10.2011

⋆ Ensslin, K.
Electron counting in and out of equilibrium
Physics colloquium, University of Geneva, Switzerland, 31.10.2011

⋆ Ensslin, K.
Dimensionality and Functionality of Quantum Devices
Annual congress of the Swiss Academy of Sciences, Chemistry Platform, on the occasion of the world year of chemistry, Bern, Switzerland, 18.11.2011

⋆ Ensslin, K.
Quantenphysik und Informationsverarbeitung: Waren Sie schon einmal gleichzeitig an zwei Orten?
Treffpunkt Science City, ETH Zurich, Switzerland, 20.11.2011

⋆ Ensslin, K.
Quantenmechanik und Informationsverarbeitung: Waren Sie schon einmal gleichzeitig an zwei Orten?
Seniorenuniversität Winterthur, Switzerland, 23.11.2011

⋆ Ensslin, K.
Graphene nanoribbons revisited
International workshop on ”Spintronics in Graphene”, Singapore, 4.-7.7.2011

Ensslin, K.
Elektrizität
Kindervorlesung, ETH Zurich, Switzerland, 22.6.2011

⋆ Erbudak, M.
Atomic structure of surfaces
Winter workshop on ”Physics and Chemistry of Solids: Theory and Experiment”, Bilkent University, Ankara, 8.11.2011

⋆ Erbudak, M.
Inner-shell spectroscopies
Winter workshop on ”Physics and Chemistry of Solids: Theory and Experiment” in Bilkent University, Ankara, 12.11.2011

⋆ Erbudak, M.
Excited v.s. ground state in photoelectric emission
Seminar in the Chemistry Department of Bilkent University, Ankara, Turkey, 8.3.2011

⋆ Erbudak, M.
Formation of nanometer-size islands on quasicrystals
Seminar in the Physics Department, Bogazici University, Istanbul, Turkey, 16.3.2011

⋆ Erbudak, M.
Ordered oxide layers on quasicrystal surfaces
Seminar in Department of Materials Science, Anadolu University, Eskisehir, Turkey, 8.8.2011

Erbudak, M.
SWAXS analysis on some quasicrystal formations
XXII Congress Int. Union Crystallography, Madrid, Spain. 22.-30.8.2011

⋆ Fedorov, A.
Circuit QED for Quantum Control and Computing
Group seminar, invited by K. Ishibashi, RIKEN, Wako, Japan, 9.8.2011

⋆ Fedorov, A.
Benchmarking a Teleportation Circuit realized in Circuit QED
The 1st International Conference on Quantum Technologies, Moscow, 11.7.2011

Feil, T.
Growth and Characterization of Advanced Semiconductor Quantum Materials
University of Basel, Switzerland, 13.05.2011

⋆ Filipp S.
Circuit Quantum Electrodynamics: Photons, Superconducting Qubits and Atoms on a chip
’Cold Atoms’ - Group seminar, invited by Lucia Hackermueller, University of Nottingham, U.K., 7.12.2011

⋆ Filipp, S.
Circuit Quantum Electrodynamics - Interfacing Photons, Superconducting Qubits and Rydberg Atoms on a Chip
Seminar ’Nichtlineare Quantenoptik’, invited by Prof. Richter, University of Hamburg, Germany, 20.10.2011

⋆ Filipp, S.
Distributing Quantum Information with Microwave Resonators in Circuit QED
4th Workshop on the Physics and Applications of Superconducting Microresonators, Grenoble, France, 28.7.2011

Filipp, S.
Dark States of Cavity Coupled Qubits
APS March Meeting, Dallas, USA, 21.3.2011

⋆ Filipp, S.
Dispersive multi-mode mediated qubit coupling in circuit QED
Quantum Simulations Workshop, Benasque, Spain, 28.2.2011

⋆ Filipp, S.
Hybrid Quantum Systems - Circuit QED meets Rydberg atoms
Swiss Swedish Meeting on "Quantum Materials and Devices", Les Diableret, Switzerland, 7.1.2011

⋆ Fink, J.M.
Quantum nonlinearities in strong coupling circuit QED
Seminar at Max Planck Institute for the Science of Light, Erlangen, Germany, 21.7.2011

Fognini, A.
Ultrafast magnetism seen by time and spin resolved photoemission at FLASH
MMM conference, Scottsdale, USA, 2.11.2011

Gvasaliya, S.
Phase transitions in relaxors as seen by neutron scattering
APS March Meeting, Dallas, USA, 21.03.2011

⋆ Gvasaliya, S.
The phase transitions in $PbMg_{1/3}Nb_{2/3}O_3$ and $PbMg_{1/3}Ta_{2/3}O_3$ relaxor ferroelectrics
Condensed-Matter Physics & Materials Science Seminar, Brookhaven National Laboratory, Upton NY, USA, 10.03.2011

⋆ Gvasaliya, S.
Static and dynamic short-range order in relaxors
Department of Ferroelectricity Seminar, Ioffe Physical Technical Institute, St. Petersburg, Russia, 28.12.2011

⋆ Häusermann Roger
Fast and Slow Charge Traps in Organic Semiconductors: Characterization, Identification and Elimination
Seminar at Chiba University, Chiba, Japan, 21.11.2011

Häusermann, R.
Role of Semiconductor and Gate-dielectric in Charge Trapping during Gate-bias Stress
ICMAT 2011 "International Conference on Materials for Advanced Technologies" Singapore, 29.06.2011

Hüvonen, D.
Luttinger parameter in a magnetized spin chain
3rd Bilateral Estonian-German Workshop, Cottbus, Germany, 13.06.2011

Hüvonen, D.
Luttinger parameter in a magnetized spin chain
Swiss Workshop on Materials with Novel Electronic Properties, Les Diablerets, Switzerland, 29.06.2011

Hüvonen, D.
Luttinger parameter in a magnetized spin chain
26th International Conference on Low Temperature Physics (LT26), Beijing, China, 10.08.2011

Ihn, T.
Coherent electron-phonon coupling in double quantum dots
EP2DS, Tallahassee, USA, 28.7.2011

Ihn, T.
Electronic Transport in Graphene Nanostructures
Graphene Week, Obergurgl, Austria, 28.4.2011

⋆ Ihn, T.
Electronic Transport in Graphene Nanostructures
Int. Conf. on Solid State Devices and Materials (SSDM), Nagoya, Japan, 29.9.2011

⋆ Ihn, T.
Graphene Nanostructures
Int. Conf. on Solid State Devices and Materials (SSDM), Rump Session, Nagoya, Japan, 29.9.2011

⋆ Ihn, T.
Electronic Transport in Graphene Nanostructures
Moriond Conference on Quantum Mesoscopic Physics, LaThuile, Italy, 14.3.2011

⋆ Ihn, T.
Graphene Nanostructures
Inauguration of the Peter Grünberg Institute, Jülich, Germany, 6.4.2011

⋆ Ihn, T.
Interactions and disorder in graphene constrictions
CeNS Winterschool, St. Christoph a. Arlberg, Austria, 29.3.2011

⋆ Ihn, T.
Transport in graphene constrictions and quantum dots
Int. Conf. on the Science and Applications of Nanotubes (NT11), Graphene Satellite Symposium, Cambridge, UK, 16.6.2011

Ihn, T.
Quantum Spintronics
NCCR QSIT Meeting, Arosa, Switzerland, 12.1.2011

Kanter, J.
The superconducting phase and electronic excitations of (Rb,Cs)Fe_2As_2
APS March Meeting 2011, Dallas, TX, USA, 21.03.2011

Karpinski, J.
Single crystals of iron pnictides grown under high pressure
Study of Matter at Extreme Conditions (SMEC), Miami, USA, 27.03.2011

⋆ Karpinski, J.
Single crystals of iron pnictides: investigations of basic properties relevant for applications
MRS Spring Meeting, San Francisco, USA, 25.04.2011

Karpinski, J.
Doping and substitutions in LnFeAsO
Physical Society and Austrian Physical Society, Lausanne, Switzerland, 15.06.2011

⋆ Karpinski, J.
Doping and substitutions in LnFeAsO single crystals grown at high pressure: influence on superconducting properties and structure
7th Intern. Conf. "Vortex matter in Nano- structured superconductors", Rhodes, Greece, 10.09.2011

⋆ Karpinski, J.
Doping and substitutions in LnFeAsO single crystals grown at high pressure
European Materials Conference E-MRS Fall Meeting, Warsaw, Poland, 19.09.2011

⋆ Karpinski, J.
LnFeAsO single crystals: influence of doping and substitutions on superconducting properties and structure
Polish Conference on Superconductivity, Kazimierz, Poland, 09.10.2012

⋆ von Känel, H.
Hetero-epitaxial integration on pre-patterned Si substrates
XIV International Conference on Gettering and Defect Engineering in Semiconductor Technology, Hotel Loipersdorf Spa & Conference, Austria, 25.09.2011

⋆ von Känel, H.
SiGe/Si heteroepitaxy: From layers to three-dimensional crystals
SFB IR-ON Symposium, Vienna, Austria, 10.03.2011

⋆ von Känel, H.
Self-aligned arrays of semiconductor crystals
3rd International Conference from Nanoparticles and Nanomaterials to Nanodevices and Nanosystems (IC4N), Crete Island, Greece, 26.06.2011

von Känel, H.
Self-aligned epitaxy in mask-less deposition with kinetic and geometric constraints
7th International Conference on Si Epitaxy and Heterostructures, Leuven, Belgium, 28.08.2011

⋆ Kirk, T.L.
Near Field Emission Scanning Electron Microscopy and Applications in the Semiconductor Industry
Seminar, Intel Corporation, Hillsboro, Oregon (U.S.A.), 05.05.2011

⋆ Kirk, T.L.
Introduction to Near Field Emission Scanning Electron Microscopy
Seminar, Rowan University, Glassboro, New Jersey (U.S.A.), 05.06.2011

⋆ Kirk, T.L.
Near Field Emission Scanning Electron Microscopy
Seminar, Attocube Systems, München,Germany, 10.06.2011

Komijani, Y.
Counting statistics of hole transfer in a quantum dot with dense spectra
Uni. of Konstanz, Germany, 28.9.2011

⋆ Küng, B.
Irreversibility in single-electron tunneling
Nanotechnology and Research (NanoTR) 7, Istanbul, Turkey, 28.6.2011

Küng, B.
Irreversibility on the level of single-electron tunneling
Quantum information processing and communication (QIPC), Zürich, Switzerland, 7.9.2011

Lang, C.
Observation of photon blockade in circuit QED usingsecond-order correlation function measurements
APS March Meeting, Dallas, USA, 21.3.2011

Leek, P.
Coupling a double quantum dot to a microwave resonator
Quantum Information Processing and Communication (QIPC) 2011, International conference at ETH Zurich, Zurich, Switzerland, 5.9.2011

Leek, P.
Coupling a double quantum dot to a microwave resonator
Quantum Information Processing and Communication (QIPC) 2011, International conference at ETH Zurich, Zurich, Switzerland, 5.-9.9.2011

⋆ Lucarelli, A.
Charge dynamics in iron-pnictide superconductors
Meeting of the MaNEP Forum, Neuchatel, Switzerland, 18.1.2011

Lucarelli, A.
Anisotropic Charge Dynamics in Detwinned $Ba(Co_xFe_{1-x})_2As_2$
SCES 2011, Selwyn College, Cambridge, UK, 29.8.-4.9.2011

Mathis, T.
Formation process of a conducting interface between two organic crystals
Int. Conference on Material for Advanced Technologies ICMAT, Singapore, 27.06.2011

⋆ Mesot, J.
Spectroscopy on superconductors and related materials
Swiss-Swedish Meeting on ”Quantum Materials and Devices”, Les Diablerets, Switzerland, 07.01-09.01.2011

⋆ Mesot, J.
From materials to medical research at Paul Scherrer Institute
Université de Genève, Switzerland, 31.01.2011

⋆ Mesot, J.
Quelle est l’importance de la recherche fondamentale pour notre société?
Club des Quatre Saisons, Zurich, Switzerland, 06.04.2011

⋆ Mesot, J.
Die Bedeutung der Grundlagenforschung für unsere Gesellschaft
Business Club Mittelland Veranstaltung, Aarau, Switzerland, 29.06.2011

⋆ Mesot, J.
Das PSI im Überblick
Conférence des Recteurs des Universités Suisses, Berne, Switzerland, 08.09.2011

⋆ Mesot, J.
The Status and Perspectives of Collaboration between the Paul Scherrer Institut and the Chinese Academy of Sciences
7th Chinese Association of Science and Technology in Switzerland General Assembly, Muri, Switzerland, 17.09.2011

⋆ Mesot, J.
From fundamental research to applications: examples from the Paul Scherrer Institute
Symposium Österreichische Akademie der Wissenschaften, Vienna, Austria, 24.10.2011

Moll, P.
Nearly isotropic critical currents in SmFeAs(O,F) in high magnetic fields
APS March Meeting Dallas, TX, USA, 22.03.2011

Moll, P.
Fermi surface of the pnictide superconductor $LaRu_2P_2$ studied by quantum oscillations
APS March Meeting Dallas, TX, USA, 23.03.2011

⋆ Moll, P.
High magnetic-field scales and critical currents in SmFeAs(O,F) crystals
Studies of Matter under Extreme Conditions Conference (SMEC) Miami, FL, USA, 29.03.2011

⋆ Moll, P.
Ion Beam Sample Preparation for Pulsed Magnetic Fields: Application to Pnictides
DACH Workshop EMEZ, ETH Zurich, Switzerland, 27.06.2011

⋆ Mühlbauer, S.
Structure and Phase Transitions of the Dzyaloshinskii-Moriya Helimagnet $Ba_2CuGe_2O_7$
DMI workshop, St. Petersburg, Russia, 26.05.2011

⋆ Mühlbauer, S.
Small Angle Neutron Scattering of Skyrmion Structures in Chiral MnSi
ESS Workshop, Bad Reichenhall, Germany, 11.10.2011

⋆ Mühlbauer, S.
Structure and Phase Transitions of the Dzyaloshinskii-Moriya Helimagnet $Ba_2CuGe_2O_7$
Swiss Workshop on Materials with Novel Electronic Properties, Les Diablerets, Switzerland, 29.06.2011

Mühlbauer, S.
Structure and Phase Transitions of the kinky Dzyaloshinskii-Moriya Helimagnet $Ba_2CuGe_2O_7$
Neutron Scattering and Magnetism, Group Workshop, Celerina, Switzerland, 13.07.2011

Mühlbauer, S.
New phase of the Dzyaloshinskii-Moriya Helimagnet $Ba_2CuGe_2O_7$
APS March Meeting, Dallas, USA, 21.03.2011

⋆ Ott, H.-R.
100 Years of Superconductivity
MaNEP Winter School, Saas Fee, Switzerland, 11.01.2011

⋆ Ott, H.-R.
100 Jahre Supraleitung
Physikalische Gesellschaft Zürich, Zürich, 09.06.2011

⋆ Ott, H.-R.
First Glimpses at Unconventional Superconductivity
SCES Conference 2011, Cambridge, United Kingdom, 03.09.2011

Pechal, M.
Adiabatic and Non-Adiabatic Geometric Phases of a Harmonic Oscillator in Superconducting Circuits
Quantum Information Processing and Communication (QIPC) 2011, International conference at ETH Zurich, Zurich, Switzerland, 5.9.2011

⋆ Pescia, D.
Fundamental aspects of magnetism
Lecture series, Winterschool on "Physics and Chemistry of Solids: Theory and Experiment" in Bilkent University, Ankara, 10.11.2011

Pescia, D.
Modeling magnetism in solids with Dirac-Delta function potentials
Workshop "Magnetism in the past and now", Preda, Switzerland, 13.-19.02 2011

Prša, K.
A Direct Observation of Quasi-one-dimensional Magnetism
European Conference on Neutron Scattering, Prague, Czech Republic, 17.-22.07.2011

Prša, K.
Tunable Restriction of Phase-space of Magnetic Configurations in the Triangular Ising Antiferromagnet $Ca_3Co_2O_6$
Topological Materials Workshop, Institut Laue-Langevin, Grenoble, France, 26-28.10.2011

Reichl, C.
Investigations of Si-dopant Layers on Ultrahigh-mobility 2DEGs in GaAs/AlGaAs-Structures
Euro-MBE, Alpes d'Huez, France, 23.03.2011

⋆ Rössler, C.
Hybrid Quantum Dots
VCIAN, Las Vegas, 21.04.2011

Rössler, C.
Many-body Effects in Ultra-Clean Quantum Point Contacts
EP2DS, Tallahassee, 25.07.2011

Schiltz, G.
Bridging lectures with summary podcasts
19th International Conference on Computers in Education, Chiang Mai, Thailand, 1.12.2011

Schiltz, G.
Student Activities In Introductory Physics lectures
IDEA League Workshop on Excellence in Engineering Education, TU Delft, 3.11.2011

Schiltz, G.
Lehrentwicklung aus einem Guss?
Wissensgemeinschaften: Fachtagung GMW/Delfi 2011, TU Dresden, 7.9.2011

Schiltz, G.
Bridging lectures with summary podcasts
Proceedings of the 19th International Conference on Computers in Education ICCE 2011, Chiang Mai, Thailand, 28.11.-2.12.2012

Schmidiger, D.
Long-lived magnons throughout the Brillouin zone of the strong-leg spin ladder $(C_7D_{10}N)_2CuBr_4$
Swiss Workshop on Materials with Novel Electronic Properties, Les Diablerets, Switzerland, 29.06.2011

Shiroka, T.
Probing randomness in Heisenberg spin chains via magnetic resonance
MaNEP SWM Meeting 2011, Les Diablerets, Switzerland, 29.06-01.07.2011

⋆ Shiroka, T.
Low-temperature features of random Heisenberg spin chains
Low-Temperature Physics Conference LT26, Beijing, China, 11.08.2011

Shiroka, T.
Investigating random Heisenberg spin chains via nuclear magnetic resonance
Broadband Solid-State NMR, Trogir, Croatia, 05.09.2011

⋆ Thede, M.
Effect of bond disorder in spin-1/2 antiferromagnetic Heisenberg chains
μSR Users' Meeting, PSI, Villigen, Switzerland, 26.01.2011

⋆ Thede, M.
Bond disorder in a quasi 1-d antiferromagnet
12th International Conference on μSR, Cancun, Mexico, 16.05.2011

Thede, M.
Bond disorder in a quasi 1-d antiferromagnet
Swiss Workshop on Materials with Novel Electronic Properties, Les Diablerets, Switzerland, 29.06.2011

Thede, M.
Bond disorder in a quasi 1-d antiferromagnet
26th International Conference on Low Temperature Physics (LT26), Beijing, China, 10.08.2011

Vaterlaus, A.
Begabtenförderung aus Sicht der ETH
Tagung zur Begabtenförderung Bildungsraum Nordwestschweiz, Kantonsschule Wettingen, 16.09.201

⋆ Vaterlaus, A.
Time and spin resolved photoemission
Seminarbeitrag in der Reihe: Science with photons, BESSY, Berlin, 08.11.2011

Vindigni, A.
What do magnetic domain walls share with the ubiquitous physics of solitons?
Workshop "Magnetism in the past and now", Preda, Switzerland, 13.-19.02.2011

⋆ Vindigni, A.
The physics of emerging length scales in low-dimensional magnetic systems
Seminar Paul Scherrer Institute - PSI, Villigen, Switzerland, 12.4.2011

Wagner, C.
Promoting Formative Assessment in High School Teaching of Physics
ICPE 2011, Mexico-City, Mexico, 15.-19.8.2011

Wagner, C.
Matura KiK Projektunterricht an der Kantonsschule Romanshorn
Weiterbildungsveranstaltung Mathematik-Physik, ETH Zurich, 4.11.2011

⋆ Wallraff, A.
Photons, Qubits and Computers - A Quantum Mechanics Lab on a Chip
Condensed Matter and Materials Physics Conference (CMMP11), Manchester, UK, 13.12.2011

⋆ Wallraff, A.
Quantum Optics with Superconducting Circuits: Exploring Propagating Microwave Photons
Quantum Information, Measurement and Control, CEA-EDF-INRIA School, INRIA Paris-Rocquencourt, Paris, 29.11.2011

⋆ Wallraff, A.
Photons, Qubits and Computers - Constructing Quantum Machines on a Chip
Physikalisches Kolloquium, invited by Prof. Gernot Guentherodt, RWTH Aachen, Aachen, Germany, 28.11.2011

⋆ Wallraff, A.
Circuit Quantum Electrodynamics
NanoResonance 2011, Heinrich Fabri Haus, Blaubeuren, Germany, 2.11.2011

⋆ Wallraff, A.
Exploring the Quantum Physics of Light with Micro- and Nanoelectronic Circuits
Nanosciences: From molecular systems to functional materials, Venice International University (VIU), Venice, Italy, 19.9.2011

⋆ Wallraff, A.
Quantum optics with superconducting circuits
CFN Summer School 2011 on NANO-ELECTRONICS, DFG-Center for Functional Nanostructures (CFN) of the Karlsruhe Institute of Technology and the EU network on Nanoelectronics Concepts, Theory and Modelling (NanoCTM), Bad Herrenalb, Germany, 11.9.2011

⋆ Wallraff, A.
Quantum science and Technology with Electronic Circuits at Ultra Low Temperatures
Special Event at LT 26 hosted by Oxford Instruments, Beijing, China, 11.8.2011

⋆ Wallraff, A.
Generating and Detecting Propagating Photons in Superconducting Circuits
26th International Conference on Low Temperature Physics (LT26), Beijing, China, 10.8.2011

⋆ Wallraff, A.
Quantum Optics with Superconducting Circuits: Exploring Propagating Microwave Photons
Institut Neel-CNRS and UJF, Grenoble, France, 5.7.2011

⋆ Wallraff, A.
Experiments with Single Microwave Photons
Quantum machines: measurement and control of engineered quantum systems, Summer School, Les Houches, France, 4.7.2011

⋆ Wallraff, A.
Quanten, Bits und Computer - Neue Perspektiven in der Informationstechnologie
ETH Foundation Thanksgiving 2011, Roessler prize talk, ETH Zurich, Switzerland, 23.6.2011

⋆ Wallraff, A.
Quantum Optics and Quantum Computing with Superconducting Circuits
Quantum Repeater Status Seminar 2011, Bad Honnef, Germany, 20.6.2011

⋆ Wallraff, A.
Exploring Propagating Microwave Photons in Quantum Optics Experiments with Superconducting Circuits
Quantum Science and Technologies, EU workshop, Rovereto, Italy, 9.5.2011

⋆ Wallraff, A.
Quantum Science and Technology with Superconducting Electronic Circuits
International Conference ”Quantum Technology”, Akademie der Naturforscher Leopoldina, German Museum, Munich, Germany, 8.5.2011

⋆ Wallraff, A.
Quantum Optics with Superconducting Circuits: Exploring Propagating Microwave Photons
CIFAR Quantum Physics Discussion and Winter School, Canadian Institute for Advanced Research (CIFAR) 2011 Winter School, Fairmont Whistler, BC, Canada, 3.4.2011

⋆ Wallraff, A.
Quantum Optics with Superconducting Circuits
Quantum Nanoscience, Winter school organized by the International Max Planck Research School for Advanced Materials and Ecole Polytechique Federal de Lausanne in collaboration with Troisieme Cycle de la Suisse Romande, Crans Montana, Switzerland, 27.3.2011

⋆ Wallraff, A.
Tomography and Correlation Function Measurements of Itinerant Microwave Photons
APS March Meeting, Dallas, USA, 21.3.2011

⋆ Wallraff, A.
Tomography and Correlation Function Measurements of Propagating Microwave Photons
Spring Meeting of the German Physical Society, special symposium on ”Cavity meets Circuit Quantum Electrodynamics”, Dresden, Germany, 13.3.2011

⋆ Wallraff, A.
Quantum Optics with Superconducting Circuits: Controlling Photons, Qubits and their Interactions
Physikalisches Kolloquium, invited by Prof. Johannes Hecker Denschlag, Universitaet Ulm, Germany, 14.2.2011

⋆ Wallraff, A.
Cavity QED with superconducting circuits: Measuring microwave photon correlations
5th International Conference on Spontaneous Coherence in Excitonic Systems (ICSCE-5), Swiss Federal Institute of Technology, Lausanne, Switzerland, 7.2.2011

⋆ Wallraff, A.
Cavity QED with Superconducting Circuits: Measuring Microwave Photon Correlations
Colloquium of the Center for Optical Quantum Technologies, invited by Prof. Peter Schmelcher, Zentrum fuer Optische Quantentechnologien, Universitaet Hamburg, Germany, 26.1.2011

⋆ Wallraff, A.
Hybrid Quantum Systems using Microwave Frequency On-Chip Resonators as a Coupling Bus
NCCR project presentation at NCCR-QSIT Meeting 2011, Arosa, Switzerland, 12.1.2011

⋆ Wallraff, A.
Tomography and Correlation Function Measurements of Itinerant Microwave Photons
Quantum Physics of Low-Dimensional Systems and Materials, Stellenbosch Institute for Advanced Study (STIAS), Stellenbosch, South Africa, 3.1.2011

⋆ Wegscheider, W.
Fractional Quantum Hall States for Topological Information Processing, QSIT Workshop
Arosa, Switzerland, 14.01.2011

⋆ Wegscheider, W.
Cryogenic pumping for the fabrication of highest-purity semiconductors
German Physical Society (DPG), Dresden, Deutschland, 14.03.2011

⋆ Wegscheider, W.
Magnetic Coupling of a High-Mobility 2D Hole Gas with Remotely-Doped Mn Ions
EP2DS19/MSS15, Tallahassee, Florida, USA, 26.07.2011

⋆ Wegscheider, W.
Hole Transport in GaAs Quantum Wires Fabricated by Cleaved Edge Overgrowth Molecular Beam Epitaxy
Satellite Materials World Network Meeting on Nuclear Spins in Semiconductor Heterostructures, Sardinia, Italy, 4.10.2011

Willa, K.
Synthesis and Function of Thermoelectric Materials
Villars sur Ollons, Switzerland, 14.08.2011

Wulf, E.
Bond randomness in a frustrated spin ladder
APS March Meeting 2011, Dallas, USA, 21.03.2011

Wulf, E.
Bond randomness in a frustrated spin ladder
Swiss Workshop on Materials with Novel Electronic Properties, Les Diablerets, Switzerland, 29.06.2011

Wulf, E.
Bond randomness in the frustrated spin ladder Sul-$Cu_2(Cl_{1-x}Br_x)_4$
26th International Conference on Low Temperature Physics (LT26), Beijing, China, 10.08.2011

Wüster, W.
Probing Fractional Quantum Hall States in Ultra-High Mobility 2DEGs
28th Jerusalem Winter School in Theoretical Physics, Jerusalem, 04.1.2011

Zanin, D.,
V-d-I curves, Measurement and Models
Seminar, ETH Zurich, 24.11.2011

Zanin, D.
Holographic images of sharp field emitters for NFESEM
Workshop "Magnetism in the past and now", Preda, Switzerland, 13.-19.02 2011

Zhao, S.
Disorder in a two-dimensional spin liquid
Swiss Workshop on Materials with Novel Electronic Properties, Les Diablerets, Switzerland, 29.06.2011

Zhao, S.
Disorder in a two-dimensional spin liquid
26th International Conference on Low Temperature Physics (LT26), Beijing, China, 10.08.2011

⋆ Zheludev, A.
Disorder in quantum magnets
Quantum Quenches and Strongly Correlated Physics, Montauk, New York, USA, 06.09.2011

⋆ Zheludev, A.
Disorder and magnon localization in quantum magnets
Seminar, Neutron Scattering Science Division, Oak Ridge National Laboratory, Oak Ridge, USA, 31.08.2011

⋆ Zheludev, A.
In search of the Bose Glass
26th International Conference on Low Temperature Physics (LT26), Beijing, China, 10.08.2011

⋆ Zheludev, A.
In search of the Bose Glass
Swiss Workshop on Materials with Novel Electronic Properties, Les Diablerets, Switzerland, 29.06.2011

⋆ Zheludev, A.
Disorder in quantum magnets
Lecturer, Summer School "Disordered Systems: From Condensed-Matter Physics to Ultracol Atomic Gases", Cargese, France, 30.05.2011

Zhigadlo, N.
Interplay of composition, structure, magnetism and superconductivity in $SmFeAs_{1-x}P_xO_y$
Joint Annual Meeting of the Swiss Physical Society and Austrian Physical Society, Lausanne, Switzerland,15.06.2011

Zhigadlo, N.
Recent progress in crystal growth of oxypnictide superconductors
8th International Conference of the series on Stripes and High T_c Superconductivity "Quantum Phenoma in Complex Matter", STRIPES 11, Sapienza University of Rome, Rome, Italy, 10.07.2011

⋆ Zhigadlo, N.
Superconducting materials from high pressure synthesis
SLS symposium "Crystal growth and characterization", PSI Villigen, Switzerland, 06.09.2011

⋆ Zhigadlo, N.
Crystal growth, structure and physical properties of LnFeAsO (Ln = rare earth) oxypnictide superconductors
4th International Conference "Fundamental problems of high temperature superconductivity" FPS'11, Zvenigorod, Russia, 03.10.11

⋆ Zhigadlo, N.
Recent developments in crystal growth of LnFeAsO (Ln = rare earth) oxypnictide superconductors
7th International Conference "Vortex Matter in Nanostructured Superconductors", Rhodes, Greece, 10.09.2011

Zhigadlo, N.
High-pressure crystal growth, structure and superconducting properties of LnFeAsO (Ln = rare earth)
European Materials Conference E-MRS 2011 Fall Meeting, Warsaw, Poland, 19.09.2011

Zimmerling, T.
Ion Irradiation Induced Hole Trap States in Rubrene Single Crystals
Int. Conference on Material for Advanced Technologies ICMAT, Singapore, 27.06.2011

12.2 Posters

Baer, S.
Quantum dots in the Quantum Hall regime
QSpice2 Workshop, Sardinia, Italy, Oct. 2011

Baer, S.
Quantum dots in the Quantum Hall regime
NCCR QSIT evaluation, ETH Zürich, 08.12.2011

Berger, S.
Multi-level geometric phases in circuit QED
Quantum Information Processing and Communication (QIPC) 2011, International conference at ETH Zurich, Zurich, Switzerland, 5.9.2011

Bischoff, D.
Graphene Quantum Dots and Related Topics
QSIT Junior meeting, Passugg, Switzerland, 21.-24.6.2011

Bischoff, D.
Resist Residues
Raith User Meeting, ETH Zürich, Switzerland, 15.11.2011

Casola, F.
Frustration and Quantum Criticality in a Spin Ladder
MaNEP SWM Meeting 2011, Les Diablerets, Switzerland, 29.06-01.07.2011

Casola, F.
Field-Induced Incommensurate Magnetic Order in a Frustrated Heisenberg Ladder
SCES Conference 2011, Cambridge, United Kingdom, 29.08-03.09.2011

Choi, T.
Novel semiconductor materials: fabrication and transport experiments
QSIT meeting Arosa 2011, Arosa, Schweiz, 12.-14.1.2011

Dröscher, S.
Cotunneling and one-dimensional localization in graphene nanoribbons
Graphene Week 2011, Obergurgl, Austria, 25.04.2011

Eichler, C.
Experimental State Tomography of Itinerant Single Microwave Photons
NCCR-QSIT Meeting 2011, Arosa, Switzerland, 12.1.2011

Falub, C.
Epitaxial growth of high quality Ge layers on Si substrates using a novel approach
7th Internation Conference on Si Epitaxy and Heterostructures, Leuven, Belgium, 28.08.2011

Falub, C.
Self-aligned arrays of epitaxial Ge crystals on Si substrates
XIV International Conference on Gettering and Defect Engineering in Semiconductor Technology, Loipersdorf, Austria, 25.09.2011

Fedorov, A.
Generation of multi-qubit entanglement in circuit QED architecture
Quantum Information Processing and Communication (QIPC) 2011, International conference at ETH Zurich, Zurich, Switzerland, 5.9.2011

Filipp, S.
Symmetry-selective Rabi oscillations and observation of subradiance in circuit QED
Quantum Information Processing and Communication (QIPC) 2011, International conference at ETH Zurich, Zurich, Switzerland, 5.9.2011

Fink, J.M.
Quantum optics experiments with 2D and 3D microwave cavities
Micro and macro-cavities in classical and non-classical light, Physikzentrum Bad Honnef, Germany, 30.9.2011

Frey, T.
Integration of quantum dots with superconducting microwave circuits
Quantum Information Processing and Communication (QIPC) 2011, International conference at ETH Zurich, Zurich, Switzerland, 5.-9.9.2011

Hellmüller, S.
Using High Frequencies to Probe Semiconducting Nanostructures
NCCR QSIT General Meeting Arosa, GR, 12.1.2011

Häusermann, R., Willa, K.
Methods to Fabricate, Measure and Analyze Organic Semiconductor Devices
MRC Graduate Symposium, Zürich, Switzerland, 08.06.2011

Häusermann, R.
Charge Trapping due to Gate-Bias-Stress in Organic Semiconductors: Role of Dielectric and Semiconductor
CECAM workshop ”First Principles Theory and Modeling in Organic Electronics” Lausanne, Switzerland, 01.02.2011

Häusermann, R.
Highly Stable Organic Devices with Cytop as Fluoropolymer Gate Dielectric
MRC Graduate Symposium, Zürich, Switzerland, 08.06.2011

Jacobsen, A.
Electronic transport in a three-terminal quantum dot
ESONN summer school, Grenoble, France, 24.8.2011

Jacobsen, A.
Transport in a three-terminal graphene quatum dot
Workshop on quantum spintronics 2, Porto Ottiolu, Sardinia, Italy, 03.10.2011

Küng, B.
Irreversibility on the level of single-electron tunneling
EP2DS, Tallahassee FL, USA, 27.7.2011

Küng, B.
Occupancy of a quantum dot in cotunneling processes
EP2DS, Tallahassee FL, USA, 27.7.2011

Lang, C.
Observation of Photon Blockade in Circuit QED using Correlation
Quantum Information Processing and Communication (QIPC) 2011, International conference at ETH Zurich, Zurich, Switzerland, 5.9.2011

⋆ Moll, P.
Vortex lock-in dissipation in c-axis transport of iron pnictide superconductors
13th International Workshop on Vortex Matter in Superconductors, Chicago, IL, USA, 31.07.2011

Morf, T.
Molecular Electronics: From Organic Electronics to Single Molecules
Workshop an EMPA, Dübendorf, Schweiz, 24.06.2011

Nichele, F.
Novel semiconductor materials: fabrication and transport experiments
Arosa, Switzerland, 12.1.2011

Nichele, F.
p-type GaAs rings with strong spin-orbit interaction
QSIT Junior meeting, Passugg, 21.-24.6.2011

Nichele, F.
p-type GaAs rings with strong spin-orbit interaction
Workshop on Quantum Spintronics II, Hotel ”I Corbezzoli”, Porto Ottiolu, Sardinia, Italy, 2.-6.10.2011

Pascher, N.
Scanning Gate Microscooy on Gapphene Nanostructures
QSIT Junior Meeting, Passug, Graubünden, Schweiz, 21.-24.6.2011

Pascher, N.
Scanning Gate Microscopy on Graphene Nanoconstrictions
ESONN Sommer Schule, Grenoble Frankreich, 21.8.-10.9.2011

Pechal, M.
Measurement of the Geometric Phase of a Harmonic Oscillator in Circuit QED
Quantum Information Processing and Communication (QIPC) 2011, International conference at ETH Zurich, Zurich, Switzerland, 5.9.2011

Prša, K.
Intrinsic Metamagnetism in a Frustrated Antiferromagnet
Swiss Physical Society meeting, EPFL Lausanne, Switzerland, 15.-17.06.2011

Prša, K.
Direct Observation of an Emergent Quasi-one-dimensional Magnetic Nanostructure
MaNEP SWM Meeting 2011, Les Diablerets, Switzerland, 29.06-01.07.2011

Rössler, C.
Hybrid Quantum Dots
MSS, Tallahassee, USA, 25.07.2011

Shiroka, T.
Long- vs. short-range antiferromagnetic order in Ce-based iron pnictides
Swiss Physical Society meeting, EPFL Lausanne, Switzerland, 15.-17.06.2011

Simonet, P.
Electronic transport in a three-terminal quantum dot
ESONN summer school, Grenoble, France, 24.8.2011

Steffen, L.
Quantum process tomography of entangling gates in circuit QED
Quantum Information Processing and Communication (QIPC) 2011, International conference at ETH Zurich, Zurich, Switzerland, 5.9.2011

Steffen, L.
Entangling protocols for two qubits in circuit QED
NCCR-QSIT Meeting 2011, Arosa, Switzerland, 12.1.2011

Thiele, T.
Towards hybrid cavity quantum electrodynamics with atoms and circuits
Quantum Information Processing and Communication (QIPC) 2011, International conference at ETH Zurich, Zurich, Switzerland, 5.9.2011

Thiele, T.
Hybrid Cavity QED with Atoms and Circuits
NCCR-QSIT Meeting 2011, Arosa, Switzerland, 12.1.2011

Varlet, A.
Improving graphene quality using Boron-Nitride substrate
Fundamentals of Nanoelectronics, Tenerife, Spain, 12.-17.02.2012

Wagner, C.
A Model of Concept Learning
Poster-Presentation FFP12 2011, Udine, Italy, 21.-23.11.2011

Willa, K.
Molecular Electronics: From Organic Electronics to Single Molecules
6th MRC Graduate Symposium, ETH Zürich, 08.06.2011

Willa, K.
Molecular Electronics: From Organic Electronics to Single Molecules
Workshop an EMPA, Dübendorf, Schweiz, 24.06.2011

Zhigadlo, N.
High-pressure crystal growth of LnFeAsO (Ln = rare earth)
26th International Conference on Low Temperature Physics, Beijing, China, 10.08.2011